Analysis and Simplification of Chemical Kinetics Mechanisms with CSP-based techniques

Riccardo Malpica Galassi

Mechanical and Aerospace Engineering Department

Sapienza University of Rome, IT

Advisor: Mauro Valorani, Professor

Co-Advisor: Pietro Paolo Ciottoli, PhD

XXX Ciclo 2014-2017

SAPIENZA
UNIVERSITÀ DI ROMA

Rome, January 2018

This thesis was written with LaTeX

Author e-mail: riccardo.malpicagalassi@uniroma1.it

Acknowledgements

My deep gratitude goes first to my mentor and advisor, Professor Mauro Valorani, the wise guide along my path, who taught me to think.

I am grateful to Dr.Habib Najm, who strongly contributed to my education showing me his magnificent way of doing science.

Pietro, you should be the first of this list, but amongst all the life, science and politics lessons you gave me, you taught me that ranks are meaningful only in linear algebra.

I thank my fellow workmates, who made every day spent in our room a better day.

Last but not the least, I would like to thank my family, who always pushed me to do what I liked and wanted to do.

Contents

List of Figures

List of Tables

Abstract

The computational singular perturbation (CSP) method is exploited to build a comprehensive framework for analysis and simplification of chemical kinetic models. The necessity for both smart post-process tools, able to perform rational diagnostics on large numerical simulations of reactive flows, and affordable reduced kinetic mechanisms, to make the simulations feasible, is the driving force behind this work. The ultimate goal is to improve the understanding of the fundamentals of chemically reacting flows. The CSP method is a suitable candidate for extracting physical insights from reactive flows dynamics that can be employed for both the generation of simplified kinetic schemes and the calculation of smart and compact diagnostic observables. Among them, the tangential stretching rate (TSR) is an estimate of the system's driving chemical timescale that can be profitably employed for characterising the reactive flow dynamics in terms of combustion regimes and role of transport with respect to kinetics. The potentials of TSR are extensively highlighted, starting from prototypical combustion models, such as batch reactor and unsteady laminar flamelet, and getting to real-life usage on 3-dimensional direct numerical simulation datasets. The CSP mathematical foundations are then employed for mechanism simplification purposes, where small and accurate kinetic mechanisms are sought after. An existing CSP-based simplification algorithm is improved, aiming at the minimisation of the required user knowledge, which becomes a critical feature of the algorithm when dealing with new fuels. Practical applications of the revised algorithm are shown and discussed. Finally, the focus is shifted from the quest for tight accuracy in the simplified mechanisms towards a much broader question regarding confidence in detailed kinetic schemes. Uncertainty in the

kinetic model parameters, such as Arrhenius coefficients, can jeopardize the efforts spent in the reduction challenge. A new, uncertainty-aware, robust CSP simplification strategy is proposed, discussed and employed, and its robustness demonstrated in a test case involving an uncertain -in its Arrhenius pre-exponential coefficients- kinetic scheme.

Chapter 1

Introduction

The control of fire by early humans was a climax of human evolution, in both practical and cultural aspects. Some hundred thousands of years later, today, controlled fire is still at the heart of many fundamental human activities, from domestic heating to automotive, aeronautical and space engines. Despite the numerous attempts at introducing alternate energy sources, the main supplier to the world energy and power generation needs still remains chemical energy derived from combustion. When the mathematical and engineering tools began to be adequate to treat combustion in the early second half of the 20th century, the line of action was in the direction of maximizing the power outputs of combustion devices. In the last decades, the direction changed in favor of more efficient and cleaner burning, facing new challenges in terms of pollutant emissions and fuel savings, that shifted the spotlight from power maximization to the reduction of environmental impact. Formation of soot, unburnt hydrocarbons (UHC), nitrogen oxides (NO_X) and sulfur oxides (SO_X) suddenly received major attention, as well as the depletion of fossil fuels. Combustion scientists realized that the improvement of existing combustion devices architectures was not enough to address these new challenges, but instead a deeper fundamental research on combustion phenomena and alternate fuels was required.

The automotive industry is a fair example of this paradigm change. Brand new engine concepts are being studied to replace the noisy and soot/NO_X emitter diesel engine, since

these disadvantages originate at the very heart of its operational principle. One example is the stratified charged combustion engine, that exploits the reduced pollutant emission and improved efficiency of lean mixtures. Nonetheless, lean mixtures are difficult to ignite, hence richer mixtures are employed for the ignition process, stratifying the mixture from lean to rich. Another, quite conceptually different, example is the homogeneous charge compression ignition (HCCI) engine, which reduces soot/NO_X formation by having reaction taking place homogeneously within the entire engine cylinder, thanks to an elevated temperature of the reactants and a low temperature increase in the combustion process, usually at high pressure.

It becomes clear that fundamental understanding of chemically reacting flows is an essential step for enabling breakthrough advancements in propulsion technologies. Such flows are characterized by strong relationships between turbulence, mixing and chemical reactions, that interact over a wide dynamic range of space and time scales. This complexity translates into difficulties in formulating affordable predictive models, and is further aggravated by the general direction in which engines are changing because of the increasingly stringent requirements on efficiency and emissions, *e.g.* higher pressures, lower temperatures, and higher levels of dilution.

The largest computational burden comes typically from chemistry. Detailed chemical kinetic mechanisms are used to describe the transformation of reactants into products through a usually large number of elementary steps. As a consequence, such mechanisms involve a multitude of species and reactions, often acting over a wide spectrum of disparate timescales which can range from nanoseconds to minutes. Hence, combustion systems are inclined to be affected by complexity issues arising from both the dimensionality of the problem, since the number of species can easily reach the order of the 1000's in large hydrocarbons combustion, and the stiffness originating from the presence of very different timescales.

Despite the continual growth in the size, speed and availability of large computers, these two main sources of complexity heavily affect the resolution of combustion problems. Typical combustion codes necessarily need to employ turbulence modeling, such as in large eddy simulations (LES) and Reynolds-averaged Navier-Stokes simulations (RANS), and/or

reduced kinetic mechanisms, to alleviate the computational cost. Nonetheless, even if the detailed kinetic scheme were affordable, *e.g.* when simple fuels such as hydrogen or methane are involved, the associated stiffness of the governing equations requires special attention, *i.e.* in choosing the appropriate numerical methods to be employed for the integration.

Notwithstanding these complications, the tremendous growth in computational capabilities and the constant need for unconventional combustion regimes and alternative fuels are pushing towards (i) direct numerical simulations (DNS) of all the scales involved in the turbulent combustion phenomena, even with detailed chemistry, eventually capable of replacing laboratory experiments, and (ii) the development of increasingly larger kinetic mechanisms that are adequate for describing today's and next-generation fuels, which are composed of a multitude of different molecular components. These two parallel directions of development are accentuating the need for both effective numerical diagnostics capabilities that allow to face the considerable amount of information that a DNS delivers, and reliable and accurate reduced models for chemistry, that are crucial for the DNS feasibility.

The computational singular perturbation (CSP) framework offers the possibility to tackle both the necessities: it allows to analyze the system's dynamics and extract physical insights that can be employed for both the generation of simplified kinetic schemes and the calculation of smart and compact diagnostic observables. The CSP method relies on the projection of the chemical source term over a suitable orthonormal basis, yielding an alternative representation in terms of modes, which are associated to time scales. Some of the (fast) chemical time scales can be considered exhausted, or in near equilibrium, in the time frame of interest, allowing for the definition of a local subspace - the slow invariant manifold - where the system evolves according to the slow scales. Starting from this chemical space decomposition, a number of tools can be exploited with the aim of extracting information from the system's dynamics, opening the way to either model reduction or system's diagnostics. Chapter 2 introduces the CSP framework and its main mathematical foundations.

The *a-posteriori* interpretation of combustion problems is crucial when high fidelity simulations are performed. There is a widespread need to rationalize the number of observables of a large reactive flow simulation, with the aim of getting the truly relevant physical

insights and of identifying the global features of the combustion phenomena. Chapter 3 will be devoted to the definition of a number of CSP-derived tools that can be used in a post-process stage for the above purposes. In particular, the Tangential Stretching Rate will be shown to represent a valuable indicator of the combustion regime, capable of (i) estimating the truly active chemical time scale, among the wide spectrum of scales involved, (ii) characterizing the explosive/dissipative nature of the dynamics, and (iii) recognizing whether or not kinetics is the controlling process with respect to transport.

Chapter 4, instead, will tackle the mechanism simplification problem within the CSP framework. First, a well established automatic procedure for generating skeletal mechanisms will be reviewed. Next, a number of improvements to the traditional CSP algorithm will be introduced that exhibit a considerable impact on the quality of the obtained mechanisms, by minimizing the number of retained species without compromising their accuracy with respect to the detailed one.

While the need for smaller and accurate chemical schemes is constantly increasing, the growth in the complexity of combustion problems and kinetic mechanisms, supported by increased computational capabilities, can lead to a misplaced focus on tight accuracy in numerical simulations when reduced models for chemistry are employed. In other words, the efforts spent in the reduction challenge should take into account that overconfidence in the detailed kinetic scheme, which is used as a baseline/reference model, can shadow other sources of error, such as uncertainty in model parameters. Typical kinetic model parameters affected by uncertainty are the rate coefficients, which are often built out of experiments and empirical considerations. Thus, a chemical model reduction strategy that is aware of such uncertainties may be desirable, in order to ascertain the range of validity of the obtained simplified mechanisms within a probabilistic setting. This strategy is presented in chapter 5.

Chapter 2

Foundations of the CSP method

The reduction of the size and stiffness associated to a combustion problem involving large and complex chemical kinetic mechanisms is crucial to obtain accurate predictions of combustion phenomena within reasonable computational time frames. Over the past decades, a large number of reduction methods have been proposed and implemented in computer codes with the aim of simplifying complex mathematical models or to acquire understanding of the underlying physics. Among them, methods such as the Quasi Steady State Approximation (QSSA) [1, 2], the Partial Equilibrium Assumption (PEA) [3], the Intrinsic Low Dimensional Manifold (ILDM) [4, 5], the Fraser and Roussel method [6, 7, 8, 9] and the Computational Singular Perturbation (CSP) [10, 11, 12, 13] have been extensively used in several fields other than combustion, including biochemistry, enzyme kinetics, atmospheric science and economics [14, 15, 16]. These methods usually label the systems variables, *i.e.* chemical species, either as major (slow), which evolve on a low dimensional, attractive subspace, commonly referred to as "slow invariant manifold", or minor (fast), which somehow are slaved to the slow variables. The long term dynamics of the system will be governed by the dynamics on the manifold, this resulting in a general reduction of complexity, being the dimension of the manifold smaller than the original phase space dimensionality. Hence, the reduction methods generally seek the manifold, or a suitable approximation of it, to lower the overall dimension of the system and reduce its stiffness,

eventually constructing a slow system which is less complex and easier to understand.

Conventional methods such as QSSA or PEA, developed in the first half of the 20th century, rely on experience and intuition to label the quasi-steady-state species or the fast reactions, often leading to an inaccurate identification of the slow manifold. The more recent methods, such as ILDM, Fraser and Roussel, and CSP, are based on stronger geometric foundations to identify the system's asymptotic dynamics, hence are considered more reliable in the determination of the low-dimensional manifold. An exhaustive comparison of the three is given in [17].

Beside the geometrical methods, a consistent number of recent works have been developed following different approaches. Such methods seek lower-dimensional models by eliminating unimportant species/reactions, employing graph analysis [18], reaction path relations [19] and path flux analysis [20] to measure the degree of interaction among species.

This chapter will be devoted to: (i) illustrate the proper mathematical setting of reduction methods for stiff problems, (ii) briefly review the conventional reduction methods, (iii) give a thorough description of the CSP method, and (iv) extend the CSP concepts to PDE systems involving both kinetics and transport.

2.1 Reduction methods for singularly perturbed problems

A generic, spatially homogeneous kinetic system is described by a set of ODE's:

$$\frac{d\boldsymbol{y}}{dt} = \dot{\boldsymbol{y}} = \boldsymbol{g}(\boldsymbol{y}), \qquad \boldsymbol{y}(0) = \boldsymbol{y}_0, \qquad \boldsymbol{y} \in \mathbb{R}^N, \tag{2.1.1}$$

where $\boldsymbol{y}$ is a N-dimensional state vector containing the chemical species and $\boldsymbol{g}(\boldsymbol{y})$ is a generic chemical source term. Reduction methods are developed for systems which evolve on two distinct time scales, with a small parameter ϵ which is indicative of the fast/slow time scale gap in the dynamics of the system. The *singularly perturbed form* of system

(2.1.1) reads:

$$\frac{d\boldsymbol{y}_s}{dt} = \epsilon \boldsymbol{g}_s(\boldsymbol{y}_s, \boldsymbol{y}_f, \epsilon) \tag{2.1.2}$$

$$\frac{d\boldsymbol{y}_f}{dt} = \boldsymbol{g}_f(\boldsymbol{y}_s, \boldsymbol{y}_f, \epsilon), \tag{2.1.3}$$

where $\boldsymbol{y}_s \in \mathbb{R}^m$ is the vector of slow variables, $\boldsymbol{y}_f \in \mathbb{R}^n$ the vector of fast variables. The time t is usually referred to as the fast time, being the time scale on which the fast variables evolve, and the system (2.1.2)-(2.1.3) may be identified as the fast system. Defining $\tau = \epsilon t$, the system acquires the equivalent slow form:

$$\frac{d\boldsymbol{y}_s}{d\tau} = \boldsymbol{g}_s(\boldsymbol{y}_s, \boldsymbol{y}_f, \epsilon) \tag{2.1.4}$$

$$\epsilon\frac{d\boldsymbol{y}_f}{d\tau} = \boldsymbol{g}_f(\boldsymbol{y}_s, \boldsymbol{y}_f, \epsilon). \tag{2.1.5}$$

In the limit $\epsilon \to 0$, system (2.1.4)-(2.1.5) reduces to:

$$\frac{d\boldsymbol{y}_s}{d\tau} = \boldsymbol{g}_s(\boldsymbol{y}_s, \boldsymbol{y}_f, 0) \tag{2.1.6}$$

$$0 = \boldsymbol{g}_f(\boldsymbol{y}_s, \boldsymbol{y}_f, 0), \tag{2.1.7}$$

where the first equation describes the evolution of the slow variables, thus the system's long-term dynamics, and the second equation represents an algebraic constraint which confines the reduced slow system to a reduced slow manifold. It is to be noted that the explicit singularly perturbed form of system (2.1.2)-(2.1.3) is never available in complex chemical-physical systems, where the determination of the slow and fast variables and of the parameter ϵ is a substantial part of the reduction process.

2.1.1 Conventional reduction methods

Very popular and extensively used for decades, the quasi-steady-state approximation (QSSA) and the partial equilibrium approximation (PEA) are considered the conventional methods for dealing with the class of problems described in § 2.1, however they strongly rely on intuition, this characteristic making them unfeasible for large and complex kinetic problems such as those of interest today. Despite this critical weak point, studies have been

conducted in the last decade concerning their validity, their geometric interpretation and their implementation.

Both methods aim at constructing a reduced (N-M)-dimensional model of system (2.1.1) by employing M algebraic relations involving the reaction rates. Depending on the nature of these relations, the QSSA and the PEA methods can be distinguished. In particular, the QSSA presumes the specification of M components of the state vector, *i.e.* chemical species, whose rates of formation and destruction are much larger in magnitude than their difference: their net rate of change is neglected. It follows that the right-hand-sides $\boldsymbol{g}_f$ corresponding to the M quasi-steady-state species are put equal to zero, constituting the M algebraic relations of the QSSA method. These algebraic equations can be used to calculate the concentrations of the QSS-species from the concentrations of the other (non-QSS) species. The system of ODEs for the non-QSS-species and the system of algebraic equations for the QSS-species together form a coupled system of differential algebraic equations (DAE).

In the PEA method, instead, M reactions are labeled as those having their forward and backward rates much larger than the magnitude of their difference, *i.e.* they are in equilibrium, hence the algebraic relations involve the M reaction rates contained in the right-hand-sides of all the state variables. Again, this results in a DAE system.

Goussis [21] analyzed and compared the two methods, concluding that, once the variables and processes associated the most with the fast time scales are properly identified, a valid QSSA or PEA is a limit case of leading-order asymptotics, producing $O(\epsilon)$ accuracy, and that a valid QSSA is a limit case of a valid PEA. A proper identification of the fast variables/processes remains the limiting feature of this class of methods.

2.2 Computational Singular Perturbation

2.2.1 Basic CSP concepts

What follows is mainly due to Lam and Goussis [10, 13], who introduced the CSP method as a valuable mathematical tool capable of extracting physical insights on massively complex reaction systems, in contrast with the conventional methods, such as the quasi-steady-state

or the partial-equilibrium approximation, which heavily relied on experience and intuition. Consider again a spatially homogeneous chemical kinetic system whose dynamics is described by a Cauchy problem of the form:

$$\frac{d\boldsymbol{y}}{dt} = \boldsymbol{g}(\boldsymbol{y}), \qquad \boldsymbol{y}(0) = \boldsymbol{y}_0, \qquad \boldsymbol{y} \in \mathbb{R}^N. \tag{2.2.1}$$

where $\boldsymbol{y}$ is a N-dimensional state vector and $\boldsymbol{g}(\boldsymbol{y})$ is a generic chemical source term. The N-dimensional state vector $\boldsymbol{y}$ usually contains the N chemical species concentrations and the N-dimensional column vector $\boldsymbol{g}(\boldsymbol{y})$ is the overall reaction rate vector, usually defined as the matrix product between a N-by-R stoichiometric matrix and a R-dimensional reaction rate vector, where R is the number of unidirectional reactions[1]. The definition of the state vector $\boldsymbol{y}$ can be extended to include thermo-dynamic variables (temperature, pressure, internal energy, entropy, ...), this requiring a suitable generalization of the coefficients matrix, to accommodate laws of energy conservation, entropy production, and so forth[2]. A thorough definition of the set of ODEs describing a spatially homogeneous chemical kinetic system is given in Appendix A. Here, it is only important to stress that in today's complex chemical problems, N and R may be very large numbers: $O(1000)$ chemical species and $O(10000)$ chemical reactions.

The main idea behind the CSP method is to find and exploit an alternative representation for $\boldsymbol{g}(\boldsymbol{y})$, which is a non-linear function of $\boldsymbol{y}$, built by summing all the physical processes that contribute to the production/consumption of $\boldsymbol{y}$. This physical representation of $\boldsymbol{g}(\boldsymbol{y})$ is not capable to give insights on the problem more than the physical explanation of each term used to build it, namely the contribution of each reaction to the time rate of change of the species concentrations. The CSP method takes advantage of the following alternative modal representation:

$$\frac{d\boldsymbol{y}}{dt} = \boldsymbol{g}(\boldsymbol{y}) = \sum_{i=1,N} \boldsymbol{a}_i f^i, \tag{2.2.2}$$

[1] In many textbooks, the number of unidirectional reactions is denoted by $2R$, where R is the number of reversible reactions.

[2] For the sake of clarity, the number of system's variables will be always denoted as N, although in all the practical applications of this work, involving the models presented in Appendix A, the state vector includes also temperature, so that the number of variables is N+1.

which is always valid as long as $\boldsymbol{a}_i$ is a set of linearly independent column vectors. The N arbitrarily chosen column vectors $\boldsymbol{a}_i$ are called *CSP-vectors*, which span the tangent space $TC_{\boldsymbol{y}}$ at $\boldsymbol{y}$, and the set of N scalars f^i are called *amplitudes* of the CSP-modes, which are given by:

$$f^i := \boldsymbol{b}^i \cdot \boldsymbol{g}(\boldsymbol{y}). \tag{2.2.3}$$

The set of N row vectors $\boldsymbol{b}^i$ are the dual of $\boldsymbol{a}_i$, spanning the dual of the tangent space $TC^*_{\boldsymbol{y}}$, such that they satisfy the biorthonormality condition:

$$\boldsymbol{b}^i \cdot \boldsymbol{a}_i = \delta^i_j, \qquad \sum_{i=1}^{N} \boldsymbol{a}_i \boldsymbol{b}^i = I, \tag{2.2.4}$$

where I is the identity matrix. The condition (2.2.4) and the definition (2.2.3) allow to recover the original representation of system (2.2.2).

The CSP method aims at answering a number of questions, such as: how to derive a reduced reaction system which involves a smaller set of chemical species and elementary reactions? How to identify the rate-controlling reactions? How to identify the intrinsic chemical time scales and the directions in phase space along which they act? Which are the exhausted chemical time scales? These, and many more questions, can be answered by choosing a suitable set of basis vectors, thus obtaining the sought-after representation of $\boldsymbol{g}$ that allows to explore the features of the dynamical system (2.2.1).

2.2.2 The ideal basis vectors

A good set of projection basis vectors should allow to decouple the modes time evolution, so that a speed-based ordering of the modes can be done. This, in turn, will allow to exploit the time scale gap typical of the singularly perturbed problems.
The modes evolution in time can be expressed as a non-linear system of ODEs:

$$\frac{df^i}{dt} = \sum_{j=1}^{N} \Lambda^i_j f^j, \qquad \Lambda^i_j = \left(\frac{d\boldsymbol{b}^i}{dt} + \boldsymbol{b}^i \boldsymbol{J} \right) \boldsymbol{a}_j, \tag{2.2.5}$$

which follows from the time differentiation of the definition of f^i, and where $\boldsymbol{J}(\boldsymbol{y})$ is the N-by-N Jacobian matrix $(\partial g^i / \partial y_j)$ of $\boldsymbol{g}(\boldsymbol{y})$. An ideal system of basis vectors $\{\{\boldsymbol{a}_i\}; \{\boldsymbol{b}^i\}\}$ is such that the matrix Λ is diagonal, *i.e.* $\Lambda = diag(\mu_i)$. It follows that, in this case,

the system (2.2.5) is decoupled, and each mode amplitude evolves in time independently, according to:

$$\frac{df^i}{dt} = \mu_i f^i. \tag{2.2.6}$$

This, in turn, allows to define a spectrum of intrinsic local time scales as $\{1/\mu_i\}$ and to order the modes based on the values of μ_i, eventually leading to a suitable fast/slow decomposition. For linear problems where $\boldsymbol{J}$ is a constant matrix, the ideal basis vectors would be the (constant) ordered eigen-vectors of $\boldsymbol{J}$. For non-linear problems, and this is the case of reactive systems, the eigen-vectors of $\boldsymbol{J}$ are time-dependent, and they do not diagonalize Λ.

Lam and Goussis [11] proposed the so-called *CSP-refinement* procedure, which is an iterative method that weakens the coupling between fast and slow modes, supposing that a suitable criterion for the determination of the number of fast modes is available. This method produces refined basis vectors after each step that satisfy the biorthonormal relations and is a generalization of the so-called *power method* for computing eigen-vectors. It produces a block diagonal Λ when converged. Each refinement cycle was shown to increase the accuracy of the reduced model by a factor of the order of the fast/slow timescale gap [11].

In the context of this work, instead, leading order approximations of the basis vectors will be employed, these consisting in the right and left eigen-vectors of the Jacobian matrix. This approximation is the result of neglecting the term $d\boldsymbol{b}^i/dt$ in Eq. (2.2.5), which means assuming that the system is locally linear. It follows that, the inverse of the Jacobian eigenvalues λ_i will be adopted as leading order approximations of the intrinsic time scales, *i.e.* $\Lambda = diag(\lambda)$ is the eigen-value matrix of $\boldsymbol{J}$. Such leading order approximation is considered adequate for systems exhibiting a sufficiently large gap between fast and slow timescales [11].

In principle, a nondiagonal Λ introduces a certain degree of mode-mixing, which renders the discrimination between timescales ambiguous. Note that a converged refinement procedure delivers a block-diagonal Λ, which still retains couplings between modes in the fast and slow subspaces. The validity of the CSP-refined vectors, and their leading order approximation, namely the Jacobian eigen-vectors, is discussed in [22], where it is con-

cluded that the CSP vectors are not a proper set of basis vectors in presence of persistent oscillatory behaviors. However, such dynamical systems are out of the scope of the present work, although chemical kinetics systems may exhibit periodic and chaotic attractors.

2.2.3 The number of exhausted modes

The N CSP-modes in Eq. (2.2.2) are ordered so that the first ($i = 1$) mode refers to the fastest chemical time scale, as measured by the modulus of the eigen-value associated to that mode, the second ($i = 2$) mode refers to the second fastest, etc.

At any time epoch, one can partition the tangent space into the slow and fast subspaces. The criterion that determines the dimension of the fast subspace M, is based on the definition of an error vector $\boldsymbol{y}_{error}$ defined as $y^i_{err} = \epsilon^i_{rel} y^i + \epsilon^i_{abs}, i = 1, N$, where ϵ^i_{rel} and ϵ^i_{abs} are the maximum relative and absolute errors on the i-th element of the state vector $\boldsymbol{y}$ respectively. The number M of time scales which - within the limits of accuracy specified by the given error vector - are considered exhausted (in near equilibrium), is defined [23] as the largest integer lying between 1 and N that satisfies the following inequality for each $i = 1, N$:

$$\delta y^i_{fast} \approx |\tau^{M+1}_{chem} \sum_{r=1}^{M} a^i_r f^r| < y^i_{error} = \varepsilon^i_{rel} y^i + \varepsilon^i_{abs}, \tag{2.2.7}$$

where $\tau^{M+1}_{chem} = |1/\lambda_{M+1}|$ is the fastest of the slow chemical time scales. The summation[1] in Eq.(2.2.7) implicitly assumes as constant the value of the fast mode amplitudes over a time period of the order of τ^{M+1}_{chem}, with the risk of overestimating the contributions of the modes having an eigenvalue with a large negative real part. A more accurate and less conservative estimate of the fast subspace dimension is here proposed. The new estimate is built by retaining the functional dependence of f^r with time, and then approximating the amplitude evolution $f^r(t)$ with $f^r_0 e^{\lambda_r t}$, thus assuming an exponential growth/decay of $f^r(t)$ according to the corresponding positive/negative real part of its eigenvalue. Hence,

[1] The summation index r (as "rapid") is employed in place of f (as "fast") to avoid confusion with the mode amplitude symbol.

the contribution to the change of the state variables due to the fast subspace becomes:

$$\delta y^i_{fast} \approx \left| \int_0^{\tau^{M+1}_{chem}} \left(\sum_{r=1}^{M} a^i_r f^r(t) \right) dt \right| = \left| \int_0^{\tau^{M+1}_{chem}} \left(\sum_{r=1}^{M} a^i_r f^r_0 e^{\lambda_r t} \right) dt \right|, \tag{2.2.8}$$

where f^r_0 are the values of the fast mode amplitudes at the beginning of the time interval of duration τ^{M+1}_{chem}. The last integral can be solved in closed form to yield the improved criterion that determines the dimension of the fast subspace M as the largest integer that satisfies the following inequality for each component i of the state vector:

$$\delta y^i_{fast} \approx |\tau^{M+1}_{chem} \sum_{r=1}^{M} a^i_r f^r_0 \frac{1 - e^{\lambda^r \tau^{M+1}_{chem}}}{\lambda^r}| < y^i_{error} = \varepsilon^i_{rel} y^i + \varepsilon^i_{abs}. \tag{2.2.9}$$

When Eq. (2.2.9) is satisfied, then the dimension M is obtained and the following relations hold:

$$f^r \approx 0 \qquad r = 1, M \qquad . \tag{2.2.10}$$

Hence, we refer to the chemical time scales τ^r_{chem} $(r = 1, M)$ as those being "exhausted" and the corresponding modes as the "fast" modes. Note that exhausted modes occur because of cancellations of balancing reactions at equilibrium. The remaining $N - M$ time scales and modes are declared as being "slow", and are considered the currently active modes, *i.e.* the modes that give a net contribution to $\boldsymbol{g}$. The fast and slow modes span the fast and slow subspaces, respectively.

The number M of exhausted chemical time scales corresponds to the number of degrees of freedom lost by the trajectory, *i.e.* the trajectory has no components in the directions along which the exhausted time scales act, and the dimension of the manifold is $N - M$. Thus, Eq. (2.2.10) defines the slow invariant manifold (SIM), and the M algebraic constraints yield a set of M approximate equations of state.

The species most affected by these constraints are those whose axis is the most parallel to the direction along which the fast time scales act. Therefore, when a fast time scale becomes exhausted, the concentration of that species will, in essence, not change along this direction; *i.e.*, it has achieved a "directional steady-state" status. The terminology used in the CSP literature [24] refers to these species not as "steady-state" species but as "CSP radicals". The generalization of this concept will be given in § 2.2.4.

Among the slow modes, a number of modes may have a negligible contribution to $\boldsymbol{g}$. These modes are called "dormant", or "conserved". However, $f^i_{cons} \approx 0$ cannot be used as an additional constraint, such as those of Eq.(2.2.10), but rather as an information about $\boldsymbol{g}$ being frozen in specific directions. The atomic species conservation laws reveal themselves as permanent dormant modes. Note that, while in the exhausted modes the reactions participation is considerable, although the net contribution is zero, the dormant modes may have no participant at all.

Figure 1 is a sketch showing the amplitude evolutions of the different classes of modes. The green line is the amplitude of a mode which is considered exhausted over the represented timescale. The blue and red lines are two slow modes - the blue one is faster than the red one - which change considerably during the timescale of interest. The dashed black line is a permanent dormant mode, whose amplitude is always zero.

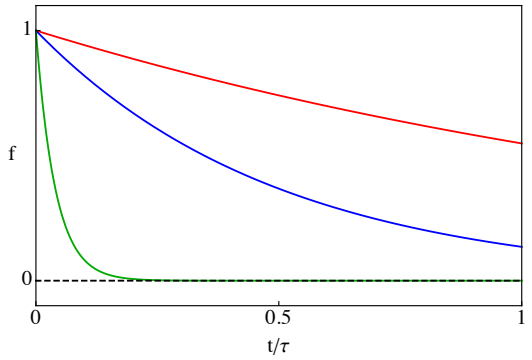

Figure 1: A sketch of the amplitude evolution of 4 representative modes: an exhausted mode (green), two slow modes (faster one is blue, slower one is red) and a permanent dormant mode (black dashed)

2.2.4 CSP pointers

The concept of CSP pointers was introduced by Lam and Goussis [10, 13] to determine which of the N ODEs could be replaced by the M algebraic constraints obtained with the

exhausted modes criterion. The CSP radicals are the species that should be solved for in the M equations of state. The identification of the radical species is done through CSP, which associates with each exhausted mode one or more species by the radical pointer, hence it does not rely on experience and/or intuition. Geometrically, the pointer is a measure of how large the mutual projection of the m-th mode is onto the k-th coordinate axis representing the k-th species, or, in other words, how "perpendicular" the k-th species axis is to the surface defined by the m-th equation of state in the phase space.

The radical pointer of the m-th mode, Q_m, is defined by the N diagonal elements of the N-by-N matrix $\boldsymbol{a}_m \boldsymbol{b}^m$:

$$Q_m = \boldsymbol{a}_m \boldsymbol{b}^m \qquad (no\ sum\ on\ m). \tag{2.2.11}$$

Because of the biorthonormality property of the basis vectors $\boldsymbol{a}_i$ and $\boldsymbol{b}^j$, defined in Eq.(2.2.4), it follows that:

$$\sum_{m=1}^{N} Q_m = AB = BA = I, \tag{2.2.12}$$

where A and B are the matrices containing the basis vectors $\boldsymbol{a}_i$ and $\boldsymbol{b}^j$, respectively, and I is the identity matrix. Hence, the system (2.2.1) may be rewritten as:

$$\frac{d\boldsymbol{y}}{dt} = \boldsymbol{g} = AB\boldsymbol{g} = \left(\sum_{m=1}^{N} Q_m \right) \boldsymbol{g}. \tag{2.2.13}$$

Defining $\boldsymbol{e}^k$ the row versor having the k-th direction in the phase space, and $\boldsymbol{e}_k$ its dual column versor, the time evolution of the k-th component of $\boldsymbol{y}$ may be expressed as:

$$\frac{dy^k}{dt} = g^k = \boldsymbol{e}^k \boldsymbol{g} = \left(\sum_{m=1}^{N} \boldsymbol{e}^k Q_m \right) \boldsymbol{g} = \sum_{i=1}^{N} \sum_{m=1}^{N} \boldsymbol{e}^k Q_m \boldsymbol{e}_i \; g^i. \tag{2.2.14}$$

Since $\sum_{m=1}^{N} \boldsymbol{e}^k Q_m \boldsymbol{e}_i = \delta_i^k$, Eq.(2.2.14) becomes:

$$\frac{dy^k}{dt} = \sum_{m=1}^{N} \boldsymbol{e}^k Q_m \boldsymbol{e}_k \; g^k, \tag{2.2.15}$$

where each term $\boldsymbol{e}^k Q_m \boldsymbol{e}_k$ is the k-th diagonal term of the m-th Q matrix. It also follows that the sum of the diagonal entries of each matrix Q_m equals unity.

The magnitude of the k-th diagonal entry of Q_m, *i.e.* $\boldsymbol{e}^k Q_m \boldsymbol{e}_k = \mathrm{diag}_k(Q_m)$, measures the

relation of the m-th mode to the k-th species. Whenever $\mathrm{diag}_k(Q_m)$ is non-small and m is declared as fast mode, then k is a CSP radical species. Note, however, that more than one CSP radical can be associated to each fast mode, but not necessarily the one with the largest pointer will be a true CSP radical. This issue may be addressed by considering the M species associated to the whole fast subspace, which is M-dimensional, instead of associating one radical species to each mode. This can be done by projecting in the k-th direction the matrix $\hat{Q}$, defined as:

$$\hat{Q}(M) = \sum_{m=1}^{M} Q_m. \tag{2.2.16}$$

Hence, the diagonal entries of $\hat{Q}$ may be sorted in descending order based on their magnitude. The first M elements will define the M radical species, the remaining N-M species will be declared as slow species, or non-radical species.

Note that, among the M radical species, there might be a number of species that contribute insignificantly to the mixture composition, either because they have not yet been produced from the reactants or because they have been entirely consumed. Such species may be declared as "trace" if their concentration is smaller than a certain tolerance and their source term is not positive. The latter constraint is needed to avoid the inclusion of true radicals, whose concentration is usually small, into the trace species pool.

Practically speaking, the CSP pointers offer the possibility of: (i) partitioning the state vector in three subsets, namely trace species, radical/fast species and non-radical/slow species, (ii) identifying the species most affected by a given mode, which is a useful tool to get insights on the physics of some interesting modes, *e.g.* the explosive mode, or the most energy-containing modes, as will be discussed in § 3.3.

2.3 Extension of CSP to non-homogeneous problems

Let us now consider a generic reactive flow system, whose dynamics is described by a set of PDEs of the form:

$$\frac{\partial \boldsymbol{y}}{\partial t} = \boldsymbol{L}_x(\boldsymbol{y}) + \boldsymbol{g}(\boldsymbol{y}), \qquad \text{BCs on } \boldsymbol{y}, \qquad \boldsymbol{y}(0) = \boldsymbol{y}_0. \tag{2.3.1}$$

where $\boldsymbol{y} \in \mathbb{R}^N$ and $\boldsymbol{g}(\boldsymbol{y})$ are defined as in Eq.(2.2.1), whereas $\boldsymbol{L}_x(\boldsymbol{y})$ represents a generic transport term such as convection and/or diffusion, or the sum of the two.

As discussed in [25], the most natural extension of the CSP concepts for a set of PDEs involves resorting to a method of line discretization which transforms the set of PDEs into a set of ODEs. However, the dimension of the space increases proportionally to the number of cells K used in the space discretization, that is the state vector lives in an extended space of dimensions $N \times K$. Moreover, the discrete eigen-system is related to the combined kinetic plus transport nature of the system, and the discrete eigenvectors are approximation of the global eigenfunction of the spatial operators. All these concepts are theoretically sound, but practically difficult to manage. Moreover their information has a global (spatially speaking) nature and do not provide local information about the flow.

Therefore, an alternative, albeit less rigorous, approach is to accept to work in the original N dimensional space defined by the kinetics only. In this context, transport affects only the amplitude of the kinetic eigen-modes but not the structure of the mode themselves. More details on how to relate reactive with reactive-diffusive time scales can be found in [25].

Thus, as discussed in [26], one can recast Eq. (2.3.1) as an expansion over the kinetic modes as follows:

$$\frac{\partial \boldsymbol{y}}{\partial t} \;=\; \boldsymbol{L}_x(\boldsymbol{y}) + \boldsymbol{g}(\boldsymbol{y}) = \sum_{i=1,N} \boldsymbol{a}_i(\boldsymbol{y}) h^i(\boldsymbol{y}), \tag{2.3.2}$$

where the modal amplitudes h^i are defined as:

$$h^i \;=\; \boldsymbol{b}^i \cdot (\boldsymbol{L}_x(\boldsymbol{y}) + \boldsymbol{g}(\boldsymbol{y}))\,. \tag{2.3.3}$$

The N CSP-modes in Eq. (2.3.2) are ordered so that the first ($i = 1$) mode refers to the fastest chemical timescale, the second ($i = 2$) mode refers to the second fastest, etc.

At any time epoch and space location, one can partition the tangent space into the slow and fast subspaces, in the very same way discussed in § 2.2.3, which is by applying the exhausted modes criterion:

$$\delta y^i_{fast} \approx |\tau^{M+1}_{chem} \sum_{r=1}^{M} a^i_r h^r_0 \frac{1 - e^{\lambda^r \tau^{M+1}_{chem}}}{\lambda^r}| < y^i_{error} = \varepsilon^i_{rel} y^i + \varepsilon^i_{abs}. \tag{2.3.4}$$

The criterion allows to determine the dimension M of the fast subspace. Note the use of the modal amplitudes h^i, instead of f^i. When the amplitudes of the M fastest modes have vanished, i.e., when the following relations hold:

$$h^r \approx 0 \qquad r = 1, M \tag{2.3.5}$$

then we will declare "exhausted" the chemical timescales τ^r_{chem} $(r = 1, M)$ and "fast" the corresponding modes. Equation (2.3.5) defines the Slow Invariant Manifold. The remaining $N - M$ timescales and modes are declared as being "slow".
It should be noted that in the case of zero transport, i.e. $\boldsymbol{L}_x = 0$, h^i translates to f^i and all the previously introduced relations are consistent with the CSP approach for ODE systems.

Note that $h^r \approx 0$ only if $(\boldsymbol{b}^i \cdot \boldsymbol{L}_x(\boldsymbol{y})) \approx -(\boldsymbol{b}^i \cdot \boldsymbol{g}(\boldsymbol{y}))$, that is, when transport and kinetics balance each other along the direction of the i-th mode at the scale defined by the i-th eigenvalue.

When $|\boldsymbol{b}^i \cdot \boldsymbol{L}(\boldsymbol{x})| \ll 1$ the mode is kinetically controlled and $h^r \approx 0$ occurs because kinetics reaches equilibrium on that scale as defined by the condition $|\boldsymbol{b}^i \cdot \boldsymbol{g}(\boldsymbol{x})| \approx 0$. This condition, as already observed in § 2.2.3, occurs because of cancellations of balancing reactions at equilibrium.

However, when $h^r \approx 0$ and $|\boldsymbol{b}^i \cdot \boldsymbol{L}_x(\boldsymbol{y})|$ is not negligible, kinetics cannot stay in equilibrium because transport drives it off equilibrium.
Also note that in an ODE system involving only kinetics, a zero (kinetic) eigenvalue, say $\lambda^i = 0$, corresponds to a mode $\boldsymbol{a}_i$ which defines a (linear) conservation law (possibly an atomic species conservation) according to the expression: $f^i_{cons} = \boldsymbol{b}^i \cdot \boldsymbol{g}(\boldsymbol{y}) \approx 0$. However, in a PDE system involving transport, it might occur that $\boldsymbol{L}_x(\boldsymbol{y})$ could have a non-negligible projection over the same mode, say $\boldsymbol{b}^i \cdot \boldsymbol{L}_x(\boldsymbol{y}) \neq 0$, so that in this circumstance the conservation law does not hold anymore $(\boldsymbol{b}^i \cdot (\boldsymbol{L}_x(\boldsymbol{y}) + \boldsymbol{g}(\boldsymbol{y})) \neq 0)$.

Chapter 3

CSP-based tools for reactive flows diagnostics

The CSP method was originally developed with the aim of extracting physical information about complex chemical kinetic systems, to be possibly employed for the generation of reduced models, the latter being capable of alleviating the computational costs associated to the resolution of the stiff and large detailed problem. Besides the model reduction task, which will be addressed in chapter 4, the computational tools that the CSP method offers can be effectively employed to get *a-posteriori* information and physical insights on combustion problems which involve complex kinetic schemes and/or interaction between chemistry and transport. The interpretation of combustion problems, especially when the computational domain and/or the number of variables, *i.e.* chemical species, are large, is a challenging task that should allow to get fundamental understanding of reactive systems' characteristics.

Today's technological advancement in computational science and the difficulties in realizing a wide class of experiments in the laboratory, are pushing towards high fidelity simulations, such as direct numerical simulations (DNS), that produce a huge quantity of information. It is therefore crucial to have computational tools that rationalize the number of observables, giving the possibility of identifying the dominating physical processes

and systematically determine a number of global combustion characteristics, such as flame structures, flame fronts, ignition nature and combustion regimes. For example, the interaction between chemistry and transport is a key aspect in combustion modeling. The Damköhler (Da) number, which is often employed to characterize the combustion regime, is the ratio of a mixing or flow time scale to a chemical time scale. The choice of a representative chemical time scale is usually a complex task which can be addressed with a recently developed CSP-based tool: the Tangential Stretching Rate [27, 28, 29].

In this chapter, a set of CSP-based tools is presented, including (i) the CSP participation indices, that quantify the participation of a chemical reaction to a CSP mode, (ii) the Entropy participation indices, that estimate the entropy production associated to each chemical reaction, and (iii) the Tangential Stretching Rate, in both the ODE and PDE versions, which is a powerful indicator of the truly active time scale of the system, and in turn a useful tool to characterize the combustion regime and the associated dominant physical processes. Alongside the theoretical foundations of these tools, a number of practical applications will be presented. In particular, three TSR applications to a homogeneous problem, a 1-D non-premixed flame and a 3-D turbulent premixed flame, respectively, will be shown to highlight the diagnostics capabilities of the tool.

3.1 CSP participation indices

The CSP participation index provides an estimate of the participation of a given reaction to a mode. This index is built recalling that the amplitude of the i-th mode f^i can be expanded as:

$$f^i \;=\; \boldsymbol{b}^i \cdot \boldsymbol{g}(\boldsymbol{y}) = \sum_{k=1}^{R} \boldsymbol{b}^i \cdot \boldsymbol{S}_k r^k = \sum_{k=1}^{R} \beta_k^i, \tag{3.1.1}$$

where $\boldsymbol{g}$ is expressed in terms of stoichiometric vectors $\boldsymbol{S}_k$ and net reaction rates r^k according to the homogeneous model problem defined in Appendix A, and R is the number of unidirectional reactions. Then the CSP participation index P_k^i can be introduced in order to measure the relative contribution of the k-th reaction to the i-th mode amplitude

[30, 31]:

$$P_k^i = \frac{\beta_k^i}{\sum_{k'=1}^{R} |\beta_{k'}^i|}. \tag{3.1.2}$$

This index can be useful if one is interested in having physical insights about a specific mode, *e.g.* the explosive mode or some sort of energy carrying mode, such as the ones that will be introduced in § 3.3. In the next section, an application will be shown where the CSP participation indices are employed to identify the chemical reactions involved in exceedingly fast modes.

3.1.1 Using the CSP P. I. to improve kinetic mechanisms

Chemical kinetics mechanisms design is a complex and challenging process, that involves the definition of stoichiometries and thermochemical data for each of the reaction steps. Several computer codes and automated procedures have been developed in the last decades to improve and possibly replace the complicated manual generation of mechanisms that historically represented the state of the art in this field [32]. However, today's fuels used both in aircraft and car engines are composed of a multitude of different molecular components, whose physical and chemical properties are not fully known, and such fuels are often represented by surrogates. The kinetic mechanisms that are used to model such fuels are designed to reproduce certain physical or chemical properties of the blend, such as ignition delay times, laminar burning velocities or pollutants formation [33]. Mechanisms of this kind, typically including thousands of species, may generate chemical dynamics characterized by unphysical timescales, arising from extremely fast kinetics eigen-modes. In this section, it will be shown how the reactions that cause such unphysical scales can be identified, relying on the CSP method and the CSP participation index, which reveals those responsible of the modes associated to the extremely fast timescales.

The investigation of hyper-fast timescales and their mostly contributing chemical reactions is tested on an auto-ignition problem of an homogeneous, isobaric reactor. The homogeneous reactor model is described in Appendix A. The mixture is a stoichiometric air-gasoline-butanol blend whose fuel composition - in % mole - is summarized in Table 3.1 and whose initial condition is T=900 K, p = 10 bar.

Table 3.1: Mixture composition

Component	% mole
iso-octane	35.19
n-heptane	8.02
toluene	29.23
n-butanol	27.56

The detailed mechanism employed for the auto-ignition problem is a 2484-species, 10368-reactions, referred to as "TRF+dodecane+butanol", built on the Aramcomech 1.3 base chemistry [34], whose development is still in progress. Time accurate solutions of the auto-ignition problem are obtained by means of the CSPTk package [35], which integrates in time Eq. (A.1.1) using CVODE [36] and where the thermo–kinetic databases are parsed and handled using the TChem package [37]. The CSP analysis is performed with the CSPTk package as well.

In the pictures that follow, a logarithmic version of the eigenvalues of $\boldsymbol{J}$ is employed, following [29]:

$$\Lambda_i := \mathrm{Sign}(\lambda_i) \cdot \mathrm{Log}_{10}|\lambda_i|, \tag{3.1.3}$$

so as to appreciate the order of magnitude of both the positive and negative eigenvalues in the same figure.

Figure 2(a) shows the evolution of eigenvalues Λ_i and temperature against the number of integration timestep, computed with the aforementioned mechanism. The most concerning issue is the presence of eigenvalues with high or very high modulus, which reaches the order of 10^{27} in the first part of the ignition. We define as hyper-fast those timescales that correspond to eigenvalues, both positive and negative, whose modulus is greater than 10^{15}. These large eigenvalues, corresponding to extremely fast timescales, are unphysical, being shorter than the chemical bonds vibration scale, and may be the cause of prohibitively small integration time steps or, in the vast majority of the cases, may prevent the convergence to a solution. Also, they may be the root cause of a wrong identification of the fast/slow subspaces in a CSP context, *i.e.* for analysis and/or model reduction purposes. As an

example, it may happen that the fast subspace is confined to these extremely fast modes only, losing the opportunity to take advantage of any sort of model reduction. Moreover, the noisy behavior in the positive half-plane of Fig. 2(a) can be attributed to the numerical round-off due to the larger-than-double-precision spectral range. With the help of the CSP participation indices, defined in Eq. (3.1.2), we are able to identify the reactions that contribute the most to the modes associated to the hyper-fast timescales, which are summarized in Table 3.2.

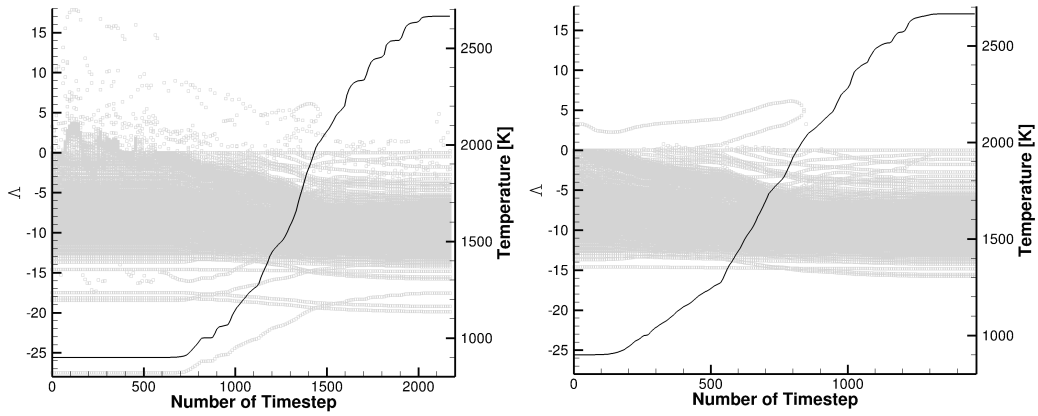

(a) Original mechanism (b) Mechanism after reactions removal

Figure 2: Eigenvalues (in Λ formulation) and temperature evolution against number of integration timestep

The same auto-ignition problem is solved again after the removal of the 7 reactions of Table 3.2 from the detailed mechanism. Figure 2(b) shows the resulting evolution of eigenvalues Λ_i and temperature against the number of integration timestep. The eigenvalues in modulus are always smaller than 10^{15}. This, in turn, allows the solver to take less timesteps to converge. Moreover, the eigenvalues evolution appears smoother, especially in the positive half-plane, where a couple of merging positive eigenvalues is clearly distinguishable among all the other -negative- eigenvalues, resembling a well-known behavior in auto-ignition problems [28].

The removal of the reactions does not appear to be pivotal in the replication of the

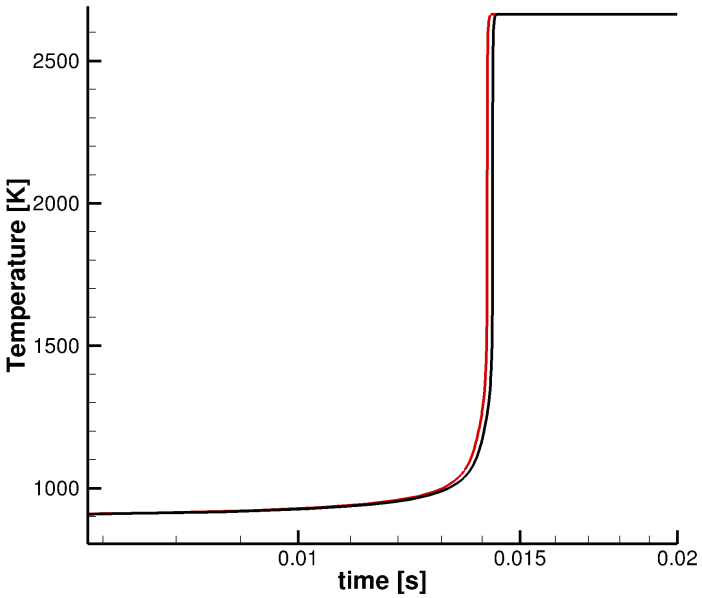

Figure 3: Temperature evolution in time with the original mechanism (red) and cleaned mechanism (black)

Table 3.2: Reactions mostly contributing to hyper-fast modes

CH2O+HO2 ↔ OCH2O2H
C5H92-4+HO2 ↔ C5H9O2-4+OH
C5H92-4+CH3O2 ↔ C5H9O2-4+CH3O
C5H92-4+C2H5O2 ↔ C5H9O2-4+C2H5O
C5H92-4+O2 ↔ C5H92O2-4
C3H6OH-3OOH-1+O2 ↔ C3H6OH-3OOH-1O2
C3H6OH-1OOH-3+O2 ↔ C3H6OH-1OOH-3O2

physical behavior of the system: fig. 3 shows the temperature evolution in time obtained with the two mechanisms, highlighting a negligible difference in the ignition delay time.

The solver performance are also evidently affected by the stiffness removal: CVODE performed the second integration with less than 40% of the CPU time required for the original mechanism, employing 67% of the number of iterations.

It should be stressed that the key feature of the present strategy is the identification of the reactions which are responsible for the unphysical scales. The removal of these reactions is a brute-force solution to the problem. A wiser approach would be to revise the Arrhenius parameters associated to those reactions in order to get a well-behaving system, without loosing the affected chemical pathways.

It is also important to highlight that a comprehensive analysis campaign on different initial conditions and/or other model problems is needed to inspect all the possible pathways that the detailed mechanism offers.

3.2 Entropy participation indices

The combination of simple thermodynamics principles, such as the mixture entropy definition and its time variation, and the CSP concepts outlined in chapter 2, allows to construct a framework in which the ideas of exhausted modes and reactions participation to the dynamics are reformulated in terms of contribution - of either a subspace or a single reaction - to the entropy production. This allows to develop additional tools, such as the entropy participation indices (EPI), or alternative criteria to determine the subspaces dimensions. In particular, the EPIs will be employed in chapter 4 in the context of model reduction, although they are perfectly suitable for straightforward diagnostics in identifying the dominating (in the entropy production sense) chemical processes. On the other hand, the entropy-based subspaces criteria have been profitably employed in the context of adaptive model reduction (G-Scheme) [38], showing improved stability with respect to the criteria introduced in chapter 2.

The first principle of non-equilibrium thermodynamics states that there exists an extensive variable, the internal energy U, whose variation in a open system, *i.e.* with energy

and matter exchange with the outside, is:

$$dU = \delta Q - \delta W + \sum_{j=1}^{N} \mu_j dN_j, \tag{3.2.1}$$

where μ_j is the chemical potential per molar units of the j-th species defined as

$$\mu_j(T, p_j) := H_j(T) - TS_j(T, p_j), \tag{3.2.2}$$

p_j is the partial pressure, N_j is the number of moles of the j-th species and H_j is the species enthalpy per molar units. The internal energy U is a function of state, for example: $U = U(p, V, N_j)$.

The second principle states that there exists an extensive variable, the entropy S, which is also a state function, whose variation in a closed system is:

$$Tds \geq \delta Q, \tag{3.2.3}$$

where the equality holds for reversible processes only. The entropy variation dS can be split into the sum of two contributions, namely $d_{int}S$ which is the variation due to internal processes, and $d_{ext}S$ which is due to interactions with the outside.

Since U is a state function, its variation does not depend on the process and one may compute heat and work exchange as if they were reversible:

$$\delta Q = Tds, \qquad \delta W = pdV \tag{3.2.4}$$

so that:

$$dU = TdS - pdV + \sum_{j=1}^{N} \mu_j dN_j, \tag{3.2.5}$$

which is the definition of the differential EOS of the kind $U = U(S, V, N_j)$. It follows that:

$$dS = \frac{1}{T} dU + \frac{p}{T} dV - \frac{1}{T} \sum_{j=1}^{N} \mu_j dN_j. \tag{3.2.6}$$

A way to easily compute the entropy of a mixture is by means of the enthalpy. Introducing the enthalpy, a function of state defined as: $H = U + pV$, differentiating and using the EOS $U = U(S, V, N_j)$:

$$dH = dU + pdV + Vdp = TdS + Vdp + \sum_{j=1}^{N} \mu_j dN_j. \tag{3.2.7}$$

It follows that, for a single species:

$$TdS_i = dH_i - Vdp_i, \tag{3.2.8}$$

and, being $dH_i = c_{p_i}(T)dT$ and $V = \frac{\mathcal{R}TN_i}{p_i}$:

$$S_i(T, p_i) = S_{i_{ref}} + \int_{T_{ref}}^{T} c_{p_i}(T)\frac{dT}{T} - \mathcal{R}N_i log\frac{p_i}{p_{ref}}. \tag{3.2.9}$$

For a mixture:

$$TdS = dH - Vdp - \sum_j \mu_j dN_j, \tag{3.2.10}$$

so that:

$$S(T, p, X_i) = \sum_i S_{i_{ref}} X_i + \sum_i X_i \int_{T_{ref}}^{T} \bar{c_p}(T)\frac{dT}{T} - \mathcal{R}log\frac{p_i}{p_{ref}} - \mathcal{R}\sum_i X_i log X_i. \tag{3.2.11}$$

This mixture entropy is due to both internal and external processes. If one wants to compute the entropy due to internal processes only, the following may be used:

$$d_{int}S = -\frac{1}{T}\sum_{j=1}^{N} \mu_j dN_j. \tag{3.2.12}$$

In isolated systems, where there is no interaction at all with the surroundings, $d_{ext}S = 0$ and the overall entropy production equals the one due to $d_{int}S$, whereas the presence of heat exchange, even if there is not matter exchange with the outside, makes the term $d_{ext}S$ different from zero. Furthermore, it can be proved that S_{int} has a maximum at equilibrium.

Dividing by dt the entropy differential EOS, and considering isolated systems, it reads:

$$\frac{dS}{dt} = -\frac{1}{T}\sum_{j=1}^{N} \mu_j \frac{dN_j}{dt}. \tag{3.2.13}$$

In the above formulation, S is considered extensive (in SI units it is J/K). In specific per-unit-mass terms, it becomes:

$$\frac{ds}{dt} = -\frac{1}{T}\sum_{j=1}^{N} \mu_j(T, p_J)\dot{\omega}_j(p, T, N_j), \tag{3.2.14}$$

where, according to the homogeneous reactor model described in Appendix A:

$$\frac{dN_j}{dt} = \dot{\omega}_j(p, T, N_j) = \sum_{k=1}^{R} \boldsymbol{S}_k r^k \qquad \boldsymbol{S}_k := (\Delta\nu_j)_k \qquad r^k\,(p, T, N_j) := r_f^k - r_b^k. \tag{3.2.15}$$

Another way to express the time variation of the mixture specific entropy is by means of the gradient of s in the chemical composition space:

$$\nabla s = -\frac{\mu^T}{T}, \tag{3.2.16}$$

which becomes, in component-wise form:

$$\left(\frac{\partial s}{\partial N_j}\right) = -\frac{\mu_j\left(T, p_j\right)}{T} = -\frac{H_j(T) - TS_j\left(T, p_j\right)}{T} = S_j\left(T, p_j\right) - \frac{H_j(T)}{T}, \tag{3.2.17}$$

so that the entropy variation can be expressed as:

$$\frac{ds}{dt} = \sum_{j=1}^{N}\left(\frac{\partial s}{\partial N_j}\right)\frac{dN_j}{\mathrm{dt}} = -\frac{1}{T}\sum_{j=1}^{N}\mu_j\left(T, p_j\right)\dot{\omega}_j\left(p, T, [N_j]\right) = -\frac{\mu^T}{T}\cdot\dot{\omega}. \tag{3.2.18}$$

Now, a suitable timescale partitioning of the RHS may be of interest, such as the fast/slow decomposition:

$$\frac{dN}{\mathrm{dt}} = \sum_{k=1}^{R}\left(P_{\mathrm{fast}}\boldsymbol{S}_k\right)r^k + \sum_{k=1}^{R}\left(P_{\mathrm{slow}}\boldsymbol{S}_k\right)r^k, \tag{3.2.19}$$

where $P_{\mathrm{fast}} := A_{\mathrm{fast}}B^{\mathrm{fast}}$ and $P_{\mathrm{slow}} := A_{\mathrm{slow}}B^{\mathrm{slow}}$ are subspaces projection matrices, built as in § 2.2.4. The use of this partitioning in the entropy variation expression leads to:

$$\frac{ds}{dt} = \sum_{j=1}^{N}\frac{\partial s}{\partial N_j}\frac{dN_j}{\mathrm{dt}} = \sum_{j=1}^{N}\left(-\frac{\mu_j\left(T, p_j\right)}{T}\right)\sum_{k=1}^{R}\left(P_{\mathrm{fast}}\boldsymbol{S}_k\right)r^k + \sum_{k=1}^{R}\left(P_{\mathrm{slow}}\boldsymbol{S}_k\right)r^k. \tag{3.2.20}$$

Thus, one can project the entropy production into the two subspaces, obtaining the entropy time-variations due to either the fast or slow subspace. This partitioning naturally leads to the definition of participation indices to the entropy production. Considering a generic subspace *sub*:

$$\begin{aligned}\frac{\mathrm{ds_{sub}}}{\mathrm{dt}} = \sum_{k=1}^{R}\left(-\frac{\mu^T}{T}\cdot P_{\mathrm{sub}}\right)\boldsymbol{S}_k r^k = -\sum_{k=1}^{R}\left(\frac{\mu^T}{T}\cdot A_{\mathrm{sub}}\right)\left(B^{\mathrm{sub}}\boldsymbol{S}_k r^k\right) = \\ = -\sum_{k=1}^{R}\left(\frac{\mu^T}{T}\cdot A_{\mathrm{sub}}\right)f_{\mathrm{sub}},\end{aligned} \tag{3.2.21}$$

with:

$$f_{\mathrm{sub}} := B^{\mathrm{sub}}\boldsymbol{S}_k r^k, \tag{3.2.22}$$

the entropy participation index is defined as:

$$\mathrm{EPi}^k_{\mathrm{subspace}} := \frac{\nabla s \cdot P_{\mathrm{sub}} \boldsymbol{S}_k r^k}{\sum_{kk=1}^{R} |\nabla s \cdot P_{\mathrm{sub}} \boldsymbol{S}_{kk} r^{kk}|} = \frac{(\nabla s \cdot A_{\mathrm{sub}}) \left(B^{\mathrm{sub}} \boldsymbol{S}_k\right) r^k}{\sum_{kk=1}^{R} |(\nabla s \cdot A_{\mathrm{sub}}) \left(B^{\mathrm{sub}} \boldsymbol{S}_{kk}\right) r^{kk}|}. \quad (3.2.23)$$

The reactions most contributing to a subspace are those with a large $\mathrm{EPi}^k_{\mathrm{sub}}$, that is reactions with a large projection over the subspace ($f_{\mathrm{sub}} = B^{\mathrm{sub}} \boldsymbol{S}_k r^k \not\ll 0$), which in turn has a large projection over the entropy gradient.

Once a modal decomposition is available for the entropy production in terms of the CSP basis vectors, that is:

$$\frac{ds}{dt} = \dot{s} = \sum_{j=1}^{N} (\nabla s \cdot a_j) f^j = \sum_{j=1}^{N} (-\frac{1}{T} \sum_{i=1}^{N} \mu_i a^i_j) f^j = \sum_{j=1}^{N} \sigma_j f^j \quad (3.2.24)$$

can be thought of a sum of slow and fast (exhausted) modes:

$$\frac{ds}{dt} = \sum_{r=1}^{M} \sigma_r f^r + \sum_{s=M+1}^{N} \sigma_s f^s. \quad (3.2.25)$$

The CSP manifold is the locus of the phase space where the system vector field bears no projection onto the fast subspace thus lying entirely in the slow subspace. This implies that also its projection on the gradient of s lies in the slow subspace, meaning that there is no entropy production due to exhausted modes. This translates into:

$$\sum_{r=1}^{M} \sigma_r f^r \approx 0, \quad (3.2.26)$$

so that the relevant entropy contribution is due to the slow modes only:

$$\frac{ds}{dt} \approx \sum_{s=M+1}^{N} \sigma_s f^s. \quad (3.2.27)$$

Thus, M is defined as the largest integer between 1 and N which satisfies the following inequality:

$$\sum_{r=1}^{M} \left| \sigma_r f^r (e^{(\lambda_r \cdot \tau^{M+1})} - 1) \lambda_r \right| < s_{error}, \quad (3.2.28)$$

which means that each mode contributes to the entropy production with its own time integral of $\dot{s}$ over $\delta t = \tau^{M+1}$, which is the smallest timescale of the slow modes, and that the sum of the fast modes contributions should be smaller than a certain tolerance

indicated by s_{error}. A order zero approximation for the time integral would consider the mode amplitudes as constants and equal to f, so that:

$$\delta s_j = \tau_{M+1} \sigma_r f^r. \tag{3.2.29}$$

One may want to compute the time integral with a better approximation of the variation of f during the time interval. Thus, one may consider the time evolution of the mode amplitude as

$$f_r(t) = f_{r_0} e^{\lambda_r t}, \tag{3.2.30}$$

whose integral between zero and τ^{M+1} is

$$f_{r_0} \frac{e^{\lambda_r \tau^{M+1}} - 1}{\lambda_r}, \tag{3.2.31}$$

where f_{r_0} is the amplitude of the r-th mode at the present timestep.
The quantity s_{error} represents the integration error on s, which is

$$s_{error} = \epsilon_{rel} \frac{s}{s_0} + \epsilon_{abs}, \tag{3.2.32}$$

where the normalization of the entropy with its initial value is needed for consistency with the integration tolerances which are usually specified for the chemical species that have values between 0 and 1.

A similar approach may be used to compute the dimension of another subspace contained in the slow subspace, namely the *active* subspace, which may be defined by the modes contributing the most to the entropy production at each timestep. Given that the fast subspace, which comprises the exhausted modes, does not appreciably participate to the entropy production, and that the slow subspace, to be intended as what remains out of the active subspace, does not participate too, the active modes share all the entropy production at each point, so that

$$\frac{ds}{dt} \approx \sum_{k=M+1}^{H} \sigma_k f^k, \tag{3.2.33}$$

where H is the largest integer that satisfies

$$\sum_{k=M+1}^{H} \left| \sigma_k f^k \right| < \theta \cdot \dot{s}, \tag{3.2.34}$$

where θ is usually large, *i.e.* 0.99, and $\dot{s}$ can be computed as the sum of all the modes projected onto the gradient of s. Even in this case, the integral approach for the definition of H, as already seen for M, may be employed.

3.3 Tangential Stretching Rate

First introduced in [27], the stretching-based diagnostics of dynamical systems was developed to compute the normal stretching rate spectrum, and the corresponding set of directions of maximum normal stretching restricted to the normal subspace, and then used for performing a local classification of the slow and fast modes of the dynamics. Subsequently, in [28], the concept of tangential stretching rate was exploited to characterize the most energetic scale developing in the system. A whole mathematical framework has been established to analyze complex systems, even in presence of transport phenomena beside chemical kinetics.

The challenge of identifying combustion characteristics, ignition structures, flame regions and combustion regimes in massive DNS outputs is of critical importance today. Beside the TSR, the chemical explosive mode analysis (CEMA), developed by Lu et al. [39], was proposed to investigate the system's behavior through the identification of the contribution of species and temperature to the explosive mode. However, while CEMA restricts its analysis to the fastest explosive mode, the TSR takes into account the contribution of all the modes in assessing the system's driving timescale. A thorough comparison between TSR and CEMA is given in [28].

In the followings, the theory of tangential stretching rate will be recalled, then its extension to PDE systems will be proposed. Three novel TSR applications will be shown, respectively, to a homogeneous problem, a 1-D non-premixed flame and a 3-D turbulent premixed flame.

3.3.1 Theory of the Tangential Stretching Rate

Consider the chemical kinetic system of Eq. 2.2.1, whose dynamics is described by a Cauchy problem of the form:

$$\frac{d\boldsymbol{y}}{dt} = \boldsymbol{g}(\boldsymbol{y}), \qquad \boldsymbol{y}(0) = \boldsymbol{y}_0, \qquad \boldsymbol{y} \in \mathbb{R}^N. \tag{3.3.1}$$

The state vector $\boldsymbol{y}$ can be identified with the species concentration vector, the vector field $\boldsymbol{g}(\boldsymbol{y}) = S\mathbf{r}(\boldsymbol{y})$ with the species reaction rate vector, S with the stoichiometric coefficients matrix, $\mathbf{r}(\boldsymbol{y})$ with the net reaction rates vector, and $\boldsymbol{y}_0$ with the initial concentrations vector.

Now, consider two nearby initial conditions, $\boldsymbol{y}_{0,1}$ and $\boldsymbol{y}_{0,2}$, for the point dynamics of Eq. (3.3.1) , such that:

$$\boldsymbol{y}_{0,2} - \boldsymbol{y}_{0,1} = \boldsymbol{\epsilon} \tag{3.3.2}$$

with $\boldsymbol{\epsilon}$ a small (vector) perturbation. Eq. (3.3.1) will generate two trajectories $\boldsymbol{y}_1(t)$ and $\boldsymbol{y}_2(t)$. Next, the vector $\boldsymbol{v}(t)$ may be defined as follows:

$$\boldsymbol{v}(t) := \lim_{|\boldsymbol{\epsilon}|\to 0} \frac{(\boldsymbol{y}_2 - \boldsymbol{y}_1)}{|\boldsymbol{\epsilon}|}. \tag{3.3.3}$$

By construction, the vector $\boldsymbol{v}(t)$ belongs to the tangent bundle at $\boldsymbol{y}_{0,1}$. The vector $\boldsymbol{v}(t)$ is a scaled measure, at time t, of the difference between the two trajectories emanating from the two initial conditions.

Derivation of the Vector Dynamics Equation

The point dynamics applied to two initial conditions that satisfy Eq. (3.3.2) provides the following ODEs:

$$\frac{d\boldsymbol{y}_1}{dt} = \boldsymbol{g}(\boldsymbol{y}_1), \qquad \boldsymbol{y}_1(0) = \boldsymbol{y}_{0,1} \tag{3.3.4}$$

and

$$\frac{d\boldsymbol{y}_2}{dt} = \boldsymbol{g}(\boldsymbol{y}_2), \qquad \boldsymbol{y}_2(0) = \boldsymbol{y}_{0,2}. \tag{3.3.5}$$

Subtracting Eq. (3.3.4) from Eq. (3.3.5) yields:

$$\frac{d\,(\boldsymbol{y}_2 - \boldsymbol{y}_1)}{dt} = \boldsymbol{g}(\boldsymbol{y}_2) - \boldsymbol{g}(\boldsymbol{y}_1), \qquad \boldsymbol{y}_2(0) - \boldsymbol{y}_1(0) = \boldsymbol{\epsilon}. \tag{3.3.6}$$

Expanding in a Taylor series $\boldsymbol{g}(\boldsymbol{y}_2)$ about $\boldsymbol{y}_1$, we obtain

$$\begin{aligned}\frac{d\,(\boldsymbol{y}_2-\boldsymbol{y}_1)}{dt} = \\ \left\{\boldsymbol{g}(\boldsymbol{y}_1)+\left.\frac{\partial \boldsymbol{g}(\boldsymbol{y})}{\partial \boldsymbol{y}}\right|_{\boldsymbol{y}_1}(\boldsymbol{y}_2-\boldsymbol{y}_1)+O(|\boldsymbol{y}_2-\boldsymbol{y}_1|^2)\right\}-\boldsymbol{g}(\boldsymbol{y}_1),\\ \boldsymbol{y}_2(0)-\boldsymbol{y}_1(0)=\boldsymbol{\epsilon}\end{aligned} \tag{3.3.7}$$

to yield the evolution equation for the difference between the two point dynamics in the tangent space $\mathcal{T}_{\boldsymbol{y}_1}$ of $\boldsymbol{y}_1$:

$$\begin{aligned}\frac{d\,(\boldsymbol{y}_2-\boldsymbol{y}_1)}{dt} = \boldsymbol{J}_{\boldsymbol{g}}(\boldsymbol{y}_1)\cdot(\boldsymbol{y}_2-\boldsymbol{y}_1)+O(|\boldsymbol{y}_2-\boldsymbol{y}_1|^2),\\ \boldsymbol{y}_2(0)-\boldsymbol{y}_1(0)=\boldsymbol{\epsilon}\end{aligned} \tag{3.3.8}$$

where

$$\boldsymbol{J}_{\boldsymbol{g}}(\boldsymbol{y}_1) := \left.\frac{\partial \boldsymbol{g}(\boldsymbol{y}(t))}{\partial \boldsymbol{y}}\right|_{\boldsymbol{y}_1} \tag{3.3.9}$$

is the Jacobian matrix of the vector field $\boldsymbol{g}(\boldsymbol{y})$ evaluated at $\boldsymbol{y}_1$. It is defined at all times by solving the point dynamics, Eq. (3.3.4), for the initial condition in $\boldsymbol{y}_{0,1}$.

To obtain the vector dynamics equation, Eq. (3.3.8) is first scaled by the norm of the difference between the two initial conditions to obtain

$$\frac{d}{dt}\frac{(\boldsymbol{y}_2-\boldsymbol{y}_1)}{|\boldsymbol{\epsilon}|} = \boldsymbol{J}_{\boldsymbol{g}}(\boldsymbol{y}_1)\cdot\frac{(\boldsymbol{y}_2-\boldsymbol{y}_1)}{|\boldsymbol{\epsilon}|}+\frac{O(|\boldsymbol{y}_2-\boldsymbol{y}_1|^2)}{|\boldsymbol{\epsilon}|}. \tag{3.3.10}$$

If the vector field is smooth (Lipschitz continuous), then the Gronwall's inequality holds for any time t:

$$\left|\boldsymbol{y}_{0,2}-\boldsymbol{y}_{0,1}\right| = |\boldsymbol{\epsilon}| \quad \Rightarrow \quad |\boldsymbol{y}_2-\boldsymbol{y}_1| \leqslant |\boldsymbol{\epsilon}|\, e^{\mathcal{L}\,t} \tag{3.3.11}$$

with $\mathcal{L}$ a suitable Lipschitz constant. Subsequently, the second term vanishes under the limit $|\boldsymbol{\epsilon}| \to 0$, i.e., for any finite time t, $O(|\boldsymbol{y}_2-\boldsymbol{y}_1|^2)/|\boldsymbol{\epsilon}| = O(|\boldsymbol{\epsilon}|^2\, e^{\mathcal{L}t})/|\boldsymbol{\epsilon}| \to 0$. Therefore, Eq. (3.3.10) provides the sought-after vector dynamics equation:

$$\frac{d\boldsymbol{v}}{dt} = \boldsymbol{J}_{\boldsymbol{g}}(\boldsymbol{y}_1)\cdot\boldsymbol{v}, \qquad \boldsymbol{v}(0)=\mathbf{1}, \tag{3.3.12}$$

where $\boldsymbol{J}_{\boldsymbol{g}}(\boldsymbol{y}_1)$ is the Jacobian of the vector field $\boldsymbol{g}$ evaluated along the reference trajectory as defined in (3.3.9), and $\mathbf{1}$ is a unit vector at $\boldsymbol{y}_0$ taken along any direction.

The vector dynamics of $\boldsymbol{v}$ described by Eq. (3.3.12) can be solved only after the integration of Eq. (3.3.1) will make available the point dynamics $\boldsymbol{y}_1(t)$ required to evaluate $\boldsymbol{J_g}(\boldsymbol{y}_1)$. It is emphasized that $\boldsymbol{v} \neq d\boldsymbol{y}/dt$; instead, $\boldsymbol{v}$ provides a measure of the distance between trajectories.
To summarize:

- the dynamics of a small perturbation in $\boldsymbol{y}$ evolves exactly according with Eq. (3.3.8), and approximately with the linear dynamic system (3.3.12)
- the dynamics of any vector of unit size in the tangent bundle of $\boldsymbol{y}_{0,1}$ evolves exactly according to the linear dynamics (3.3.12).

Derivation of the Vector Norm Dynamics Equation

The norm v of the vector $\boldsymbol{v}$ is defined as $v = \sqrt{\boldsymbol{v} \cdot \boldsymbol{v}}$, and its rate of change represents the overall rate of production/consumption of intermediate and product species due to reactions. The equation for the time evolution of v is readily found by taking the scalar product of the left- and right-hand side of Eq. (3.3.12) with $\boldsymbol{v}$, and reads

$$\frac{dv}{dt} = \left(\frac{\boldsymbol{v} \cdot \boldsymbol{J_g} \cdot \boldsymbol{v}}{v^2} \right) v, \qquad v(0) = 1. \tag{3.3.13}$$

The rate at which v changes (grows/shrinks) with time is governed by the quadratic form enclosed by the parentheses on the right hand side of Eq. (3.3.13). It is thus proper to name this coefficient "the (local) rate of stretching of the dynamics," evaluated along the direction identified by the unit vector $\tilde{\boldsymbol{u}} := \boldsymbol{v}/v$ and defined as

$$\boldsymbol{\omega}_{\tilde{\boldsymbol{u}}} := \tilde{\boldsymbol{u}} \cdot \boldsymbol{J_g} \cdot \tilde{\boldsymbol{u}}. \tag{3.3.14}$$

The (local) stretching rate $\boldsymbol{\omega}_{\tilde{\boldsymbol{u}}}$ takes positive/negative values when the dynamics acts so as to stretch/shrink the initial unit vector.

Introducing the stretching rates

In Adrover, et al. [27], it was introduced (i) the tangential stretching rate (TSR) by setting

$$\tilde{\boldsymbol{\tau}} := \boldsymbol{g}/\mathrm{g}, \qquad \text{with} \qquad \mathrm{g} = |\boldsymbol{g}|, \tag{3.3.15}$$

which spans the vector field direction, and (ii) $N-1$ normal stretching rates spanning the orthogonal complement of the vector field subspace. In a two-dimensional system (the simple model of immediate interest), the unit normal vector is obtained as $\tilde{\mathbf{n}}(\boldsymbol{y}) = \{\tilde{\boldsymbol{\tau}}_2(\boldsymbol{y}), -\tilde{\boldsymbol{\tau}}_1(\boldsymbol{y})\}$. One thus obtains the following definitions of tangential, $\omega_{\tilde{\boldsymbol{\tau}}}$, and normal, $\omega_{\tilde{\mathbf{n}}}$, stretching rates:

$$\omega_{\tilde{\boldsymbol{\tau}}} := \tilde{\boldsymbol{\tau}} \cdot \boldsymbol{J_g} \cdot \tilde{\boldsymbol{\tau}} \qquad \omega_{\tilde{\mathbf{n}}} := \tilde{\mathbf{n}} \cdot \boldsymbol{J_g} \cdot \tilde{\mathbf{n}}. \tag{3.3.16}$$

For $\omega_{\tilde{\boldsymbol{\tau}}}$ ($\omega_{\tilde{\mathbf{n}}}$) > 0, the tangential (normal) perturbations are amplified, while for $\omega_{\tilde{\boldsymbol{\tau}}}$ ($\omega_{\tilde{\mathbf{n}}}$) $<$ 0 they are damped.

However, this definition based on the local Jacobian degenerates when the trajectory crosses a region of complex eigenvectors. To overcome this shortcoming, the TSR definition will be combined with the eigen-decomposition of the Jacobian matrix of the vector field as discussed in the following section.

Stretching rates and eigenvalues

The Jacobian of the vector field can be always decomposed as $\boldsymbol{J_g} = A \cdot \Lambda \cdot B$, where $A = \{\boldsymbol{a}_j\}_{j=1,N}$ and $B = \{\boldsymbol{b}^i\}_{i=1,N}$ are the right and left normalized eigenvector matrices of $\boldsymbol{J_g}$, respectively, and $\Lambda = \{\lambda^i_j\}_{i,j=1,N}$ is the eigenvalue matrix of $\boldsymbol{J_g}$.
Evaluating the stretching rates along the eigendirections, $\boldsymbol{a}_j$, yields:

$$\omega_{\boldsymbol{a}_j} := \boldsymbol{a}_j \cdot \boldsymbol{J_g} \cdot \boldsymbol{a}_j. \tag{3.3.17}$$

By definition of eigendirection, it holds that $\boldsymbol{J_g} \cdot \boldsymbol{a}_j = \lambda_j \boldsymbol{a}_j$, so that $\omega_{\boldsymbol{a}_j}$ becomes

$$\omega_{\boldsymbol{a}_j} = \boldsymbol{a}_j \cdot \boldsymbol{J_g} \cdot \boldsymbol{a}_j = \boldsymbol{a}_j \cdot \lambda_j \boldsymbol{a}_j = |\boldsymbol{a}_j|^2 \lambda_j = \lambda_j. \tag{3.3.18}$$

since $|\boldsymbol{a}_j| = 1$ by construction. Thus, the stretching rate $\omega_{\boldsymbol{a}_j}$ evaluated along $\boldsymbol{a}_j$ coincides with the eigenvalue λ_j corresponding to that eigendirection.

The unit vector $\tilde{\boldsymbol{\tau}}$ can be rewritten after projecting the vector field over the right eigenvector basis as

$$\tilde{\boldsymbol{\tau}} = \frac{\boldsymbol{g}}{\mathrm{g}} = \frac{1}{\mathrm{g}} \sum_{i=1}^{N} \boldsymbol{a}_i f^i, \text{with } f^i := \boldsymbol{b}^i \cdot \boldsymbol{g}, \text{ and } \boldsymbol{g} = \sum_{i=1}^{N} \boldsymbol{a}_i f^i.$$

Given that $\boldsymbol{J_g} = \boldsymbol{A} \cdot \Lambda \cdot \boldsymbol{B}$, we now have

$$\begin{aligned} \omega_{\tilde{\boldsymbol{\tau}}} &= \tilde{\boldsymbol{\tau}} \cdot \boldsymbol{J_g} \cdot \tilde{\boldsymbol{\tau}} = \frac{1}{\mathrm{g}^2} \left(\boldsymbol{g} \cdot A \cdot \Lambda \cdot B \cdot \boldsymbol{g} \right) = \frac{\boldsymbol{g}}{\mathrm{g}^2} \sum_{i=1}^{N} \boldsymbol{a}_i \lambda_i \left(\boldsymbol{b}^i \cdot \boldsymbol{g} \right) \\ &= \frac{\boldsymbol{g}}{\mathrm{g}^2} \sum_{i=1}^{N} \boldsymbol{a}_i \lambda_i f^i = \frac{1}{\mathrm{g}^2} \sum_{i=1}^{N} \left(\boldsymbol{g} \cdot \boldsymbol{a}_i \right) \lambda_i f^i . \end{aligned} \tag{3.3.19}$$

Expanding $\boldsymbol{g}$ in terms of eigen-modes, one obtains

$$\boldsymbol{g} \cdot \boldsymbol{a}_i = \left(\sum_{k=1}^{N} \boldsymbol{a}_k f^k \right) \cdot \boldsymbol{a}_i = \sum_{k=1}^{N} f^k \left(\boldsymbol{a}_k \cdot \boldsymbol{a}_i \right), \tag{3.3.20}$$

where $\boldsymbol{a}_k \cdot \boldsymbol{a}_i$ is the direction cosine (the phase) between $\boldsymbol{a}_i$ and $\boldsymbol{a}_k$ (with $|\boldsymbol{a}_k \cdot \boldsymbol{a}_i| \leq 1$).

With this result, Eq. (3.3.19) becomes

$$\begin{aligned} \omega_{\tilde{\boldsymbol{\tau}}} &= \sum_{i=1}^{N} \left(\frac{1}{\mathrm{g}^2} \sum_{k=1}^{N} f^k \left(\boldsymbol{a}_k \cdot \boldsymbol{a}_i \right) \right) \lambda_i f^i \\ &= \sum_{i=1}^{N} \left(\frac{f^i}{\mathrm{g}^2} \sum_{k=1}^{N} f^k \left(\boldsymbol{a}_k \cdot \boldsymbol{a}_i \right) \right) \lambda_i = \sum_{i=1}^{N} W_i \lambda_i \end{aligned} \tag{3.3.21}$$

with

$$W_i := \frac{f^i}{\mathrm{g}} \frac{\boldsymbol{g} \cdot \boldsymbol{a}_i}{\mathrm{g}} = \frac{f^i}{\mathrm{g}} \sum_{k=1}^{N} \frac{f^k}{\mathrm{g}} \left(\boldsymbol{a}_k \cdot \boldsymbol{a}_i \right). \tag{3.3.22}$$

Therefore, the TSR may be computed as:

$$\omega_{\tilde{\boldsymbol{\tau}}} := \sum_{i=1}^{N} \bar{W}_i \ |\lambda_i| , \qquad \bar{W}_i = \frac{W_i}{\sum_{j=1}^{N} |W_j|} \tag{3.3.23}$$

with

$$W_i := \frac{f^i}{\mathrm{g}} \frac{\boldsymbol{g} \cdot \boldsymbol{a}_i}{\mathrm{g}}. \tag{3.3.24}$$

The vector field is an invariant direction for the (locally linearized) dynamics as well as the eigendirections. The unit vector $\tilde{\boldsymbol{\tau}}$ tangent to the vector field $\boldsymbol{g}$ changes according with the rate $\boldsymbol{\omega}_{\tilde{\boldsymbol{\tau}}} = \sum_{i=1}^{N} W_i \lambda_i$ because of the action of the (linearized) dynamics as represented by $\boldsymbol{J_g}$. By construction, this term takes the maximum value when all $\boldsymbol{a}_i$ are co-linear with

$\boldsymbol{g}$, that is:

$$\frac{\boldsymbol{g}\cdot\boldsymbol{a}_i}{\mathrm{g}} = \sum_{k=1}^{N} \frac{f^k}{\mathrm{g}} \left(\boldsymbol{a}_k \cdot \boldsymbol{a}_i\right) \leq \frac{f^i}{\mathrm{g}},$$

and substituting this result in Eqs. (3.3.20)-(3.3.22), provides the upper bound

$$\omega_{\tilde{\boldsymbol{\tau}}} \leq \sum_{i=1}^{N} \left(\frac{f^i}{\mathrm{g}}\right)^2 \lambda_i. \tag{3.3.25}$$

This shows that, because of the quadratic term, the sign of $\omega_{\tilde{\boldsymbol{\tau}}}$ depends on those of the prevailing eigenvalues.

To summarize, the stretching rate along an eigendirection simply coincides with the corresponding eigenvalue. Instead, the (tangential) stretching rate along the vector field, which is an invariant direction of the dynamics, is a weighted average of all eigenvalues λ_i, with weights W_i that according to Eq. (3.3.22) depend on:

- the normalized amplitude f^i of the i-th mode,
- the degree of co-linearity of the eigenvector $\boldsymbol{a}_i$ with respect to the vector field $\boldsymbol{g}$.

Based on the value and the sign of the TSR, one can readily characterize the explosive/dissipative nature of the chemical dynamics, identified by the positive/negative sign, and the estimate of the truly active chemical time scale, which is the inverse of the TSR.

Tangent Space Decomposition induced by TSR

After ordering the terms in the sum which defines $\omega_{\tilde{\boldsymbol{\tau}}}$ by the descending value of the modulus of the eigenvalue, and setting for simplicity $\boldsymbol{g}\cdot\boldsymbol{a}_i = f^i$ for all modes, we have

$$\omega_{\tilde{\boldsymbol{\tau}}} = \sum_{r=1}^{L} \left(\frac{f^r}{\mathrm{g}}\right)^2 \lambda_r + \sum_{a=L+1}^{K-1} \left(\frac{f^a}{\mathrm{g}}\right)^2 \lambda_a + \sum_{s=K}^{N} \left(\frac{f^s}{\mathrm{g}}\right)^2 \lambda_s, \tag{3.3.26}$$

where the labels "r", "a", "s" denote fast, active, slow modes, respectively. Let us now consider a typical situation for which, at some point in the phase space, there exists a number of fast and slow modes with a vanishing amplitude, that is $\{f^r = \boldsymbol{b}^r \cdot \boldsymbol{g} \approx 0\}_{r=1,\ldots,L}$ and $\{f^s = \boldsymbol{b}^s \cdot \boldsymbol{g} \approx 0\}_{s=K,\ldots,N}$, with $L < K$.

This situation can develop when there exist two spectral gaps between the slow and active subspaces, $\varepsilon_s = |\lambda_L/\lambda_{L+1}|$, and between the active and slow subspaces, $\varepsilon_r = |\lambda_{K-1}/\lambda_K|$, both (much) smaller than one.

In such a case, it happens that

$$\omega_{\tilde{\boldsymbol{\tau}}} \approx \sum_{a=L+1}^{K-1} \left(\frac{f^a}{\mathrm{g}}\right)^2 \lambda_a, \tag{3.3.27}$$

which implies that only the active scales contribute to $\omega_{\tilde{\boldsymbol{\tau}}}$. If an eigenvalue is positive, say λ_{a+}, it is likely that f^{a+} will be the largest of all active mode amplitudes. In this case $\omega_{\tilde{\boldsymbol{\tau}}}$ will be mostly affected by λ_{a+}.

From Eq. (3.3.26), three scales can be identified: *(i)* one associated with $\omega_{\tilde{\boldsymbol{\tau}}}$, which is the most energy containing scale; *(ii)* two others associated with λ_{K-1} and λ_{L+1}, which are the fastest and slowest scales, respectively, contributing to $\omega_{\tilde{\boldsymbol{\tau}}}$, and these bracket the range of active (energy containing) scales. The integers K and L underline a decomposition of the tangent space $\mathcal{T}_{\boldsymbol{y}}$ in three subspaces: the fast subspace $\mathcal{F}_{TSR}$ $(r = 1, \ldots, L)$, the active $\mathcal{A}_{TSR}$ $(a = L+1, \ldots, K-1)$, and the slow $\mathcal{S}_{TSR}$ $(s = K, \ldots, N)$, such that $\mathcal{T}_{\boldsymbol{y}} = \mathcal{F}_{TSR} \bigoplus \mathcal{A}_{TSR} \bigoplus \mathcal{S}_{TSR}$. This three-fold decomposition is analogous to that employed in the G-Scheme framework proposed in [40]. In the CSP method, the contribution of the M fastest modes $(r = 1, \ldots, M)$ to the system dynamics is considered negligible until the inequality (2.2.9) is satisfied:

$$\delta y^i_{fast} \approx |\tau^{M+1}_{chem} \sum_{r=1}^{M} a^i_r f^r_0 \frac{1 - e^{\lambda^r \tau^{M+1}_{chem}}}{\lambda^r}| < y^i_{error} = \varepsilon^i_{rel} y^i + \varepsilon^i_{abs}. \tag{3.3.28}$$

where $\tau^{M+1}_{chem} = 1/|\lambda_{M+1}|$, and $\boldsymbol{\epsilon} = \{\epsilon^j\}_{j=1,N}$ is a user-defined error vector. In CSP, the first integer M for which the inequality is not satisfied for all N components of the state $\boldsymbol{y}$, identifies the decomposition of the tangent space as $\mathcal{T}_{\boldsymbol{y}} = \mathcal{F}_{CSP} \bigoplus \mathcal{S}_{CSP}$, with $\mathcal{F}_{CSP} = \{\boldsymbol{a}_r\}_{r=1,\ldots,M}$ and $\mathcal{S}_{CSP} = \{\boldsymbol{a}_s\}_{s=M+1,\ldots,N}$.

Note that the "slow" modes in the CSP nomenclature correspond to the union of the "slow" and "active" modes in the above nomenclature, that is $\mathcal{A}_{TSR} \bigoplus \mathcal{S}_{TSR} = \mathcal{S}_{CSP}$, while the fast subspaces coincide: $\mathcal{F}_{TSR} = \mathcal{F}_{CSP}$.

3.3.2 Participation Index of a reaction to the TSR

The additive nature of definition (3.3.23) suggests the introduction of a Participation Index of the i-th mode to the TSR as:

$$P^{\omega_{\tilde{\boldsymbol{\tau}}}}_{\text{mode}_i} = \frac{\bar{W}_i \ |\lambda_i|}{\sum\limits_{j'=1}^{N} \left|\bar{W}_{j'} \ |\lambda_{j'}|\right|} \qquad \text{no sum on } i. \tag{3.3.29}$$

Modes with a large and positive/negative $P^{\omega_{\tilde{\boldsymbol{\tau}}}}_{\text{mode}_i}$ are the ones that contribute the most to the growth/decay of the most energy containing time scale. Next, the reactions that contribute the most to the development of the $\omega_{\tilde{\boldsymbol{\tau}}}$ scale can be identified by resorting to the CSP participation index for the k-th reaction to these modes, $P^{\text{mode}_i}_{\text{reaction}_k}$, defined in § 3.1. To identify the reactions most contributing to the development of $\omega_{\tilde{\boldsymbol{\tau}}}$, an index is conveniently introduced relating the k–th reaction to $\omega_{\tilde{\boldsymbol{\tau}}}$, $P^{\bar{\omega}_{\tilde{\boldsymbol{\tau}}}}_{\text{reaction}_k}$, as the product of the participation index of the mode i to the TSR, $P^{\omega_{\tilde{\boldsymbol{\tau}}}}_{\text{mode}_i}$, times the CSP participation index of the k–th reaction to the i–th mode, $P^{\text{mode}_i}_{\text{reaction}_k}$, that is

$$P^{\omega_{\tilde{\boldsymbol{\tau}}}}_{\text{reaction}_k} := \sum_{\text{mode}_i=1}^{N} P^{\omega_{\tilde{\boldsymbol{\tau}}}}_{\text{mode}_i} \, P^{\text{mode}_i}_{\text{reaction}_k}. \tag{3.3.30}$$

Since the CSP participation indices to each mode $P^{\text{mode}_i}_{\text{reaction}_k}$ and the indices $P^{\omega_{\tilde{\boldsymbol{\tau}}}}_{\text{mode}_i}$ sum to 1 by construction, it follows that $\sum_{k=1}^{R} P^{\omega_{\tilde{\boldsymbol{\tau}}}}_{\text{reaction}_k} = 1$ as well, in virtue of the following:

$$\sum_{k=1}^{R} P^{\omega_{\tilde{\boldsymbol{\tau}}}}_{\text{reaction}_k} = \sum_{k=1}^{R} \left(\sum_{i=1}^{N} P^{\omega_{\tilde{\boldsymbol{\tau}}}}_{\text{mode}_i} P^{\text{mode}_i}_{\text{reaction}_k} \right) = \left(\sum_{i=1}^{N} P^{\omega_{\tilde{\boldsymbol{\tau}}}}_{\text{mode}_i} \right) \left(\sum_{k=1}^{R} P^{\text{mode}_i}_{\text{reaction}_k} \right) = 1. \tag{3.3.31}$$

Note there exist other metrics that allow to identify the reactions most contributing to a given time scale. The important question then becomes how to sort out the most relevant time scales: in fact, it might happen that no or little energy is associated to a specific time scale. In other words, although there might exist a *potential* channel to propagate energy through a mode (at the associated time scale), it might well happen that the system does not select that mode for the *actual* energy propagation. On this regard, it is stressed that - by construction - the indices $P^{\omega_{\tilde{\boldsymbol{\tau}}}}_{\text{reaction}_k}$ select the chemical processes that are associated with (i) the time scale provided by $\omega_{\tilde{\boldsymbol{\tau}}}$, and (ii) all and only the (active) modes that contribute

the most to the "energy" of the system during both the explosive and contractive phases of its dynamics. This way, the user is not requested to make any a-priori assumption about the specific system of interest.

3.4 Extension of TSR to non-homogeneous problems

The CSP method has been extended to systems of PDEs in § 2.3. It is rather natural to extend the definition of the TSR to systems of PDEs by simply replacing the definition of $\tilde{\boldsymbol{\tau}}$ in (3.3.15), which is based on kinetics only, with a $\tilde{\boldsymbol{\tau}}_{pde}$ based on the algebraic sum of kinetics and transport as follows:

$$\tilde{\boldsymbol{\tau}}_{pde} =: \frac{\boldsymbol{L}_x(\boldsymbol{y}) + \boldsymbol{g}(\boldsymbol{y})}{|\boldsymbol{L}_x(\boldsymbol{y}) + \boldsymbol{g}(\boldsymbol{y})|} \tag{3.4.1}$$

which can be rewritten after projecting the vector field over the right (kinetic) eigenvector basis as

$$\tilde{\boldsymbol{\tau}}_{pde} = \frac{1}{|\boldsymbol{L}_x(\boldsymbol{y}) + \boldsymbol{g}(\boldsymbol{y})|} \sum_{i=1}^{N} \boldsymbol{a}_i h^i, \tag{3.4.2}$$

with

$$h^i := \boldsymbol{b}^i \cdot (\boldsymbol{L}_x(\boldsymbol{y}) + \boldsymbol{g}(\boldsymbol{y})).$$

After having introduced $\tilde{\boldsymbol{\tau}}_{pde}$, it is immediate to arrive at the extended definition of the TSR, $\omega_{\tilde{\boldsymbol{\tau}}_{pde}}$, which reads:

$$\omega_{\tilde{\boldsymbol{\tau}}_{pde}} := \tilde{\boldsymbol{\tau}}_{pde} \cdot \boldsymbol{J}_{\boldsymbol{g}} \cdot \tilde{\boldsymbol{\tau}}_{pde} = \sum_{i=1}^{N} W_{i,pde} \lambda_i, \tag{3.4.3}$$

where the weights $W_{i,pde}$ are defined as follows

$$W_{i,pde} := \frac{h^i}{\mathrm{L} + \mathrm{g}} \left(\tilde{\boldsymbol{\tau}}_{pde} \cdot \boldsymbol{a}_i \right) = \frac{h^i}{\mathrm{L} + \mathrm{g}} \sum_{k=1}^{N} \frac{h^k}{\mathrm{L} + \mathrm{g}} \left(\boldsymbol{a}_k \cdot \boldsymbol{a}_i \right), \tag{3.4.4}$$

where L is the norm of $\boldsymbol{L}$.

The explosive/dissipative nature of the flow will still be identified by a positive/negative value of the TSR, $\omega_{\tilde{\boldsymbol{\tau}}_{pde}}$. Also, it can happen that a purely kinetic propensity to explosion, as marked by a large and positive value of $\omega_{\tilde{\boldsymbol{\tau}}}$, can be mitigated by an adverse effect of transport, that is with a lower - albeit still positive - value of $\omega_{\tilde{\boldsymbol{\tau}}_{pde}}$. In the limit, $\omega_{\tilde{\boldsymbol{\tau}}_{pde}}$ can

become zero or negative when transport overwhelms kinetics. This is the case when ignition cannot occur at low Damkhöler numbers. Note that, when transport is absent($\boldsymbol{L}_x = 0$), the purely reactive case is recovered.

In the following, the purely reactive TSR will be referred to as $\omega_{\tilde{\boldsymbol{\tau}}}$, or equivalently as $\omega_{\boldsymbol{g}} := \omega_{\tilde{\boldsymbol{\tau}}}(\boldsymbol{L}_x = 0, \boldsymbol{g})$, and the reactive-transport TSR as $\omega_{\tilde{\boldsymbol{\tau}}_{pde}}$, or equivalently $\omega_{\boldsymbol{g}+\boldsymbol{L}} := \omega_{\tilde{\boldsymbol{\tau}}}(\boldsymbol{L}_x \neq 0, \boldsymbol{g})$. When transport is absent, $\omega_{\boldsymbol{g}}$ provides the stretching rate along the unit vector oriented in the direction of the chemical source term. While in a purely reactive system, only $\omega_{\boldsymbol{g}}$ is defined, in a reactive-transport system both quantities are defined and meaningful, $\omega_{\boldsymbol{g}+\boldsymbol{L}}$ being the stretching along the reactive-transport vector field and $\omega_{\boldsymbol{g}}$ the stretching along the chemical source term direction, i.e., the direction the system would follow if transport were abruptly removed.

On the basis of the TSR indices, diagnostics criteria are proposed which are able to identify in non homogeneous systems the most ignitable conditions and to discriminate between spontaneous ignition and deflagration front, as detailed in the following:

Def.1: At any given time, the locus of extrema of the $\omega_{\boldsymbol{g}+\boldsymbol{L}}$ field ($\partial[\omega_{\boldsymbol{g}+\boldsymbol{L}}]/\partial\xi = 0$) identifies the "most ignitable states" if $\omega_{\boldsymbol{g}+\boldsymbol{L}} > 0$ and the "most dissipative state" if $\omega_{\boldsymbol{g}+\boldsymbol{L}} < 0$.

Def.2: The locus where the quantity $\delta(\omega) := \text{sign}[\omega_{\boldsymbol{g}+\boldsymbol{L}}]|\omega_{\boldsymbol{g}+\boldsymbol{L}} - \omega_{\boldsymbol{g}}|$ is large and positive identifies regions where transport plays a significant role in the explosive regime (*e.g.* a deflagration front).

Def.3: The locus where $|\delta(\omega)|$ is small identifies regions where kinetics is the controlling process (spontaneous ignition).

3.4.1 Participation Index of a Process to the extended TSR

In analogy with what has been done in § 3.3.2, a Participation Index of a process to the extended TSR can be introduced. In this case, the process is either a reaction or the convection/diffusion of a species.

Recalling the definition (2.3.3) for the CSP mode amplitudes h^i in non-homogeneous problems:

$$h^i = \boldsymbol{b}^i \cdot (\boldsymbol{L}_x(\boldsymbol{y}) + \boldsymbol{g}(\boldsymbol{y})), \tag{3.4.5}$$

the extension of the CSP Participation Index, defined in § 3.1, to non-homogeneous problems, which quantifies the influence of a generic k-th process, either a reaction or a convection/diffusion of a species, to the i-th mode, may be defined as:

$$P_k^i = \frac{|(\boldsymbol{b}^i \cdot \boldsymbol{S}_k) r^k|}{\sum_{j'=1}^{N} |(\boldsymbol{b}^i \cdot \boldsymbol{e}_{j'}) \boldsymbol{L}_x^{j'}| + \sum_{k'=1}^{R} |(\boldsymbol{b}^i \cdot \boldsymbol{S}_{k'}) r^{k'}|}, \qquad k = 1, ..., R \ , \tag{3.4.6}$$

$$P_j^i = \frac{|(\boldsymbol{b}^i \cdot \boldsymbol{e}_j) \boldsymbol{L}_x^j|}{\sum_{j'=1}^{N} |(\boldsymbol{b}^i \cdot \boldsymbol{e}_{j'}) \boldsymbol{L}_x^{j'}| + \sum_{k'=1}^{R} |(\boldsymbol{b}^i \cdot \boldsymbol{S}_{k'}) r^{k'}|} \qquad j = 1, ..., N \ , \tag{3.4.7}$$

where $\boldsymbol{e}_j$ is the j-th versor in the phase space.

The definition (3.4.6) yields R indexes referring to unidirectional reactions and definition (3.4.7) yields N indexes referring to each spatial operator $\boldsymbol{L}_x$, *i.e.* N for the species diffusion and N for the species convection, if both are present.

The combination of this index with the participation index of a mode to the extended TSR, which may be defined in analogy with definition (3.3.29) as:

$$P_{\mathrm{mode}_i}^{\omega_{\tilde{\tau}_{pde}}} = \frac{\bar{W}_{i,pde} \ |\lambda_{i,pde}|}{\sum\limits_{j'=1}^{N} \left| \bar{W}_{j',pde} \ |\lambda_{j',pde}| \right|} \qquad \text{no sum on } i. \tag{3.4.8}$$

quantifies the contribution of a physical process, either a reaction or a transport process, to the extended TSR, that is:

$$P_{\mathrm{process}_k}^{\omega_{\tilde{\tau}}} := \sum_{\mathrm{mode}_i=1}^{N+1} P_{\mathrm{mode}_i}^{\omega_{\tilde{\tau}}} \ P_{\mathrm{process}_k}^{\mathrm{mode}_i}. \tag{3.4.9}$$

3.5 Analysis of a homogeneous problem

The capabilities of the Tangential Stretching Rate and the related TSR Participation Indices are demonstrated in the analysis of a simple homogeneous problem, involving a hydrogen/air mixture. In particular, two test-cases are investigated: a low-temperature and a high-temperature oxidation. The detailed chemistry is supplied by a 12-species, 33-reactions, kinetic scheme designed for hydrogen and carbon monoxide oxidations [41]. The different initial conditions activate two distinct oxidation paths, known in literature as

below- and above-crossover regimes [42, 43, 44]. In both cases, the slow initiation reaction, which generates the first radicals, is[1]:

$$H_2 + O_2 \longrightarrow HO_2 + H \qquad \text{(Rb 10)}$$

However, based on the mixture initial temperature, the ignition process is characterized by a competition between the chain branching reaction:

$$H + O_2 \longrightarrow O + OH \qquad \text{(Rf 1)}$$

and the chain terminating three-body collision:

$$H + O_2 + M \longrightarrow HO_2 + M \qquad \text{(Rf 9)}$$

which produces a rather inactive radical (HO_2) instead of two active radicals (O and OH). Above the *crossover temperature*, which is pressure-dependent (∼950 K at 1 atm for stoichiometric mixtures), the chain branching reaction dominates. However, below the crossover temperature, the two reactions compete and the chain branching process is inhibited. In this low-temperature regime, another oxidation process takes place, namely a thermal runaway caused by the very slow, slightly exothermic reactions:

$$H_2 + HO_2 \longrightarrow H_2O_2 + H \qquad \text{(Rb 18)}$$
$$2\ HO_2 \longrightarrow H_2O_2 + O_2 \qquad \text{(Rf 15)}$$

which generate H_2O_2 and in turn activate the alternative chain branching path:

$$H_2O_2 + M \longrightarrow 2\ OH + M \qquad \text{(Rf 16)}.$$

The two analyzed test cases are isobaric (1 atm), stoichiometric H_2/air mixtures at the initial temperatures of 750 K and 1200 K. The dataset are generated with the CSPTk package [35], which integrates in time the batch reactor model of Eq. (A.1.1) using CVODE [36] and where the thermo–kinetic database is parsed and handled using the TChem package [37]. Table 3.3 summarizes all the reactions that are referred to in this section.

[1] the reactions numbering follows the kinetic mechanism ordering and is summarized in table 3.3

Table 3.3: Chemical reactions legend, where f stands for *forward* and b for *backward*.

Rf - 1:	$H + O_2 \longrightarrow O + OH$
Rf - 2:	$O + H_2 \longrightarrow H + OH$
Rf - 3:	$H_2 + OH \longrightarrow H_2O + H$
Rf - 8:	$H + OH + M \longrightarrow H_2O + M$
Rb - 8:	$H_2O + M \longrightarrow H + OH + M$
Rf - 9:	$H + O_2 + M \longrightarrow HO_2 + M$
Rb - 10:	$H_2 + O_2 \longrightarrow HO_2 + H$
Rf - 15:	$2\,HO_2 \longrightarrow H_2O_2 + O_2$
Rf - 16:	$H_2O_2 + M \longrightarrow 2\,OH + M$
Rb - 18:	$H_2 + HO_2 \longrightarrow H_2O_2 + H$

3.5.1 Above crossover auto-ignition

Figure 4 shows the systems' eigenvalues evolution against integration time-step (left) and time (right) for the T_0=1200 K case. The eigenvalues are plotted in Λ formulation, following the definition employed in § 3.1.1, Def. (3.1.3). Typical features of the eigenvalues can be observed: (i) a couple of positive eigenvalues, whose merging happens approximately in correspondence of the maximum temperature rate of increase, *i.e.* the ignition delay time, which is $\tau_{ign} \approx 4.5 \times 10^{-5}$; (ii) a number of dormant modes, associated to negligibly small eigenvalues (collapsed onto the zero axis in the plots), corresponding to the 4 atomic conservation laws (H,O,C,N). The TSR, in the same logarithmic formulation employed for the eigenvalues, is plotted as a red symbol on top of the eigenvalues. When plotting figures involving the TSR, the variables $\Omega := \mathrm{Sign}(\omega_{\tilde{\boldsymbol{\tau}}}) * \mathrm{Log}_{10}|\omega_{\tilde{\boldsymbol{\tau}}}|$ and $\Omega_{pde} := \mathrm{Sign}(\omega_{\tilde{\boldsymbol{\tau}}_{pde}}) * \mathrm{Log}_{10}|\omega_{\tilde{\boldsymbol{\tau}}_{pde}}|$ are adopted to appreciate the order of magnitude of both the positive and negative TSR in the same figure. With the exception of the very first time-steps, the TSR tracks the positive eigenvalue, denoting the explosive propensity of the system, whose characteristic time scale is $O(10^{-6})$ s. After the merging, the TSR tracks the eigenvalues associated to mode #7 first, and mode #8 then, following it until equilibrium. This means that the system evolves and approaches equilibrium according to the dissipative

scale equal to $1/\lambda_8$. Mode #8 is also the first (faster) slow mode (M=7) from time-step #600 to equilibrium.

The extremely short ignition delay time and the explosive nature of the system since the very beginning are clues of the above-crossover regime of this test-case. However, more insights on the physics of the problem may be obtained by resorting to the TSR participation indices, defined in § 3.3.2, which identify the processes involved in the energy carrying, TSR-important, modes, *i.e.* the dominant reactions. Figure 5 shows the TSR participation indices against time. As expected, in the very first stages Rb-10 is the dominant reaction, being the initiation step. Immediately after, the chain branching reaction Rf-1 takes the lead ($\sim$ 70 %), while the chain terminating reaction Rf-9 has a negligible participation index (not shown). This behavior is typical of the above-crossover regime. To a minor extent, chain branching reaction Rf-2 ($O + H_2 \longrightarrow H + OH$) and, very close to ignition, chain carrying reaction Rf-3 ($H_2 + OH \longrightarrow H_2O + H$) share the remaining $\sim$ 30 % of importance. These three reactions are known as *shuffle* reactions, and constitute the submechanism that describes the rapid H-O-OH radical conversion in the radical pool.

After ignition, the recombination reaction Rf-8 ($H + OH + M \longrightarrow H_2O + M$) becomes the leading process, which becomes counter-balanced by its reverse reaction (Rb-8) when approaching equilibrium.

3.5.2 Below crossover auto-ignition

Figure 6 shows the systems' eigenvalues evolution against integration time-step (left) and time (right) for the T_0=750 K case. Differently to the previous case, the positive eigenvalue becomes large with a long delay, and the ignition delay itself is extremely large ($\tau_{ign} \approx 73.6$ s). However, the post-ignition behavior of the eigenvalues resembles the previous case one. Again, TSR tracks the positive eigenvalue until merging, then follows λ_8. More insights may be obtained from Fig.7, that shows the time evolution of the TSR participation indices, plotted with 3 different degrees of magnification, so as to appreciate their evolution far and close to ignition. As expected, the initiation reaction Rb-10 is again the leading process in the first instants. Then, reaction Rb-18 takes the lead, followed by Rf-16 and Rf-15, perfectly resembling the alternative ignition path, typical of the below-crossover regime.

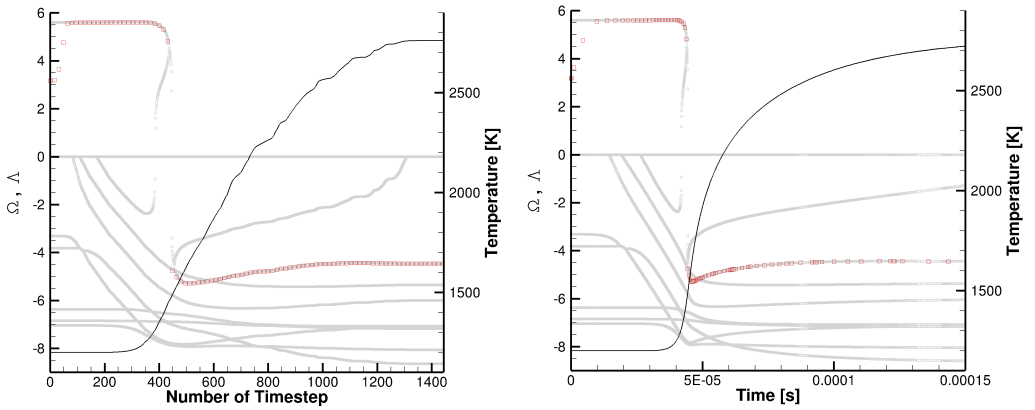

Figure 4: Eigenvalues (grey, in Λ formulation), TSR (red, in Ω formulation) and temperature evolution against number of integration timestep (a) and time (b). Above crossover regime.

Noteworthy, Rf-1 and Rf-9 have similar importance indices, since they compete, preventing the chain branching process typical of high-temperature mixtures. Then, after a long time delay, Rf-1 eventually becomes the most important process, in correspondence of the maximum temperature increase and positive eigenvalues merging. Figure 8 shows the same indices plotted against the number of integration time-step, to allow a comparison with the eigenvalues/TSR evolution of Fig.6 (left). Interestingly, the positive eigenvalue starts increasing around time-step #1000, which corresponds to the couple Rf-1/Rf-9 overtaking Rf-16 as the most important reactions. Interestingly, the sharpest positive eigenvalue growth happens between time-steps #1300 and #1500, where the chain terminating reaction Rf-9 is the leading process, with Rf-1 slightly less important. However, the maximum temperature rate and the eigenvalues merging correspond to Rf-1 being the reaction with the largest participation index.

In conclusion, the TSR analysis allowed to reveal the active chemical time scales and the reactions participating to the active modes. The latter are in complete agreement with the physical expectations in both cases, *i.e.* above and below crossover, where substantially different chemical pathways are taken. In addition, the TSR participation indices may be

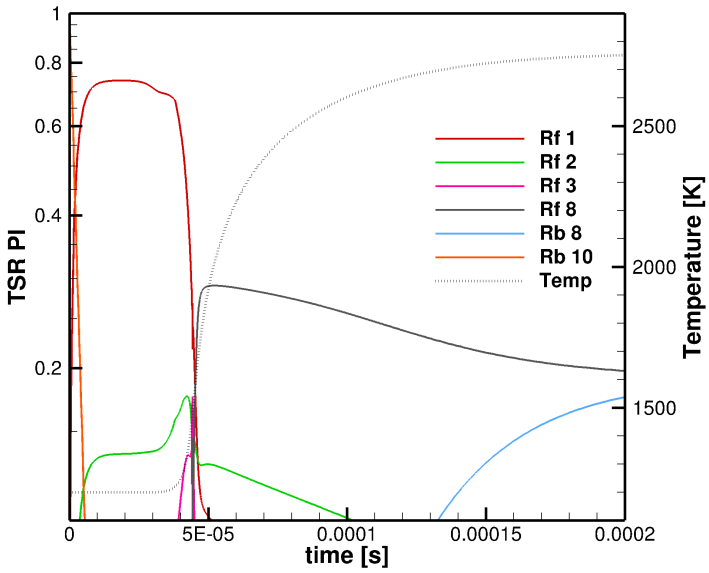

Figure 5: TSR Participation Indices against time. Above crossover regime.

even used to identify the regimes. For example, by inspecting the relative participation of reactions Rf-1 and Rf-9, one can infer whether the mixture experienced an above- or below-crossover ignition, and which is the crossover temperature, which is a function of pressure. Figure 9 (left) shows the difference between $P^{\omega_{\bar{\tau}}}_{\text{Rf-1}}$ and $P^{\omega_{\bar{\tau}}}_{\text{Rf-9}}$, averaged over the branching region of the auto-ignition, computed for a set of stoichiometric batch reactor solutions obtained at different initial temperature and pressure. For a fixed pressure, it can be observed that the two indices are equal, *i.e.* their difference is zero, up to a certain initial temperature, where they start to differ in favor of a larger $P^{\omega_{\bar{\tau}}}_{\text{Rf-1}}$. When the two are equal, the regime may be labeled as below-crossover, while $P^{\omega_{\bar{\tau}}}_{\text{Rf-1}}$ larger than $P^{\omega_{\bar{\tau}}}_{\text{Rf-9}}$ is a typical behavior encountered in above-crossover regimes. The temperature at which the regime changes may be denoted as crossover temperature. Note that, increasing pressure, the initial temperature where reaction Rf-1 starts to participate more than Rf-9, *i.e.* the crossover temperature, shifts towards higher temperatures. This behavior is clearly visible

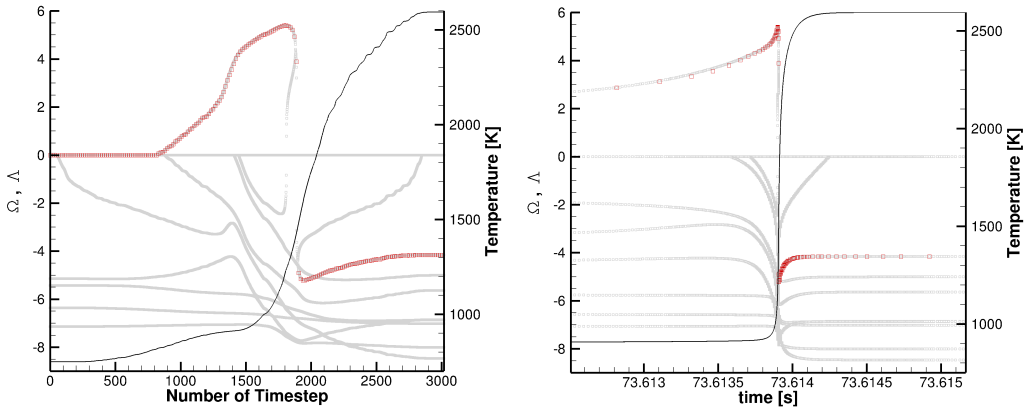

Figure 6: Eigenvalues (grey, in Λ formulation), TSR (red, in Ω formulation) and temperature evolution against number of integration timestep (a) and time (b). Below crossover regime.

in Fig.9 (right), which resembles the analytic expression for the crossover temperature defined in [45].

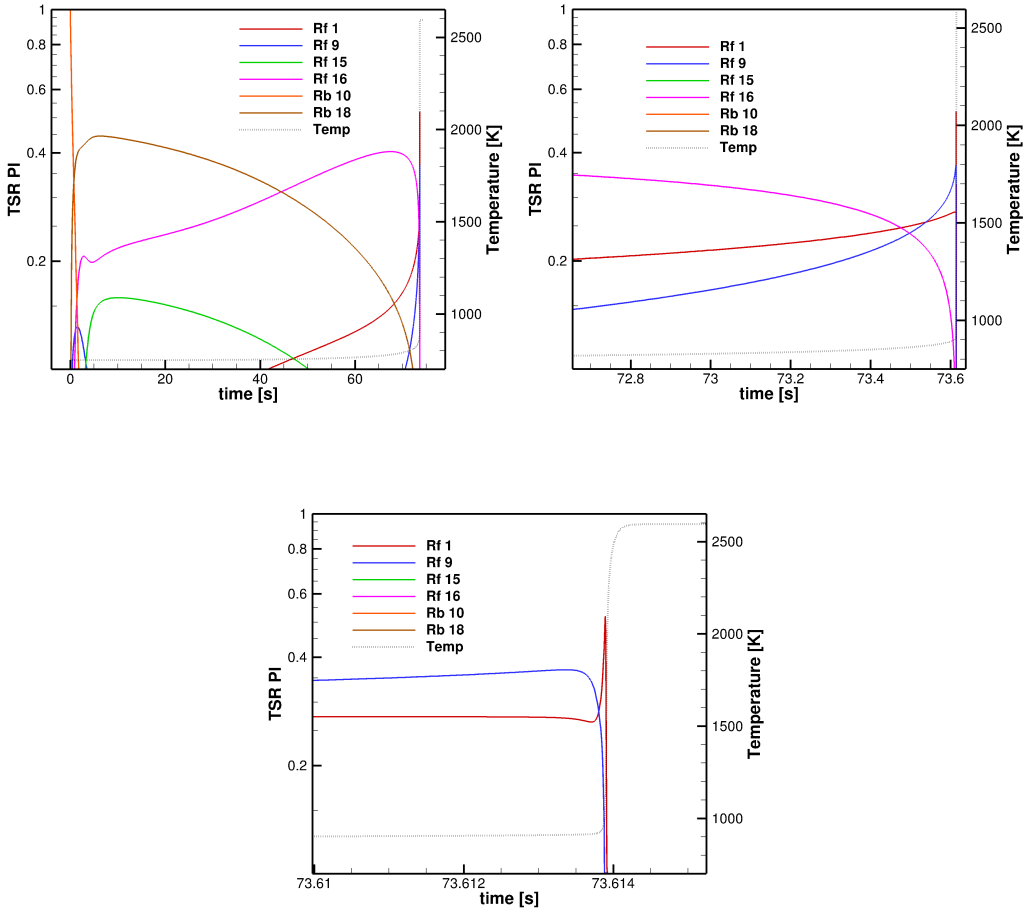

Figure 7: TSR Participation Indices against time, with different degrees of magnification. Below crossover regime.

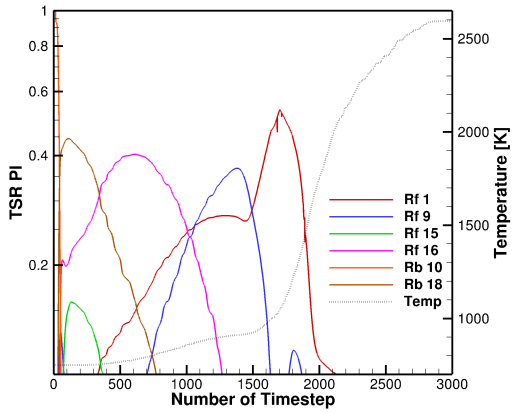

Figure 8: TSR Participation Indices against number of time-step. Below crossover regime.

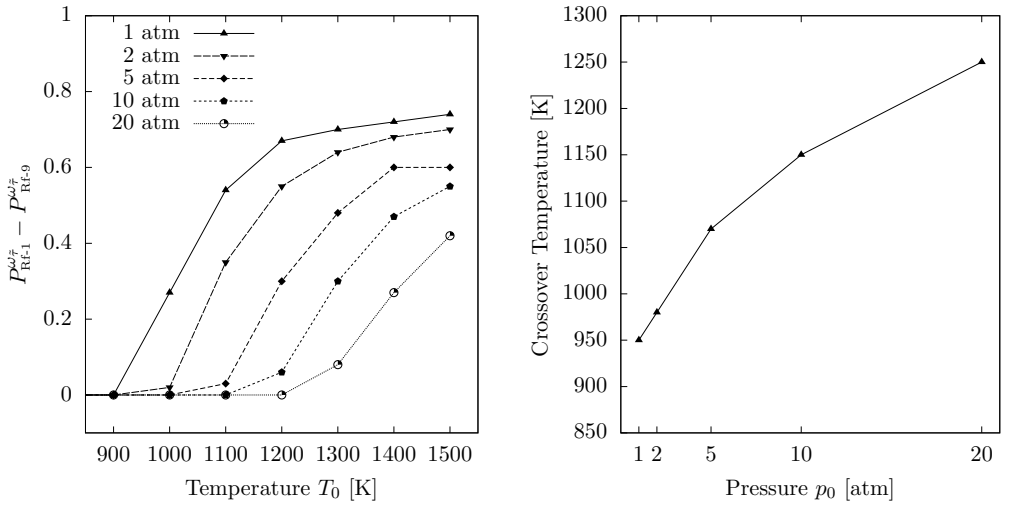

Figure 9: Difference between $P^{\omega_{\tilde{\tau}}}_{\text{Rf-1}}$ and $P^{\omega_{\tilde{\tau}}}_{\text{Rf-9}}$ with increasing initial temperature T_0, for different pressure values p_0 (left); estimated crossover temperature (right)

3.6 Analysis of a non-premixed flame

An unsteady laminar flamelet model, representing the competition between chemical kinetics and molecular diffusion processes, is used to generate numerical datasets describing ignition processes in a non premixed system. These datasets will be analyzed by resorting to the Tangential Stretching Rate.

The laminar flamelet model is thoroughly described in Appendix A. The model equations are complemented by proper initial and boundary conditions. Time accurate solutions of Eq.(A.2.1) are obtained by means of the CSPTk package [35], which integrates in time Eq. (A.2.1) using CVODE [36] and where the thermo–kinetic database is parsed and handled using the TChem package [37]. The scalar dissipation rate χ is an input parameter of the flamelet system, which affects the flame structure in terms of ignition delay, as well as flame quenching. Since the scalar dissipation represents the reciprocal of a diffusive time scale, a Damkhöler number can be defined as $Da = 1/(\tau_c \chi)$, where τ_c is a characteristic chemical time scale. As will be emphasized later, a good choice for the characteristic chemical time scale is the reciprocal of the TSR. The S-shaped diagram in Fig. 10 provides a good appreciation of the flame structure sensitivity to the Damkhöler number, and therefore to the scalar dissipation χ. A point on the upper branch of the S-shaped diagram in Fig. 10 refers to a burning (stationary) flame (point A). The peak value of flame temperature decreases when the scalar dissipation increases (Da decreases). Quenching occurs suddenly for scalar dissipation values higher than a critical value, Da_E, (point E). The points on the lower branch of the diagram refer to mixtures whose temperatures is close to the autoignition one, nevertheless autoignition is hindered by the diffusive processes (point B). A progressive reduction of the scalar dissipation rate, below a value Da_I, eventually allows the system to autoignite (points I). Both points E and B (representing quenching/extinction) and points I and A (representing autoignition) are end-points of unsteady transition of the system. The main goal of this section is to analyze the autoignition transient of the laminar diffusive flame using the Tangential Stretching Rate index as the principal tool of analysis. Quenching is left to future work.

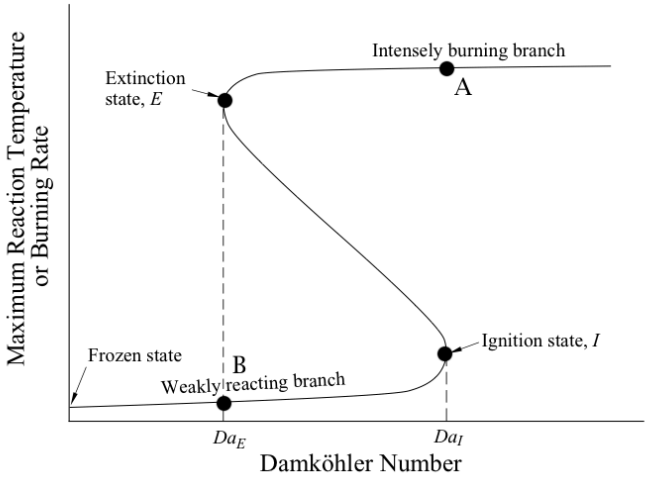

Figure 10: S-shaped temperature behavior as a function of the Damkohler number, $Da = 1/(\tau_c \chi)$.

3.6.1 Results of Unsteady Flamelets

The reactive mixture considered in this work is syngas/air. The same detailed chemical scheme of § 3.5, with 12 species and 33 chemical reactions is employed [41].

The fuel is made of syngas (H_2:CO molar ratio of 0.7:1), the oxidizer is oxygen diluted with three times the amount of nitrogen present in the air (i.e. a molar ratio of N_2:O_2=11.28). This reactive mixture is relevant to gas turbine operations and has been extensively studied in [46].

The domain of integration relates to mixture fraction, and it ranges from $\xi = 0$ to $\xi = 1$. The mixture fraction space discretization involves 1024 cells of equal size. The boundary conditions here considered are pure oxidizer at $\xi = 0$ and pure fuel at $\xi = 1$, both kept at the temperature of 1000 K, while the pressure is kept constant in the whole domain and at all times and equal to 20 atm. The initial condition at time t=0 is a constant temperature of 1000K in the whole ξ domain, and the mass fractions of fuel and oxidizer along ξ are prescribed as linear distributions between the left and right boundaries.

Two different test cases will be analyzed and compared: in the first one, the scalar

dissipation rate χ in Eq. (A.2.1) is set to zero, i.e. $\chi = 0\ s^{-1}$, to isolate the role of kinetics at different mixture fraction values; in the second one it is set to $\chi = 10\ s^{-1}$, to study the combined diffusion/reaction system. Such a value of the scalar dissipation rate is chosen for showing that even a small degree of mixing radically changes the behavior of the system with respect to the purely kinetic-driven dynamics. Other numerical simulations performed at larger values of χ, up to the quenching value of $\chi_{quench} \approx 650\ s^{-1}$, are not qualitatively different from the one presented in the following for what concerns the TSR analysis, thus are not included in this work.

3.6.2 Pure kinetics

First, the time evolution of the system described by Eq. (A.2.1) when $\chi = 0\ s^{-1}$ is discussed. When there is no diffusion that couples with kinetics at different mixture fractions, each batch of mixture along the ξ-axis behaves as an independent reactor undergoing auto-ignition at constant pressure, with an ignition delay time that varies from point to point because of the different composition. The ignition delay time features a minimum at about $\xi \approx 0.5$, and increases significantly on the lean side and to a small extent on the rich side. At large times, temperature reaches its peak value at the stoichiometric mixture fraction ($\xi_{st} = 0.055$), as shown in Fig. 11. The equilibrium temperature decreases for leaner and richer mixtures.

Figure 12 shows that TSR, computed in the direction of $\boldsymbol{g}$, since $\boldsymbol{L}_x$ is absent, takes positive values ahead of the ignition front ($\Omega > 0$). It is worth stressing that this occurs in a region of low temperature. Indeed, a positive TSR identifies the explosive region of the system: as such, it provides a measure of the "propensity" to ignition of the system. The most ignitable conditions are actually identified with the peak value of TSR noticeable at $\xi \approx 0.5$. Downstream the ignition front, TSR becomes negative, this indicating the dissipative nature of the approach to equilibrium of the system. Note that the region to the left of the peak TSR ($\xi \approx 0.5$) exhibits a high propensity to ignition whereas at very rich conditions the mixture is unable to ignite ($\Omega < 0$).

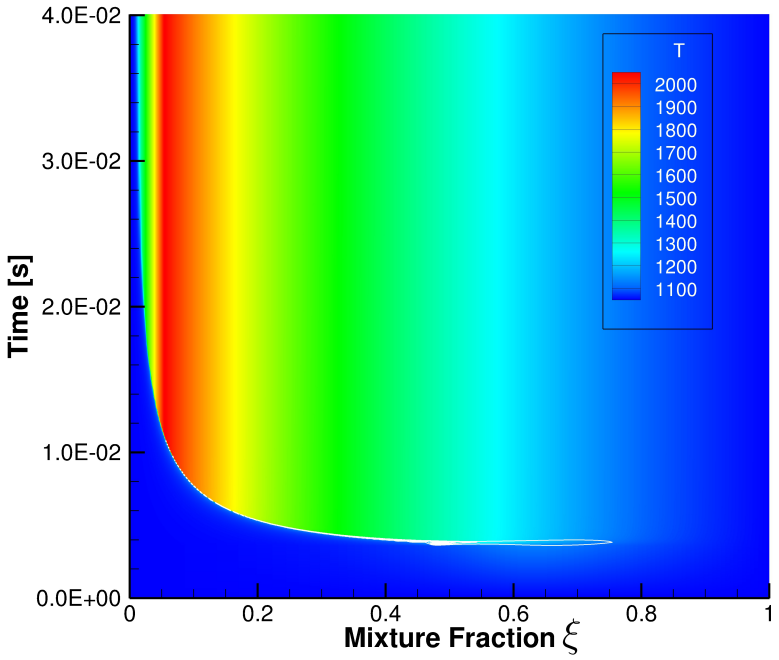

Figure 11: Case $\chi = 0\ s^{-1}$. Contour levels of Temperature.

3.6.3 Combined effect of diffusion and kinetics

The second case involving diffusion is now discussed, and specifically the case obtained setting $\chi = 10\ s^{-1}$. While the case $\chi = 0\ s^{-1}$ provides a simple model of a (seemingly) front propagation purely driven by spontaneous ignition, the case $\chi = 10\ s^{-1}$ models a deflagration wave involving diffusion as transport mechanism (no convection).

Figure 13 shows the isocontour lines of temperature, T, and HCO mass fraction in the (ξ, t) phase space, while Fig. 14 shows several temporal snapshots of the temperature field. Ignition begins - as observed for the purely kinetic case - at $\xi \approx 0.5$ as indicated by the location of the extended TSR peak value in Fig. 16, while the equilibrium field (red line in Fig. 14) peaks at $\xi \approx 0.055$.

Diffusion steps in as soon as kinetics creates spatial non uniformities, in such a way to propagate heat and mass outward with respect to the most ignitable mixture fraction

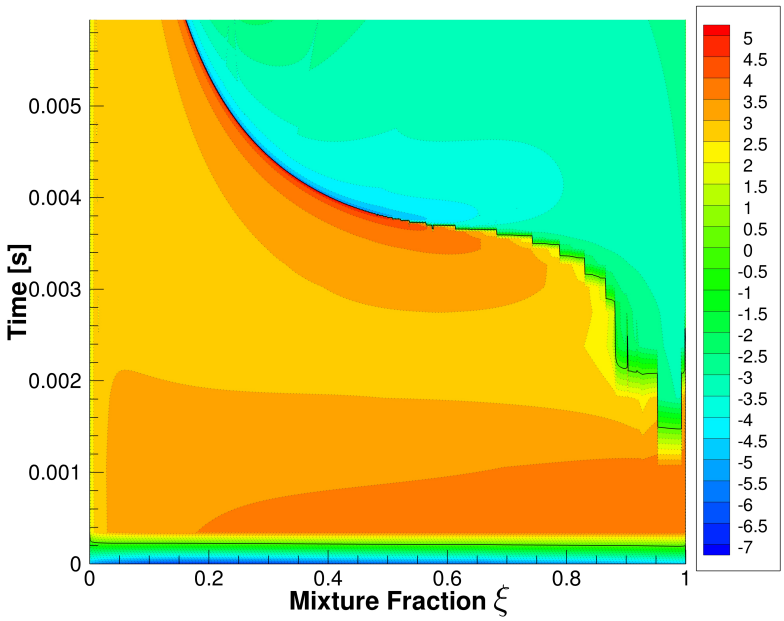

Figure 12: Case $\chi = 0\ s^{-1}$. Isocontour lines of Ω. The black line indicates the zero contour level.

value. The reaction-diffusion wave weakens while traveling towards rich mixtures, while it becomes stronger (faster) moving towards leaner mixtures. The steep temperature front generated by the reaction-diffusion wave moves from right to left towards the asymptotic limit marked as a red solid line in Fig. 14.

The effectiveness of diffusion in spreading ignition from the most ignitable mixture fraction value can be appreciated by superposing the isocontour lines of HCO mass fraction for the case $\chi = 0\ s^{-1}$ (black solid lines) and $\chi = 10\ s^{-1}$ (red dash dotted lines) as shown in Fig. 15. This comparison shows that the (apparent) propagation speed of the spontaneous ignition front tends to slow down while moving towards leaner mixtures. Instead, the (real) propagation speed of the reaction-diffusion wave increases in the same direction. Note also that diffusion delays the onset of ignition by contrasting the early stages of the kinetically controlled ignition.

It is worth to discuss how the most energetic scale evolves during both the explosive

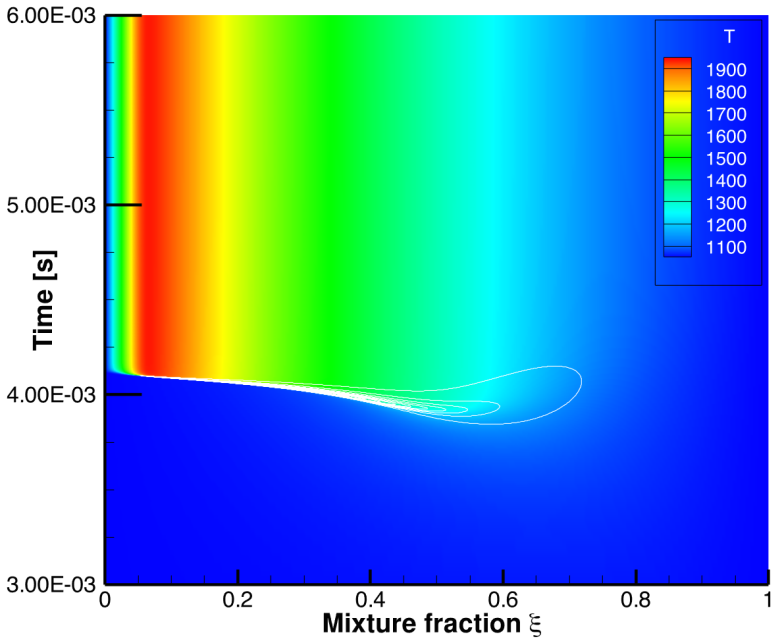

Figure 13: Case $\chi = 10\ s^{-1}$. Isocontour lines of temperature (T) and HCO mass fraction (thin white lines).

and dissipative regimes of the system dynamics. Also, the TSR ($\Omega_{\boldsymbol{g}}$) and the extended TSR ($\Omega_{\boldsymbol{g+L}}$) are compared and their comparison is exploited to gain physical insights on the dynamics.

With reference to Fig. 16, the locus of mixture fractions at which $\Omega_{\boldsymbol{g+L}} > 0$ peaks ($\partial[\Omega_{\boldsymbol{g+L}}]/\partial\xi = 0$) - at any given time - determines the most ignitable mixture conditions. Similarly, at any given time, the locus of extrema of $\Omega_{\boldsymbol{g+L}} < 0$ ($\partial[\Omega_{\boldsymbol{g+L}}/\partial\xi = 0$) identifies the "most dissipative state". The field of $\Omega_{\boldsymbol{g}}$ is similar at this level of magnification and thus it is not shown.

A closer look at Fig. 16, whose magnification around the flame front is shown in Fig. 17 (top), reveals that a region with a peak of $\Omega_{\boldsymbol{g+L}}$ is formed in the pre-heat zone - where kinetics and diffusion compete - of the reaction-diffusion wave. This feature is also noticeable in Fig. 19, which shows a slice of the field at t=4.059 $\times 10^{-3}$, where $\Omega_{\boldsymbol{g+L}}$ is denoted

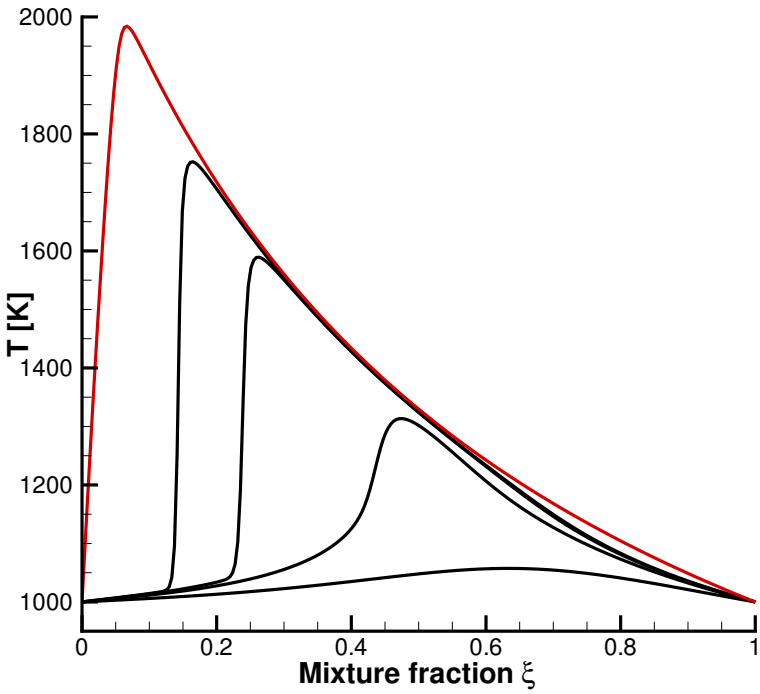

Figure 14: Case $\chi = 10\ s^{-1}$. Temporal snapshots of temperature field (transient states: black lines; stationary state: red line).

by green symbols.

Figure 18 shows the essential representation and characterization of the critical features of the flame front: the green region is the region where ω_{g+L} attains a peak ($\omega_{g+L} > 10^4$, *i.e.*, $\Omega_{g+L} > 4$), tracking the largest positive eigenvalue. This region may be identified as the flame front, *i.e.*, where the dynamics of the reactive-diffusive system is explosive and sufficiently fast. This region may be referred to as an auto-igniting region, since ω_g and ω_{g+L} coincide, meaning that the role of transport processes is here not pivotal. The red region corresponds to the region where ω_g and ω_{g+L} differ, *i.e.*, the deflagrative, diffusion-contributed, part of the flame front, which is also depicted in Fig. 19 as the red symbols valley in the region marked as B. This figure shows a time slice at $t = 4.059 \times 10^{-3} s$, with the deflagrative wave traveling from right to left. Analyzing this figure from left to right,

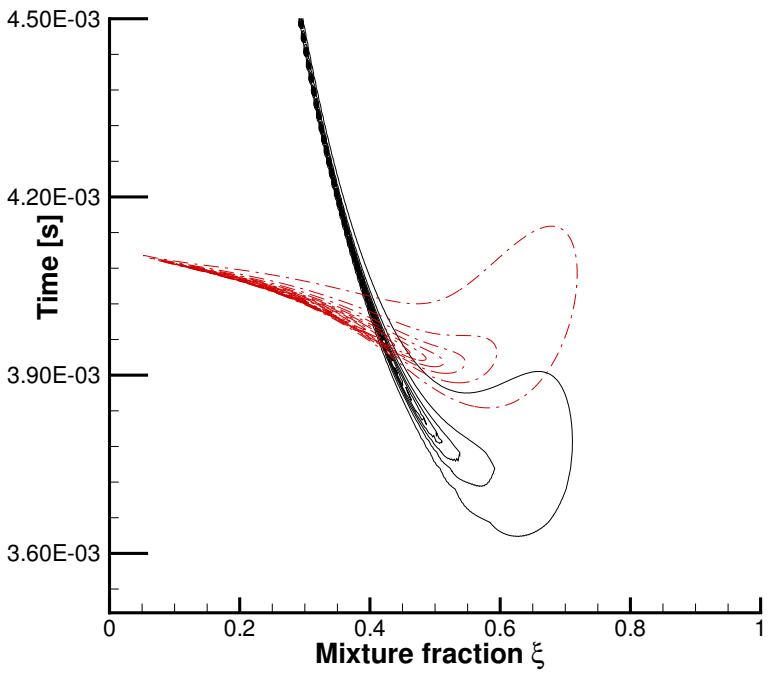

Figure 15: Spontaneous ignition front ($\chi = 0\ s^{-1}$, black solid lines) vs. reaction-diffusion wave ($\chi = 10\ s^{-1}$, red dash dotted lines) as described by HCO isocontour lines.

four distinct regions may be identified: (i) region A, where $\omega_{\boldsymbol{g}}$ and $\omega_{\boldsymbol{g+L}}$ coincide and are small and positive; (ii) region B, where $\omega_{\boldsymbol{g+L}}$ remains close to the positive eigenvalue, indicating the explosive nature of the reaction/diffusion system, while $\omega_{\boldsymbol{g}}$ becomes negative, pointing out the contractive nature of the system dynamics due to the chemical source term only; (iii) region C, where $\omega_{\boldsymbol{g}}$ becomes positive and coincident with $\omega_{\boldsymbol{g+L}}$; and (iv) region D, where the diffusive processes become negligible, and the system exhibits a contractive nature with both $\omega_{\boldsymbol{g}}$ and $\omega_{\boldsymbol{g+L}}$ being negative and coincident.

A detailed break-up analysis at time $t = 4.059 \times 10^{-3}$ s and $\xi = 0.19$ (see tables 3.4 and 3.5) allows to evaluate the contribution of all modes to $\omega_{\boldsymbol{g}}$ and $\omega_{\boldsymbol{g+L}}$; it was found that $\omega_{\boldsymbol{g}} = -1.54 \times 10^6 s^{-1}$ originates from two modes: 94% by #5 ($\lambda_5 = -1.49 \times 10^6\ s^{-1}$) and 5.7% by #4 ($\lambda_4 = -5.80 \times 10^6\ s^{-1}$), while $\omega_{\boldsymbol{g+L}} = +1.02 \times 10^5\ s^{-1}$ originates from two modes: 73% by #5 ($\lambda_7 = +1.68 \times 10^5\ s^{-1}$) and 26% by #5 ($\lambda_5 = -5.80 \times 10^6\ s^{-1}$).

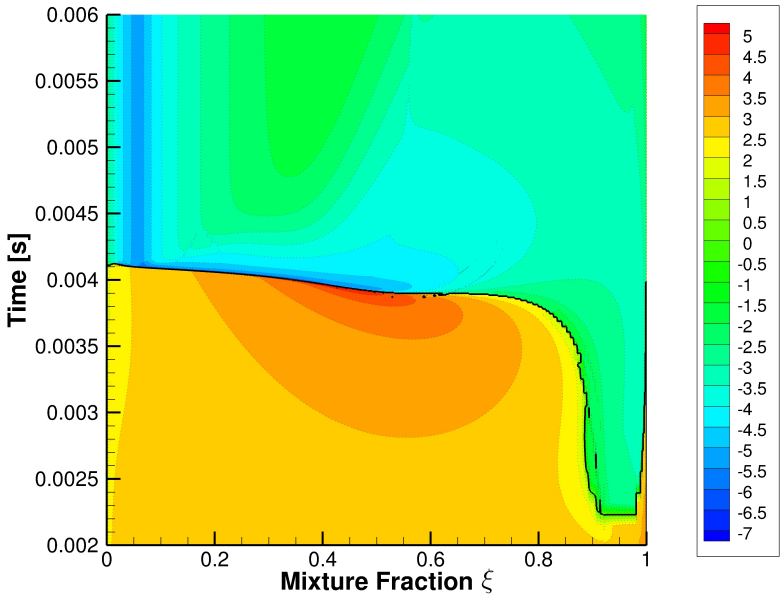

Figure 16: Case $\chi = 10\ s^{-1}$. Isocontour lines of $\Omega_{\boldsymbol{g+L}}$. The black line indicates the zero contour level.

Hence, modes with both positive and negative eigenvalues contribute to the TSR.

3.6.4 Important processes

It is straightforward to identify the processes, *i.e.* reactions and diffusion of species, participating to the modes mostly contributing to $\omega_{\boldsymbol{g}}$ and $\omega_{\boldsymbol{g+L}}$, by resorting to the participation indices defined in § 3.3.2 and 3.4.1.

It is worth to investigate the participation indices to both $\omega_{\boldsymbol{g}}$ and $\omega_{\boldsymbol{g+L}}$, shown in Fig. 20 and 21 respectively, for the time slice $t = 4.059 \times 10^{-3} s$. It is observed that in region A the behavior of the participation indices to $\omega_{\boldsymbol{g}}$ in the mixture fraction space, moving towards richer mixtures (from left to right), resembles the evolution in time of the indices computed for the below-crossover autoignition problem. If diffusion were not present, *i.e.* $\chi = 0$, this time slice would have shown the state of several batches of mixture, with different equivalence ratio, evolving independently in time, and photographed at $t = 4.059 \times$

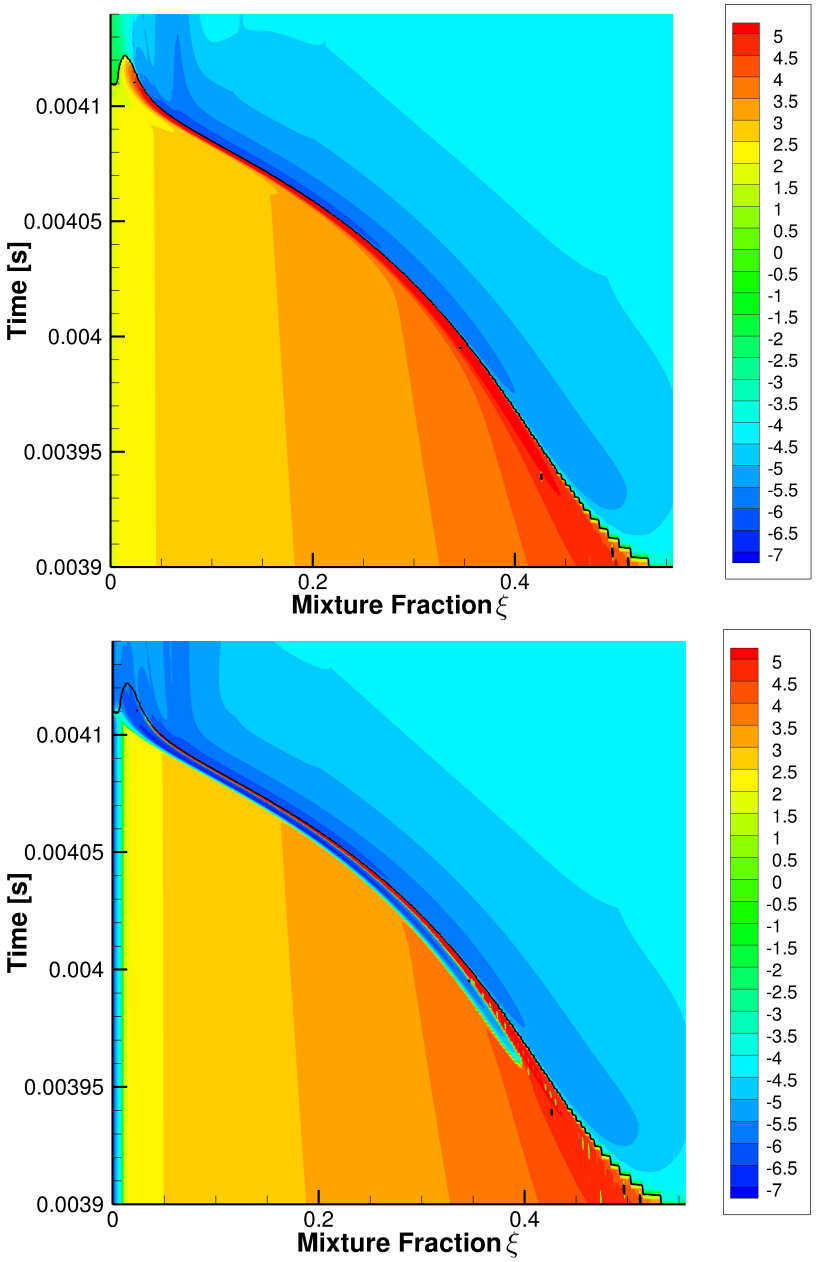

Figure 17: Case $\chi = 10\ s^{-1}$. Isocontour lines of $\Omega_{\boldsymbol{g+L}}$ (top) and $\Omega_{\boldsymbol{g}}$ (bottom)

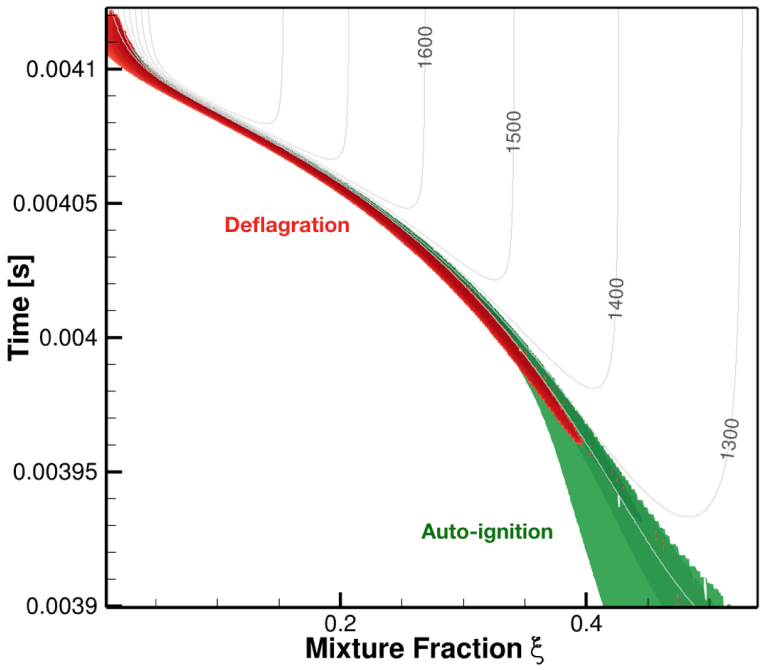

Figure 18: Case $\chi = 10\ s^{-1}$. Flame front identification and characterization: autoignition vs deflagration. Temperature iso-contours in grey.

10^{-3} s. Since the reactive-diffusion wave has not yet reached this region, the left-to-right evolution is approximately an initial composition effect that translates into different ignition delays (supposing that the chemical pathways do not vary much around stoichiometric conditions). In particular, Rb-18 and Rf-16 are dominant, while Rf-9 and Rf-1 show a growing importance. Note that, although the mixture is syngas, the ignition process is started by the hydrogen submechanism. Note also that the temperature/pressure condition of this flamelet falls in the below-crossover regime (see Fig. 9, valid for a stoichiometric H_2/air mixture). In region B, the reaction-diffusion wave travels from right to left. Here, the diffusion of temperature is the dominant process of the reactive-diffusive system right in front of the flame (wave) front. This is the region where $\omega_{\boldsymbol{g}}$ and $\omega_{\boldsymbol{g+L}}$ differ, and where also the respective PIs differ the most. Here, $\omega_{\boldsymbol{g}}$ is negative and mostly contributed by Rf-9. The effect of the reaction-diffusion wave is to enhance ignition (deflagrative effect),

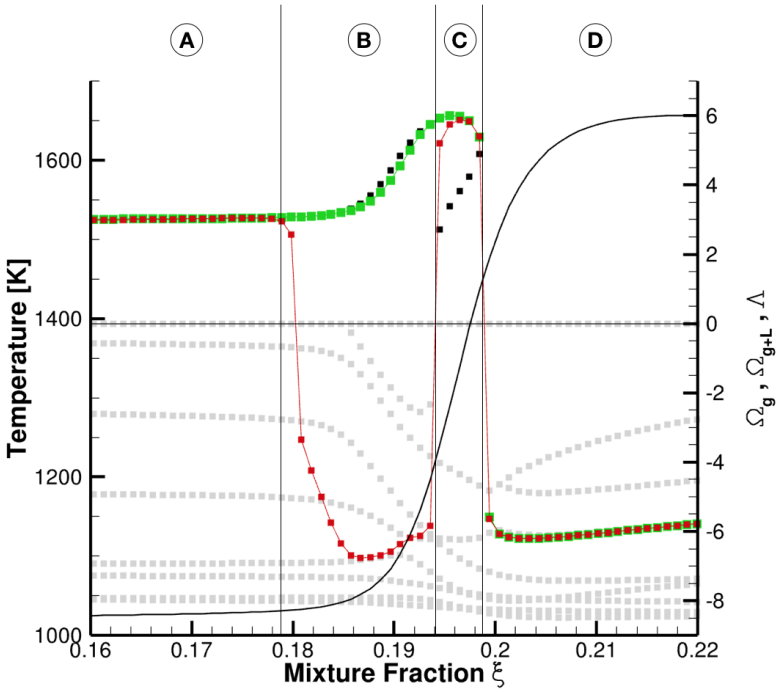

Figure 19: Case $\chi = 10\ s^{-1}$. Slice at $t = 4.059 \times 10^{-3}$, zoom on the flame front. $\Omega_{\boldsymbol{g}}$ (red) vs $\Omega_{\boldsymbol{g+L}}$ (green). Positive eigenvalues (black), negative eigenvalues (gray). Temperature (black line).

and chemistry alone would react in a dissipative way with the chain terminating reaction Rf-9. This explains the Rf-9 peak in Fig. 20, which differs from the auto-ignition case. In region C, the chain branching reaction Rf-1 is the largest contributor to heat release. Finally, in region D, thus behind the flame front, the carbon chemistry takes place as well, mostly through reaction Rb-26 (H + CO + M $\longrightarrow$ HCO + M).

In summary, the deflagrative wave accelerates the ignition process of the mixture to the left of the front, and the driving processes are mostly the diffusion of temperature and, to a less extent, diffusion of H, which in turn trigger Rf-1 earlier than the sequence Rb-18 / Rf-16 would have done in absence of transport.

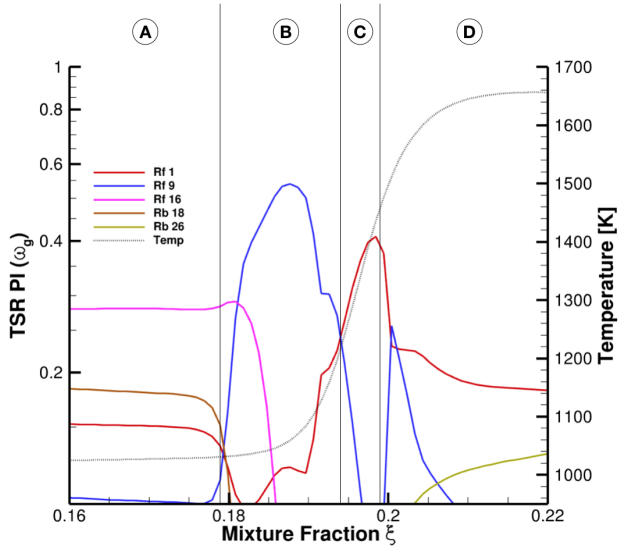

Figure 20: Participation Indices to $\omega_{\tilde{\tau}}$ at $t = 4.059 \times 10^{-3}$ s in the flame front region

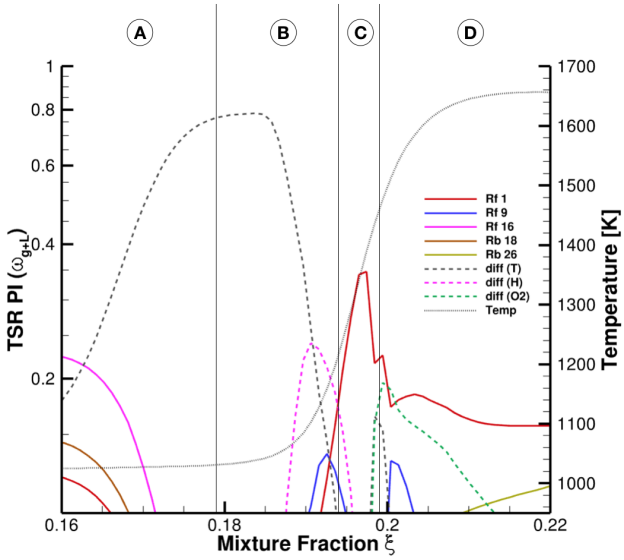

Figure 21: Participation Indices to $\omega_{\tilde{\tau}_{pde}}$ at $t = 4.059 \times 10^{-3}$ s in the flame front region

Table 3.4: TSR analysis, $\omega_{\boldsymbol{g}} = -1.545 \times 10^{6}$ s^{-1}, Case χ=10 s^{-1}, slice at t=t=4.059×10^{-3} s, $\xi = 0.19159$

active?	#	$P^{\omega_{\boldsymbol{g}}}_{mode_i}$	Amplitude f	$\bar{W}_i$	Re(λ_i)	$\bar{W}_i \cdot \lambda_i$
NO	1	3.477×10^{-9}	5.368×10^{-6}	4.099×10^{-11}	-1.312×10^{8}	5.379×10^{-3}
NO	2	1.590×10^{-6}	-1.437×10^{-4}	2.937×10^{-8}	-8.365×10^{7}	2.457
NO	3	3.142×10^{-5}	-1.058×10^{-3}	1.592×10^{-6}	-3.054×10^{7}	4.860×10^{1}
YES	4	5.712×10^{-2}	1.034×10^{-1}	1.522×10^{-2}	-5.806×10^{6}	8.836×10^{4}
YES	5	9.420×10^{-1}	8.288×10^{-1}	9.771×10^{-1}	-1.492×10^{6}	1.457×10^{6}
NO	6	1.219×10^{-5}	-6.420×10^{-3}	5.862×10^{-5}	-3.216×10^{5}	1.885×10^{1}
NO	7	8.309×10^{-4}	-7.325×10^{-2}	7.632×10^{-3}	1.684×10^{5}	1.285×10^{3}
NO	8	0.0	-3.682×10^{-8}	1.928×10^{-15}	-2.004×10^{3}	3.863×10^{-12}
NO	9	9.548×10^{-14}	1.987×10^{-5}	5.613×10^{-10}	-2.632×10^{2}	1.477×10^{-7}
NO	10	0.0	0.0	0.0	2.899×10^{-8}	0.0
NO	11	0.0	0.0	0.0	-2.048×10^{-10}	0.0
NO	12	0.0	0.0	0.0	-1.824×10^{-11}	0.0
NO	13	0.0	0.0	0.0	0.0	0.0

Table 3.5: Extended TSR analysis, $\omega_{\boldsymbol{g+L}} = +1.025 \times 10^5 s^{-1}$, Case χ=10 s^{-1}, slice at t=4.059×10^{-3} s, $\xi = 0.19159$

active?	#	$P^{\omega_{\boldsymbol{g+L}}}_{mode_i}$	Amplitude h	$\bar{W}_{i,pde}$	Re(λ_i)	$\bar{W}_{i,pde} \cdot \lambda_i$
NO	1	4.000×10^{-8}	-1.055×10^{-5}	6.727×10^{-11}	-1.312×10^{8}	8.8278×10^{-3}
NO	2	6.336×10^{-10}	1.664×10^{-6}	1.674×10^{-12}	-8.365×10^{7}	1.400×10^{-4}
NO	3	5.525×10^{-8}	2.573×10^{-5}	3.998×10^{-10}	-3.054×10^{7}	1.221×10^{-2}
NO	4	6.358×10^{-4}	-6.329×10^{-3}	2.420×10^{-5}	-5.806×10^{6}	1.405×10^{2}
YES	5	2.673×10^{-1}	-2.561×10^{-1}	3.961×10^{-2}	-1.492×10^{6}	5.908×10^{4}
NO	6	5.373×10^{-7}	7.817×10^{-4}	3.692×10^{-7}	-3.216×10^{5}	1.187×10^{-1}
YES	7	7.320×10^{-1}	-1.261	9.604×10^{-1}	1.684×10^{5}	1.618×10^{5}
NO	8	9.840×10^{-13}	-1.340×10^{-5}	1.086×10^{-10}	-2.004×10^{3}	2.174×10^{-7}
NO	9	4.530×10^{-10}	-7.935×10^{-4}	3.804×10^{-7}	-2.632×10^{2}	1.001×10^{-4}
NO	10	0.0	0.0	0.0	2.899×10^{-8}	0.0
NO	11	0.0	0.0	0.0	-2.048×10^{-10}	0.0
NO	12	0.0	0.0	0.0	-1.824×10^{-11}	0.0
NO	13	0.0	0.0	0.0	0.0	0.0

3.7 Analysis of a turbulent premixed flame

The ultimate goal of the CSP/TSR analysis is to provide physical understanding of large and complex reactive flows predictions, which offer a large amount of information - typically the state functions in each computational point - which are difficult to translate into global combustion characteristics. An attractive feature that is commonly attempted to identify is the flame front and the related explosive propensity of a mixture. This interest pertains to practical applications, where ignition is desired to be under strict control due to safety and performance issues. In this section, the investigation of an existing 3D DNS solution [47, 48] of a freely-propagating statistically stationary turbulent H_2/air premixed flame is carried out. The detailed kinetic mechanism employed in the simulations was the scheme of *Burke et al.* [49] designed for hydrogen combustion and the initial condition is a steady laminar flame with T(0)=300K, p(0)=1 atm, $\phi = 0.7$.

The analyzed dataset here presented is a representative 2D slice of the field, taken at one time-step, in the mid-z plane. The choice of the spatial and temporal position is not relevant to the scope of this demonstration, moreover the flame is statistically stationary and the lateral boundary conditions are periodic. The considered DNS case is representative of the thin reaction zone (TRZ) combustion regime [50]. It is characterized by a turbulent Reynolds number $Re_t = \rho_0 u' l_T/\mu_0$=1623, a Damköhler number $Da = l_T S_L/u'\delta_{th}$ =2.8 and a Karlovitz number $Ka = (\rho_0 S_L \delta_{th}/\mu_0)^{0.5}(u'/S_L)^{1.5}(l/\delta_{th})^{-0.5}$ =14.4, where μ_0 is the unburned gas viscosity, $\delta_{th} = (T_{ad} - T_0)/max\,|\nabla T|_L$ is the thermal flame thickness, the subscript 'L' is used to refer to unstrained laminar flame quantities, the turbulent length scale to flame thickness ratio is $l_T/\delta_{th} = 14.0$, the inflow normalized root-mean-square turbulent velocity fluctuation is u'/S_L =5. These inflow values are summarized in table 3.6.The domain size is $20mm \times 10mm \times 10mm$ and the domain has been discretised by a uniform Cartesian grid of $512 \times 256 \times 256$ cells.

Table 3.6: List of the inflow turbulence parameters.

u'/S_L	l_T/δ_{th}	Re_t	Da	Ka
5	14.0	1623	2.8	14.4

A typical progress variable employed for the study of such fields is a temperature-based variable defined as $C_T := (T - T_{min})/(T_{max} - T_{min})$.

The spatial evolution of temperature and the mass fractions of H and OH at the chosen time-step (t=2.19 ms) are reported in Fig.22, where the iso-contour lines of C_T are superimposed. The aim of the analysis presented in the following is to explore, by means of the CSP-TSR tools, the role of the different driving processes, i.e., convection, diffusion, and reactions, and their mutual interactions. Convection can be accounted for with respect to a laboratory frame of reference or with respect to the flame front, or can be absorbed in the total derivative when following a Lagrangian description of the flow. In this work, the latter interpretation is adopted to focus on the interplay between diffusion and reactions.

The reactions that were found to be the most significant and will be further referred to in the current study, are summarized in Table 3.7. Note that the reactions numbering differs from the one employed in the previous sections, since the kinetic scheme is different.

Table 3.7: The reactions providing significant contribution to the dynamics of the system.

1:	$H + O_2 \leftrightarrow O + OH$	14:	$HO_2 + O \leftrightarrow O_2 + OH$
2/3:	$O + H_2 \leftrightarrow H + OH$	15:	$HO_2 + OH \leftrightarrow H_2O + O_2$
4:	$H_2 + OH \leftrightarrow H_2O + H$	18:	$H_2O_2\ (+M) \leftrightarrow 2OH\ (+M)$
11:	$H + O_2\ (+M) \leftrightarrow HO_2\ (+M)$	19:	$H_2O_2 + H \leftrightarrow H_2O + OH$
13:	$HO_2 + H \leftrightarrow 2OH$		

Flame topology It is worth to recall that Ω_{g+L} and Ω_g are weighted averages of both the positive and negative system eigenvalues, and are defined and insightful over the whole domain. For this reason, these metrics are employed to topologically characterize the reactive field, and to identify the flame front and its internal structure.

In particular, the analysis of the scatter plot of Ω_{g+L} and Ω_g in the entire domain as function of C_T, shown in Fig. 23, allows to identify different qualitative behaviors of the reactive flow. Intrinsic to the meaning of the tangential stretching rate is the association of a different qualitative behavior with the sign of either Ω_{g+L} or Ω_g. Therefore, the edge

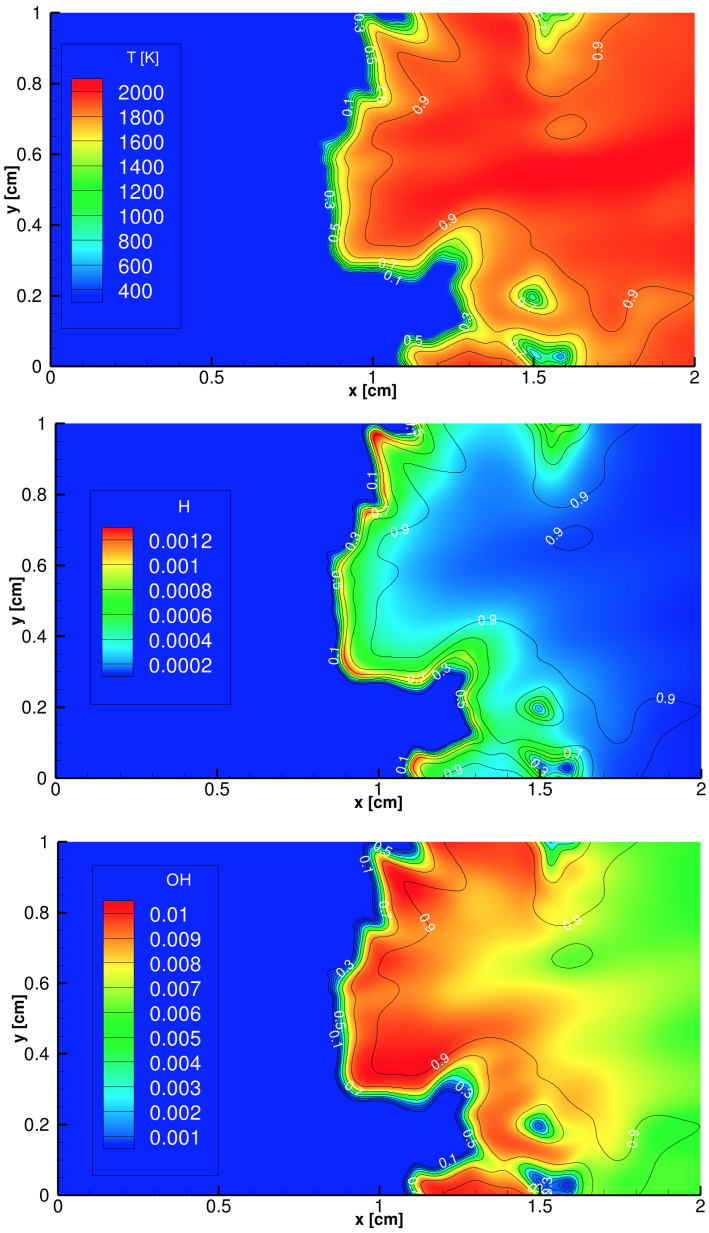

Figure 22: The spatial evolution of temperature and the mass fractions of H and OH at the chosen time-step (t=2.19 ms). Iso-contours of C_T in black.

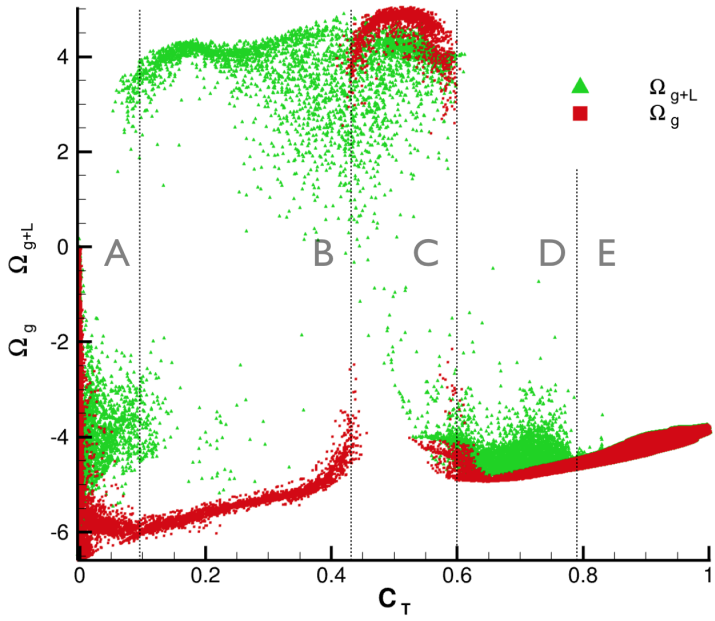

Figure 23: Scatter plots of $\Omega_{\boldsymbol{g}}$ and $\Omega_{\boldsymbol{g+L}}$ in the entire field as function of C_T.

of each region is identified where either $\Omega_{\boldsymbol{g+L}}$ or $\Omega_{\boldsymbol{g}}$ change sign. Thus in Fig. 23, four regions are observed within the flame front, and a fifth region connecting the flame front to the downstream fully burnt condition. In region **A**, $\Omega_{\boldsymbol{g+L}} < 0$ and $\Omega_{\boldsymbol{g}} < 0$, in region **B**, $\Omega_{\boldsymbol{g+L}} > 0$ and $\Omega_{\boldsymbol{g}} < 0$, in region **C**, $\Omega_{\boldsymbol{g+L}} > 0$ and $\Omega_{\boldsymbol{g}} > 0$, while in regions **D** and **E**, $\Omega_{\boldsymbol{g+L}} < 0$ and $\Omega_{\boldsymbol{g}} < 0$. Regions **D** and **E** are considered to be different because of the different scatter degree for $\Omega_{\boldsymbol{g+L}}$.

Observation of Fig. 23 reveals that the flame front lies within the interval $0.01 < C_T < 0.8$. As shown in Fig. 24, this allows to clip the reactive flow field where $0.01 < C_T < 0.8$ to graphically identify the flame front features. The colored contours in Fig. 24 represent $\Omega_{\boldsymbol{g+L}}$, red when positive, while the black dashed line inscribes the sub-region where $\Omega > 0$. A comparison of the spatial distributions of $\Omega_{\boldsymbol{g+L}}$ and $\Omega_{\boldsymbol{g}}$ reveals that $\Omega_{\boldsymbol{g}}$ is positive in a much thinner region than $\Omega_{\boldsymbol{g+L}}$, this making $\Omega_{\boldsymbol{g}}$ a good candidate for further topological analysis such as the local flame curvature evaluation.

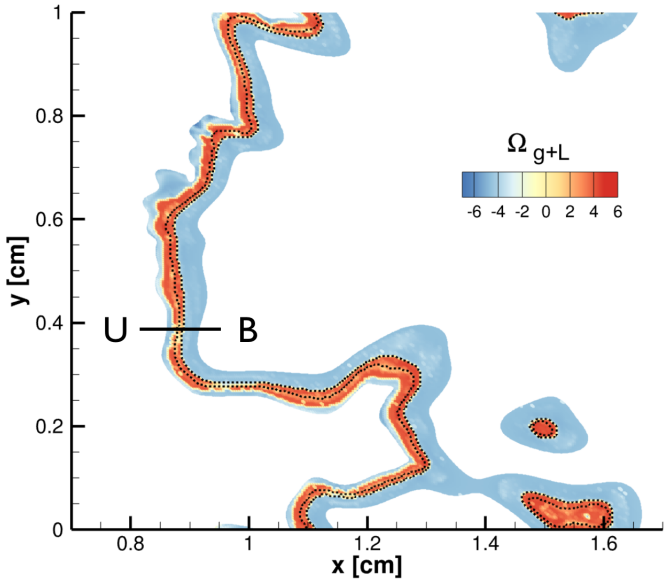

Figure 24: Flame front topology, with $\Omega_{\boldsymbol{g+L}}$ colored contours and $\Omega = 0$ isocontour (black dashed line).

Flame structure The detailed characterization of the processes in the five regions can be carried out by means of the TSR-PI ($P^{\omega_{\boldsymbol{g+L}}}_{\text{process}}$) indices evaluated (i) in the entire reactive flow (Figs. 25 and 26) or (ii) along the slice taken across the flame front (Figs. 27 and 28) between the points U-nburnt and B-urnt as shown in Fig. 24.

Entire reactive flow Figure 25 shows the scatter plots of $P^{\omega_{\boldsymbol{g+L}}}_{\text{Diff(H)}}$, $P^{\omega_{\boldsymbol{g+L}}}_{\text{Diff(H}_2\text{)}}$ and $P^{\omega_{\boldsymbol{g+L}}}_{\text{Diff(T)}}$. The observation of the aforementioned scatter plots reveals that diffusion of H is the dominant transport process in region **A**, where $P^{\omega_{\boldsymbol{g+L}}}_{\text{Diff(H)}}$ reaches the peak value of ∼60%. The participation index of H diffusion exhibits a second peak of ∼40% in region **B**. Two peaks of $P^{\omega_{\boldsymbol{g+L}}}_{\text{Diff(T)}}$ are observed, the first, with peak values of ∼40%, located at the boundary between regions **A**, **B**, the second, with peak values of ∼20%, located at the boundary between regions **B**, **C**. In region **C**, $P^{\omega_{\boldsymbol{g+L}}}_{\text{Diff(H)}}$ is lower than ∼10%, while it is observed the growth of

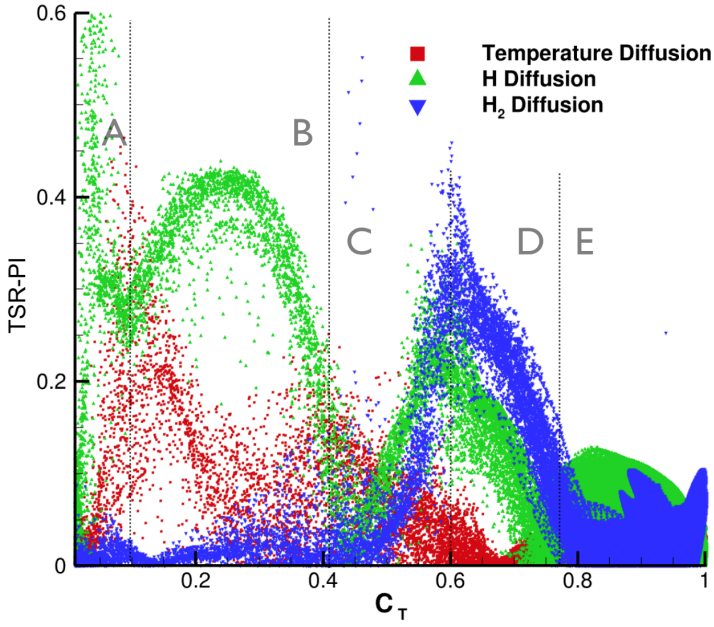

Figure 25: Scatter plots of the TSR-PIs: $P^{\omega_{g+L}}_{\mathrm{Diff(H)}}$, $P^{\omega_{g+L}}_{\mathrm{Diff(H_2)}}$ and $P^{\omega_{g+L}}_{\mathrm{Diff(T)}}$

$P^{\omega_{g+L}}_{\mathrm{Diff(H_2)}}$ and $P^{\omega_{g+L}}_{\mathrm{Diff(T)}}$. Temperature diffusion participation index reaches a local maximum ($\sim$20%) at the boundary between regions **C** and **D**. A similar behavior is observed for H_2 diffusion, with $P^{\omega_{g+L}}_{\mathrm{Diff(H_2)}}$ increasing in region **C** and reaching the maximum value of $\sim$40% at the boundary with region **D**. Participation indices of both H_2 and temperature decrease throughout region **D**, and reach values lower than $\sim$10% in region **E**.

In Fig. 26 are reported the scatter plots of $P^{\omega_{g+L}}_{\mathrm{Rf\text{-}11}}$, $P^{\omega_{g+L}}_{\mathrm{Rf\text{-}1}}$ and $P^{\omega_{g+L}}_{\mathrm{Rf\text{-}15}}$. These scatter plots reveal that region **A** is characterized by $P^{\omega_{g+L}}_{\mathrm{Rf\text{-}15}}$, reaching values of $\sim$60%, and by $P^{\omega_{g+L}}_{\mathrm{Rf\text{-}11}}$, whose peak value of $\sim$20% is located at the boundary between regions **A** and **B**. In region **B**, $P^{\omega_{g+L}}_{\mathrm{Rf\text{-}15}}$ decreases to less that $\sim$10%, while $P^{\omega_{g+L}}_{\mathrm{Rf\text{-}11}}$ is the dominant reactive process of the region, with almost constant value of $\sim$10%. In region **C**, Rf-1 and Rf-11 exhibit local peaks of $\sim$20% and $\sim$15% respectively. In regions **D** and **E**, the relative importance of Rf-1 diminishes, with $P^{\omega_{g+L}}_{\mathrm{Rf\text{-}1}}$ reaching values lower than $\sim$10%. A local minimum of $P^{\omega_{g+L}}_{\mathrm{Rf\text{-}11}}$ is observed at the boundary between regions **C** and **D**, followed by a growth up

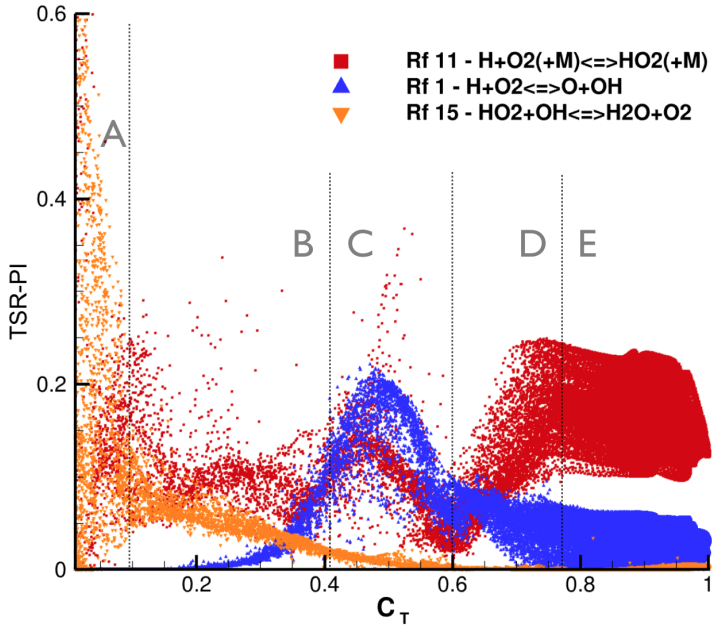

Figure 26: Scatter plots of the TSR-PIs: $P^{\omega_{g+L}}_{\text{Rf-11}}$, $P^{\omega_{g+L}}_{\text{Rf-1}}$ and $P^{\omega_{g+L}}_{\text{Rf-15}}$

to ∼20% throughout region **D**. The participation index $P^{\omega_{g+L}}_{\text{Rf-11}}$ keeps a constant value of ∼15% in the entire post-flame region **E**, while $P^{\omega_{g+L}}_{\text{Rf-1}}$ remains below the ∼10%.

The behavior observed across the flame front is confirmed throughout the entire field, with a large dispersion in the post-flame region. As an example, Fig. 29 shows that the spatial distribution of $P^{\omega_{g+L}}_{\text{Rf-1}}$ is affected by the flame curvature in both the flame front and in the post-flame region.

Slice of flame front A more detailed characterization of the processes in the five regions of the reactive flow is obtained inquiring the TSR-PI ($P^{\omega_{g+L}}_{\text{process}}$) along the line segment between the points U and B shown in Fig. 24.

The inspection of the most participating diffusive processes to ω_{g+L}, reported in Fig. 27, reveals that in regions **A** and **B**, H diffusion (∼ 35%) and, to a lesser extent (∼ 15%), temperature diffusion are dominant over kinetics. The adduction of H in region **A** is a pivotal process, feeding radicals to reactions Rf-11 , shown in Fig. 28, which initiate the

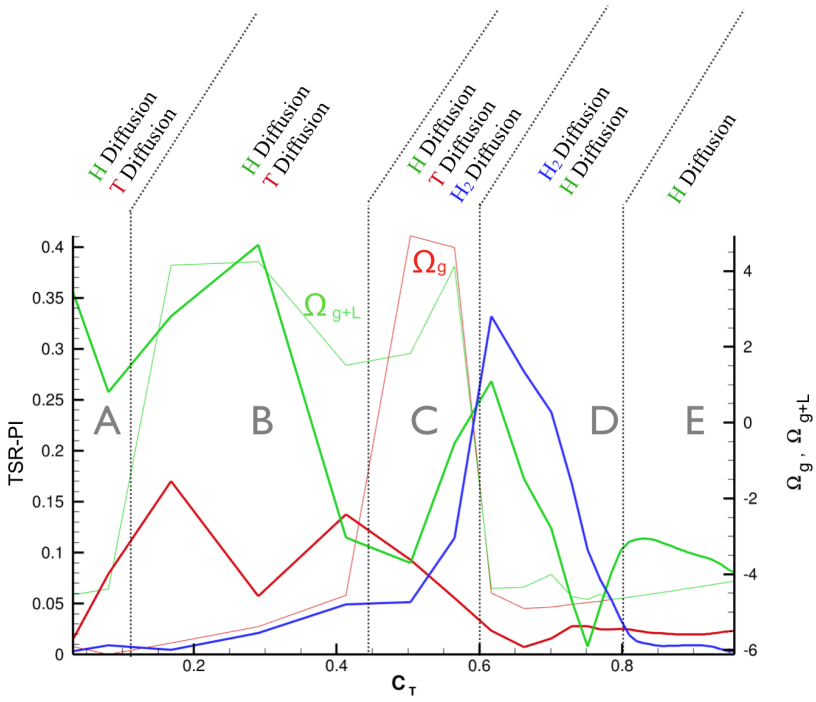

Figure 27: TSR-PIs of the dominant diffusive processes.

sequence of chemical kinetic events discussed in the following. In region **C** the role of diffusion is lowered, while in **D**, a significant growth of H_2 and H is apparent.

As shown in Fig. 28, in region **A**, H and HO_2 lead to OH radical through the reactions sequence Rf-11, Rf-13; in region **B**, while the chain branching reaction Rf-13 leads to OH production, the chain terminating reactions Rf-11 and Rf-15 recombine H and OH to the more stable radical HO_2 and H_2O. In region **C**, both $\omega_{\boldsymbol{g}}$ and $\omega_{\boldsymbol{g+L}}$ are positive, and is observed the growth of the relative importance of the reactions responsible of the production of OH, H and O radicals. Regions **D** and **E** are contractive, with both $\omega_{\boldsymbol{g}}$ and $\omega_{\boldsymbol{g+L}}$ being negative. In particular, in region **E** are observed: the balance between reactions Rf-4 and Rb-4; and an increasingly predominant role of the chain terminating reaction Rb-10, recombining OH and H radicals into H_2O.

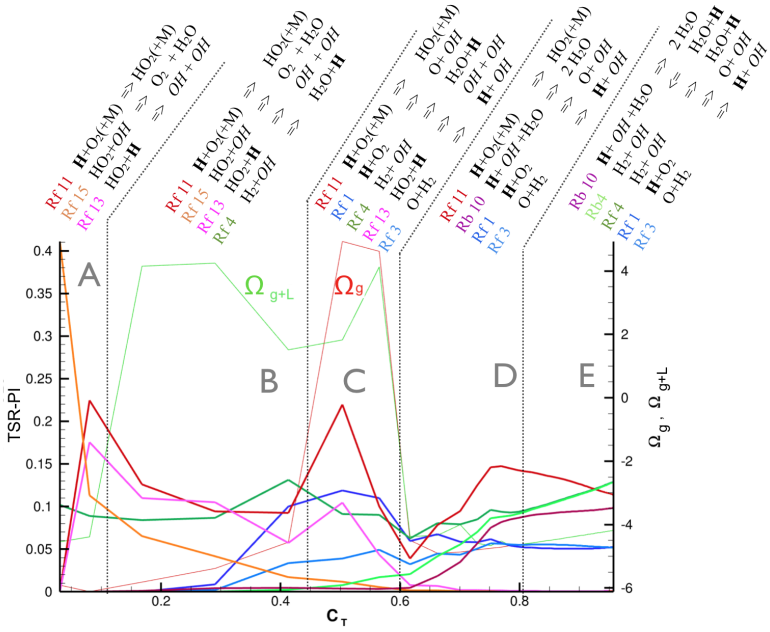

Figure 28: TSR-PIs of the dominant chemical reactions.

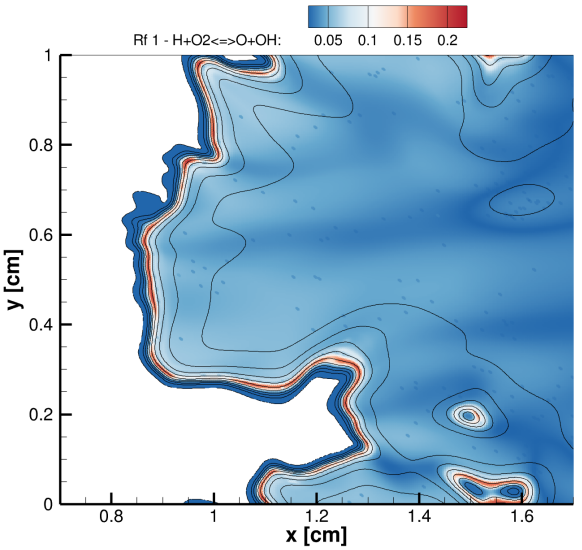

Figure 29: Contour plot of $P^{\omega_{g+L}}_{\text{Rf-1}}$

Chapter 4

CSP-based tools for simplification

4.1 Kinetic mechanisms simplification

This chapter will be devoted to the exploitation of the CSP method towards the simplification of chemical kinetic mechanisms. In the first part, suitable importance indices are defined to assess the contribution of a chemical reaction to the production/consumption of a set of species of interest, and a rigorous algorithmic procedure, successfully employed in several works, is briefly outlined for homogeneous problems. The pivotal tasks of a simplification campaign are then described, with special emphasis on how to conveniently choose a representative dataset to be fed to the algorithm. In the second part, three improvements of the algorithm are presented for the first time, involving entropy participation indices (EPI), a tangential stretching rate (TSR)-defined kernel set and a variable tolerance approach, respectively. A test-case is performed to compare them and to highlight their advantages with respect to the traditional algorithm. Lastly, the algorithm is extended to steady-state reactive-diffusive problems, and a practical application involving the generation of skeletal mechanisms for non-premixed combustion in hybrid rockets is presented.

4.1.1 Simplification algorithm

In the CSP-based skeletal reduction algorithm, the criterion for selecting the subset of reactions and species to be retained in the simplified mechanism is based on their relevance to the fast and slow dynamics of a prescribed set of "target" species, whose concentration is deemed to be accurately reproduced by the skeletal mechanism. This algorithm is based on the ability to decompose, at any time epoch and space location, the chemical kinetic processes into fast and slow components, as offered by CSP, and to identify the processes that produce the most significant contribution in either the fast or slow components. As a measure of the degree to which a reaction contributes to the fast/slow dynamics of the target species, the algorithm adopts the fast and slow CSP importance indices [51], which measure the contribution of each elementary reaction in the detailed mechanism to the fast and slow components of each species production rate. Next, a new set of active species is identified by collecting all the species participating in the selected reactions. The separate examination of fast and slow subspaces allows to distinguish the fast processes mostly participating to the emergence of the slow invariant manifold and the slow processes driving the solution along the manifold itself, as demonstrated in [51].

The relative contribution of a reaction k in the production/consumption of the species i in either the fast or slow subspace can be assessed by means of a fast/slow importance index defined as:

$$(I)^i_{k_{\rm slow}} = \frac{\sum_{s=M+1}^{N} a^i_s(\boldsymbol{b}^s \cdot \boldsymbol{S}_k) r^k}{\sum_{kk=1}^{2N_r} \mid \sum_{s=M+1}^{N} a^i_s(\boldsymbol{b}^s \cdot \boldsymbol{S}_{kk}) r^{kk} \mid}, \tag{4.1.1}$$

$$(I)^i_{k_{\rm fast}} = \frac{\sum_{r=1}^{M} a^i_r(\boldsymbol{b}^r \cdot \boldsymbol{S}_k) r^k}{\sum_{kk=1}^{2N_r} \mid \sum_{r=1}^{M} a^i_r(\boldsymbol{b}^r \cdot \boldsymbol{S}_{kk}) r^{kk} \mid}, \tag{4.1.2}$$

where the index M in the summations is defined according to the criterion (2.2.9).

The algorithm operates on a database of states $D = \{\boldsymbol{y}^{(1)}, \cdots, \boldsymbol{y}^{(K)}\}$, where $\boldsymbol{y} \in \mathbb{R}^{N+1}$ is the state vector composed of temperature and the N_s mass fractions. For each state point, the algorithmic tool computes $\boldsymbol{g}(\boldsymbol{y})$, the corresponding Jacobian matrix $\boldsymbol{J_g}$ and the number M of exhausted modes. These data allow the slow and fast importance indices to be computed using Eqs.(4.1.1) and (4.1.2), which, in turn, determine the reactions to be eliminated from the detailed mechanism as those having an index value smaller

than the user-specified tolerance with respect to the target species set. The subsets of species/reactions retained in each state point are finally merged to build a global skeletal mechanism, relative to the whole database D.
Note that if, at a particular state, a given species is present in trace quantity and its rate of production/consumption is also negligible, its importance index is not a meaningful quantity, often yielding indeterminate values, and must not be employed in a CSP analysis.

This approach is very useful in generating a spectrum of simplified mechanisms of different sizes, each associated with a given degree of fidelity in predicting the chosen quantities of interest, specified by a threshold on the importance indices. The final choice of the simplified mechanism consists in finding a compromise between the dimensionality reduction and the required accuracy in the replication of the behavior of the species of interest. Indeed, the skeletal mechanisms are tailored over the target species, hence the other species are not expected to be accurately reproduced.

So far, the CSP-based automatic chemical mechanism simplification algorithm has been successfully employed in the context of purely reactive systems [23, 52]. The skeletal mechanisms generated with this procedure proved to be capable of replicating the ignition transient of homogeneous reactors, as well as the numerical predictions of laminar and turbulent premixed flames [53].

Table 4.1 and Fig. 30 show the logical structure and block diagram of the algorithmic procedure, where the user-specified input parameters are a database of states D provided by any numerical time-integration of an ignition problem, the kernel set of initial species S_0 and the value of the tolerance threshold τ.

4.1.2 Choice of a proper dataset

A detailed mechanism is usually designed to cope with a wide rage of operating conditions. The effectiveness of the simplification algorithm relies on the capability of generating smaller chemical mechanisms able to accurately describe a subset of chemical species, in a narrower range of operating conditions, for a specific class of problems.

The key point in the simplification process is the inspection of the detailed mechanism behavior when it deals with the physical problem and the operating conditions of inter-

For all $\mathbf{u}_n \in D$:

{ **Start with kernel set of active species:** $S_{[h=0]} = S_0$;

While $\left[S_{[h]}(\mathbf{u}_n, tol, S_0) = S_{[h-1]}(\mathbf{u}_n, tol, S_0)\right]$

{ $h = h + 1$;

Define new active reactions set:

$$R_{[h]}(\mathbf{u}_n, tol, S_0) = \{k : \left(I_k^i(\mathbf{u}_n)\right)_{slow} > tol; i \in S_{[h-1]}(\mathbf{u}_n, tol, S_0)\} \cup \{k : \left(I_k^i(\mathbf{u}_n)\right)_{fast} > tol; i \in S^{rad}_{[h-1]}(\mathbf{u}_n, tol, S_0)\};$$

Define new active species set:

$$S_{[h]}(\mathbf{u}_n, tol, S_0) = \{i : \nu_{ik} \neq 0; k \in R_{[h]}(\mathbf{u}_n, tol, S_0)\};$$

};

Define local active reactions set: $R_\ell(\mathbf{u}_n, tol, S_0) = R_{[h]}$;

};

Define global active reactions set: $R(tol, S_0) = \bigcup_{n\in[1,N_{sol}]} R_\ell(\mathbf{u}_n, tol, S_0)$;

Define global active species set: $S(tol, S_0) = \{i : \nu_{ik} \neq 0; k \in R(tol, S_0)\}$.

Table 4.1: Structure of the simplification algorithm

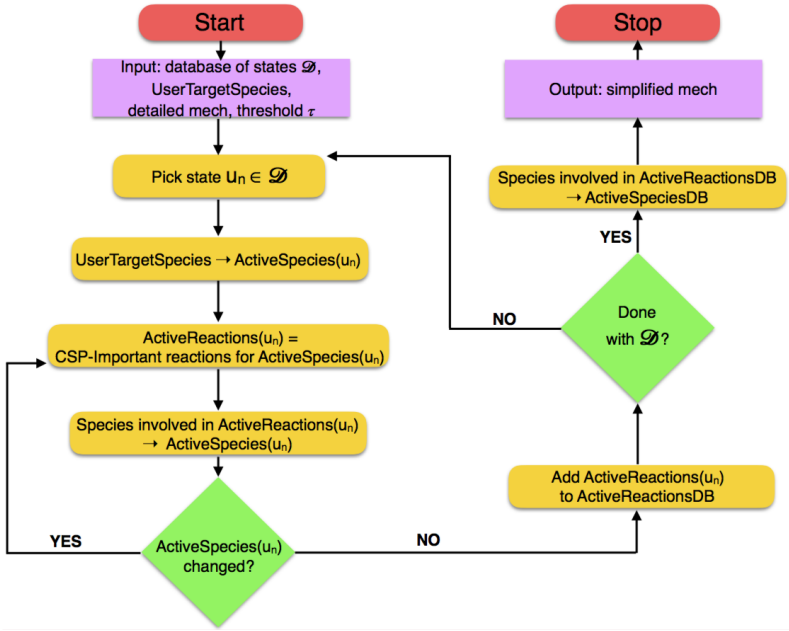

Figure 30: Block diagram of the simplification algorithm

est. Hence, the choice of the database of states to be fed into the algorithm is pivotal for the generation of simplified mechanisms that are accurate for the application purposes. Nonetheless, the use of detailed mechanisms, often consisting of hundreds of species, constrains the generation of databases to simple model problems that are computationally affordable.

Hence, according to the application and the desired features that he/she would like to accurately reproduce, the user must carefully design the simplification campaign by making decisions on: (i) the detailed mechanism to use as baseline, (ii) the model problem, representative of the physics of interest, to employ with the detailed mechanism for the database generation, (iii) the initial/boundary conditions of the model problem that allow to explore the sought-after features of the detailed kinetics.

Typical simple model problems are zero-dimensional -homogeneous reactor- auto-ignitions, nonetheless also laminar flamelet models or laminar premixed flame models may be used,

depending on the application purposes.

The choice of the initial/boundary conditions determines the collection of thermo-chemical states of the system that are generated by any solver and that are analyzed by the simplification algorithm. It follows that, for achieving the best results, those states must contain the kind of information that the user would like to maintain in the reduced model. If multiple targets are demanded, *e.g.* low- and high-temperature kinetics simultaneously, the database of states should include both, turning the campaign into a comprehensive campaign.

Lastly, a special attention should be paid to the solver that produces the collection of states. Usually, the accuracy and the number of states that are computed are subject to the user decision. A number of questions still remains open regarding the number of discrete points to feed into the algorithm, *i.e.* their sampling along the dynamics evolution, and their space/time location. All these decisions have an impact on the outcomes of the algorithm which are not known *a-priori* and should be examined, however these will not be investigated in this work, where the decision on how to sample the discrete points along time-trajectories is left to the solver itself. This usually means that discrete points are sampled based on the solver internal time-step.

4.1.3 Error measures

An *a-posteriori* error analysis is needed to assess the quality of a given simplified mechanism because the highly non linear character of the system of interest renders it impossible to derive *a-priori* error estimates. In general, we look for simplified mechanisms that are both computationally efficient, *i.e.* made up of a small number of species, and accurate in replicating some relevant features of the predictions from the detailed mechanism, which features are termed as QoIs, such as the ignition delay time and the transient evolution and equilibrium composition of the species of interest and temperature.

The discrepancies between ignition trajectories $X_i^d(t)$ and $X_i(t)$, $i = 1, \ldots, N+1$, generated by detailed and simplified models respectively, can be assessed with different metrics. The two most natural choices involve errors among solution trajectories (i) in the $\{t, X_i(t)\}$ phase space, and/or (ii) in the $\{\psi(t), X_i(t)\}$ phase space, where ψ is a suitable

progress variable and time t acts as a parametric abscissa.

The $\{t, X_i(t)\}$ phase space is suitable for ignition delay time measurements. A relative error on ignition delay time may be defined as:

$$E_{\text{ign}} = \frac{t_{\text{ign}} - t^d_{\text{ign}}}{t^d_{\text{ign}}} = \frac{\Delta t_{\text{ign}}}{t^d_{\text{ign}}} \tag{4.1.3}$$

where t^d_{ign} is the ignition delay of the detailed mechanism-based prediction.

On the other hand, Valorani *et. al.* [54] observed that, because of the exponential dependence of the ignition delay time on model parameters, the error in solution trajectories measured in the $\{t, X_i(t)\}$ plane can exhibit non-monotonic convergent behavior with decreasing degree of simplification of the kinetic mechanism. This non-monotonicity comes about as a consequence of the elimination in total or in part of chain branching/propagation reactions that can promote or postpone the onset of ignition. It was concluded in [54] that an error measure involving an integral measure of the distance between ignition trajectories in the $\{\psi, X_i\}$ phase space exhibits the sought-after monotonic convergent behavior with decreasing degree of simplification.

An appropriate progress variable $\psi(t)$ should provide a monotone and non singular mapping of time t versus ψ, so that all mappings involving the components X_i of the state X are one-to-one functions of ψ.

A progress variable is introduced, based on the mixture entropy change. The entropy per unit mass, s, of a mixture of N ideal gases is given by

$$s\left(T, p, Y_j\right) = \frac{S\left(T, p, X_j\right)}{\overline{W}}, \tag{4.1.4}$$

where $S\left(T, p, X_j\right)$ has been already defined in section (entropy participation indices). As already observed, this mixture entropy can change because of both external and internal irreversible processes, that is:

$$dS = dS_{ext} + dS_{int}, \tag{4.1.5}$$

where dS_{ext} accounts for heat exchange with the surroundings and the entropy change due to internal processes dS_{int} is evaluated according to the following differential relation:

$$dS_{int} = -\frac{1}{T}\sum_{j=1}^{N_s} \mu_j dX_j. \tag{4.1.6}$$

In isolated systems, where there is no interaction at all with the surroundings, $dS_{ext} = 0$ and the overall entropy production is due to dS_{int}, whereas the presence of heat exchange, even if the system is closed (no mass exchange), makes the term dS_{ext} different from zero. Furthermore, it can be proved that s_{int} is monotone and attains a maximum at equilibrium, making it a suitable progress variable. Thus, $\hat{s}(t)$ is defined as:

$$\hat{s}(t) := \int_0^t ds_{int}, \tag{4.1.7}$$

where s is the mixture entropy per unit mass and ds_{int} is the mixture entropy change due to internal processes.

Next, $\hat{s}(t)$ is scaled to get:

$$\tilde{s}(t) := \frac{\hat{s}(t) - \hat{s}(0)}{\hat{s}(t_{final}) - \hat{s}(0)}. \tag{4.1.8}$$

Trajectory errors in the $\{\psi, X_i\}$ space are usually obtained as integral measures of the distance between the predictions from the detailed and simplified models, such as:

$$E(X_i) = \int_0^1 \left| \frac{X_i(\tilde{s}) - X_i^d(\tilde{s})}{X_i^d(\tilde{s})} \right| d\tilde{s} \qquad i = 1, ..., N+1 \tag{4.1.9}$$

Lastly, discrepancies in equilibrium composition/temperature may be measured by relative errors such as:

$$E_{eq}(X_i) = \frac{X_i(t_{final}) - X_i^d(t_{final})}{X_i^d(t_{final})} \qquad i = 1, ..., N+1 \tag{4.1.10}$$

Errors on target species are expected to be much smaller than those on all the other species, given that the skeletal mechanism is tailored on the target species only.
Usually, the species trajectory and equilibrium errors are averaged over the target species, in order to get a single observable. As an example, the trajectory error often employed in the performance assessment is defined as:

$$E_{tgt} = \frac{\sum_{i=1}^{N_{tgt}} E(X_i)}{N_{tgt}} \tag{4.1.11}$$

The three error measures defined above are capable of characterizing the performance of a given simplified mechanism, with respect to the detailed one, when employed in the same ignition problem. However, it may happen that the three error figures are not consistent

with each-other, or that the user is not interested in all of them. An objective function may be introduced that weighs the three performance figures, based on the user desire, in order to get a single performance observable.

4.2 Improving the CSP skeletal algorithm

Most of the simplification algorithms, such as those based on computational singular perturbation (§ 4.1.1) or directed relation graph (DRG) [18], require the specification of the system's variables that the skeletal mechanism is desired to accurately predict. This set of variables, usually referred to as *target species* set, often includes temperature and the major species, such as fuel(s), oxidizer(s) and the main products, and those species the investigator/user is interested in, in the context of his/her application. As an example, typical species that are included beyond reactants and products are NOx or PAHs. The algorithm, consequently, will start its loop by inspecting the importance indices related to those variables. However, global observables such as ignition delay time or equilibrium state cannot be assumed as target variables, the reason being they are not system's state variables and can be evaluated only *a posteriori*, after a realization of the system's evolution becomes available.

Additional target species could be species known to be important for the ignition-delay-time-related dynamics, such as HCO, which is a marker for heat release and has been profitably used in methane skeletal mechanism generation. This practice, even though successful in most of the cases, requires a knowledge of the chemical pathways that typically are required for retaining accuracy in ignition delay time predictions. This knowledge, however, may be absent, being the chemical problem under study too complex to be fully understood.

The specification of the set of target species in general is a delicate matter. It is expected that the resulting skeletal mechanisms have a strong dependence on the target set, which acts as a seed for the mechanisms construction. Indeed, the more target species are specified in this set, the more species/reactions will be required in the skeletal mechanisms to obtain an accurate replication of them all. It follows that, if the user is interested in

global observables, such as ignition delay time, the choice of the target species is not trivial at all. The idea is that there exists an optimum target species set that allows to capture the core kinetics of, say, an ignition problem, with the minimum number of retained species/reactions. This optimum set has always been thought of as the aforementioned group of reactants, products and ignition-delay-related species. However, even if the latter are known, this set may be redundant, causing the inclusion of a higher-than-needed number of species/reactions in the skeletal mechanisms, with the possibility of even deteriorate the accuracy in ignition delay time, which is known to exhibit non-monotonic convergent behavior with increasing number of species/reactions of the skeletal kinetic mechanism. This non-monotonicity comes about as a consequence of the elimination in total or in part of chain branching/propagation reactions that can promote or postpone the onset of ignition [54], especially when ignition-delay-related processes are not correctly targeted by the user.

To summarize, when the user is interested in elevated accuracy in global observables, such as ignition delay time, the specification of the target species (which ones and how many) brings in a considerable number of degrees of freedom, which the user may not be aware of, or is not able to cope with. In this work, two modifications to the CSP simplification algorithm are proposed that aim at removing the need for a user-specified set of target species when global ignition observables are the targets of interest.

4.2.1 Using Entropy Participation Indices

The "Entropy Participation Indices", abbreviated as EPIs, presented in section 3.2, offer the possibility of substantially modifying the CSP skeletal algorithm, such that, as will be shown below, it does not need the specification of any target species. In fact, EPIs are able to select the reactions that are important to the entropy production. It can be imagined as if the target variable were effectively entropy itself. This version of the algorithm may be used to obtain skeletal mechanisms that capture the core kinetics of a combustion process, *i.e.* the dynamics that contribute the most to the entropy evolution, in both the fast and slow subspaces. Clearly, any additional features, such as accuracy in replicating secondary dynamics, e.g. NOx or PAHs, cannot be included, being missing the possibility of specifying

supplementary targets. It is expected, though, a substantial accuracy in global observables, with the minimum required number of retained species/reactions.

An approach based on an unprojected "Entropy Participation Index" is pursued in [55]. The motivations for a projected "Entropy Participation Index" are the same as those that are at the core of the CSP method and will not be repeated here.

Table 4.2 and Fig. 31 show the logical structure and the block diagram of the modified algorithmic procedure, where the user-specified input parameters are a training database of states D provided by any numerical time-integration of an ignition problem and the value of the tolerance threshold τ. It is important to stress again that the choice of the

For all $\mathbf{u}_n \in D$:

{ **Define active reactions set:**

$$R(\mathbf{u}_n, tol) = \{k : (EPI_k(\mathbf{u}_n))_{slow} > tol\} \quad \cup$$
$$\{k : (EPI_k(\mathbf{u}_n))_{fast} > tol\};$$

Define active species set:

$$S(\mathbf{u}_n, tol) = \{i : \nu_{ik} \neq 0; k \in R(\mathbf{u}_n, tol)\};$$

};

Define global active reactions set: $R(tol) = \bigcup_{n\in[1,N_{sol}]} R(\mathbf{u}_n, tol)$;

Define global active species set: $S(tol) = \{i : \nu_{ik} \neq 0; k \in R(tol)\}$.

Table 4.2: Structure of the simplification algorithm modified with EPIs

most appropriate training database is crucial to get satisfying results in terms of accuracy and degree of simplification. The user who is interested in capturing global observables should start the simplification campaign on as simple as possible problems, *i.e.* stoichiometric mixtures, at significant pressure and initial temperature values, that should allow to capture the core kinetics. This approach is likely to assure good accuracy of the skeletal mechanisms in predicting ignition delay times also when employed in more complicated operating conditions, *e.g.* leaner/richer mixtures, higher/lower temperature/pressure, unless substantially different ignition mechanisms take place. As an example, the auto-ignition characteristics of the H_2-O_2-inert mixture change radically above and below a certain,

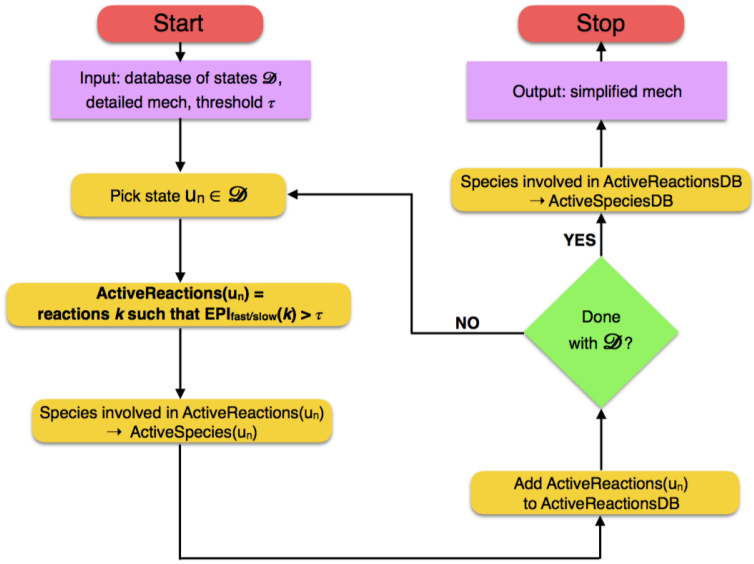

Figure 31: Block diagram of the simplification algorithm modified with EPIs

pressure dependent, initial ignition temperature ($\approx$ 950K at 1 atm). In this case, a comprehensive campaign should be done, *i.e.* using two autoignition solutions below/above the crossover temperature as training database, if one is interested in a skeletal mechanism valid throughout the whole temperature range.

4.2.2 Using Tangential Stretching Rate

The Tangential Stretching Rate (TSR) offers the possibility of removing any user-appointed degree of freedom related to the choice of the core kinetics target species, obtaining in practice a similar user experience to what the EPIs allow, although with a substantially different algorithmic procedure. Taking advantage of TSR and TSR Participation Indices, already defined in chapter 3, the algorithm automatically compute the most participating species at each time/space location to the TSR. This implies that the algorithm inspects the importance indices of a different set of species in different states of the dataset. In this way, the target set, which changes dynamically, is never redundant and forces the

algorithm to explore the truly active chemical pathways of each state.

Table 4.3 shows the logical structure of the TSR-modified algorithmic procedure, where the user-specified input parameters are a training database of states D provided by any numerical time-integration of an ignition problem and the value of the tolerance threshold τ. The TSR species are those involved in the TSR-participating reactions, which, in turn, are the reactions contributing substantially to the TSR-active modes.

For all $\mathbf{u}_n \in D$:

{ **Compute set of kernel species:**

$S_{[h=0]} = S_{\text{TSR}}(\mathbf{u}_n) = \{i : \nu_{ik} \neq 0; k \in R_{\text{TSR}}(\mathbf{u}_n)\}$;

While $\left[S_{[h]}(\mathbf{u}_n, tol, S_{\text{TSR}}(\mathbf{u}_n)) = S_{[h-1]}(\mathbf{u}_n, tol, S_{\text{TSR}}(\mathbf{u}_n))\right]$

{ $h = h + 1$;

Define new active reactions set:

$$R_{[h]}(\mathbf{u}_n, tol, S_{\text{TSR}}(\mathbf{u}_n)) = \{k : \left(I_k^i(\mathbf{u}_n)\right)_{slow} > tol; i \in S_{[h-1]}(\mathbf{u}_n, tol, S_{\text{TSR}}(\mathbf{u}_n))\} \cup \{k : \left(I_k^i(\mathbf{u}_n)\right)_{fast} > tol; i \in S^{rad}_{[h-1]}(\mathbf{u}_n, tol, S_{\text{TSR}}(\mathbf{u}_n))\};$$

Define new active species set:

$S_{[h]}(\mathbf{u}_n, tol, S_{\text{TSR}}(\mathbf{u}_n)) = \{i : \nu_{ik} \neq 0; k \in R_{[h]}(\mathbf{u}_n, tol, S_{\text{TSR}}(\mathbf{u}_n))\}$;

};

Define local active reactions set: $R_\ell(\mathbf{u}_n, tol, S_{\text{TSR}}(\mathbf{u}_n)) = R_{[h]}$;

};

Define global active reactions set: $R(tol) = \bigcup_{n\in[1,N_{sol}]} R_\ell(\mathbf{u}_n, tol, S_{\text{TSR}}(\mathbf{u}_n))$;

Define global active species set: $S(tol) = \{i : \nu_{ik} \neq 0; k \in R(tol)\}$.

Table 4.3: Structure of the simplification algorithm, modified with TSR species

Differently from the EPI modification, this version of the algorithm still relies on a target set of species. This set of species, although automatically computed in each state, may be constantly augmented by the user with other species he/she is interested in, allowing for the simultaneous inspection of secondary dynamics. Table 4.4 and Fig. 32 show the logical structure and block diagram of the TSR-modified algorithmic procedure, where the user-specified input parameters are a training database of states D provided by any numerical

time-integration of an ignition problem, the value of the tolerance threshold τ and the set S_0 of other target species, not related to the core kinetics. Again, the choice of the dataset

For all $\mathbf{u}_n \in D$:

{ **Compute set of kernel species:**

$S_{\text{TSR}}(\mathbf{u}_n) = \{i : \nu_{ik} \neq 0; k \in R_{\text{TSR}}(\mathbf{u}_n)\}$;

$S_{[h=0]} = S_{TSR}(\mathbf{u}_n) \cup S_0$;

While $\left[S_{[h]}(\mathbf{u}_n, tol, S_{\text{TSR}}(\mathbf{u}_n)) = S_{[h-1]}(\mathbf{u}_n, tol, S_0, S_{\text{TSR}}(\mathbf{u}_n))\right]$

{ $h = h + 1$;

Define new active reactions set:

$$R_{[h]}(\mathbf{u}_n, tol, S_0, S_{\text{TSR}}(\mathbf{u}_n)) = \{k : \left(I_k^i(\mathbf{u}_n)\right)_{slow} > tol; i \in S_{[h-1]}(\mathbf{u}_n, tol, S_0, S_{\text{TSR}}(\mathbf{u}_n))\} \cup \{k : \left(I_k^i(\mathbf{u}_n)\right)_{fast} > tol; i \in S^{rad}_{[h-1]}(\mathbf{u}_n, tol, S_0, S_{\text{TSR}}(\mathbf{u}_n))\};$$

Define new active species set:

$S_{[h]}(\mathbf{u}_n, tol, S_0, S_{\text{TSR}}(\mathbf{u}_n)) = \{i : \nu_{ik} \neq 0; k \in R_{[h]}(\mathbf{u}_n, tol, S_0, S_{\text{TSR}}(\mathbf{u}_n))\}$;

};

Define local active reactions set: $R_\ell(\mathbf{u}_n, tol, S_0, S_{\text{TSR}}(\mathbf{u}_n)) = R_{[h]}$;

};

Define global active reactions set: $R(tol, S_0) = \bigcup_{n\in[1,N_{sol}]} R_\ell(\mathbf{u}_n, tol, S_0, S_{\text{TSR}}(\mathbf{u}_n))$;

Define global active species set: $S(tol, S_0) = \{i : \nu_{ik} \neq 0; k \in R(tol)\}$.

Table 4.4: Structure of the simplification algorithm, modified with TSR species and additional user-defined kernel set

is delicate, especially when adding other target species. The solutions fed in the algorithm should exhibit the prototypical behaviors of the desired targets.

4.2.3 A variable tolerance approach for weighing the targets

Independently of the algorithm version, the threshold τ plays the pivotal role of the kinetic branches scissor. The retained reactions are those whose importance index to the production/consumption of a target species, or the participation to the entropy production in

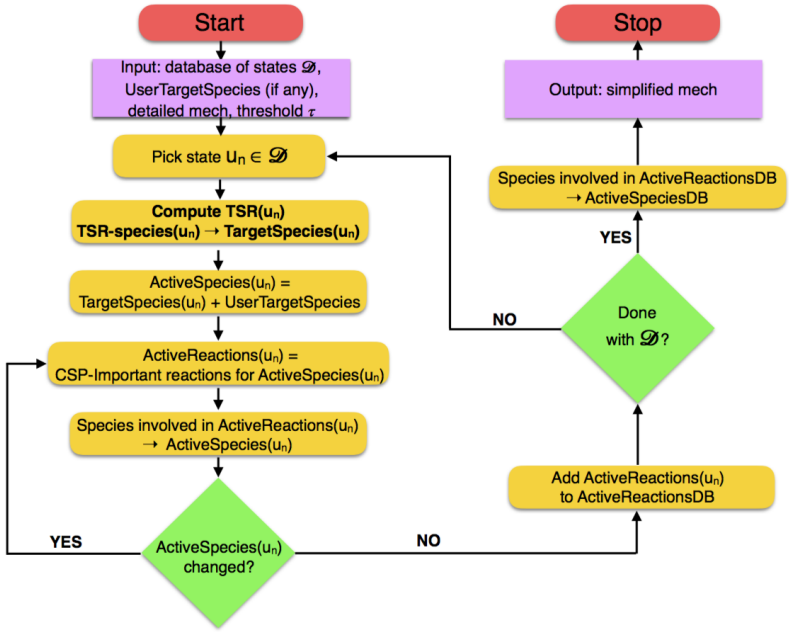

Figure 32: Block diagram of the simplification algorithm modified with TSR species and additional user-defined kernel set

the EPI-version, is larger than τ. However, the user may be interested in some features more than in others. As an example, a skeletal mechanism may be desired to accurately replicate a number of features, such as ignition delay time, or a particular set of major species, and to a less extent another set of species, that may be involved in secondary kinetic branches. Employing the same threshold τ for both the necessities, would mean giving them the same importance, and may induce the algorithm to include a large number of species/reactions involved in the second target, which is comparable to those included for the essential features. This will likely assure accuracy in both targets, if τ is sufficiently low, but at the cost of increasing the size of the skeletal mechanism.

A proposed solution for this problem is to employ different thresholds τ for different targets, allowing to tune the degree of accuracy of each specified target, in order to minimize the number of retained species. In practice, the simplification campaign is split in several

building blocks, each one with its own purpose and degree of accuracy, which are then assembled together.

Typically, the core kinetics is first captured by the EPI-version or the TSR-version of the algorithm, employed on a suitable training database of states, usually a stoichiometric auto-ignition. The best mechanism for the core kinetics, in terms of trade-off between desired accuracy in ignition delay time and/or equilibrium, and the number of retained species, is chosen a-posteriori among the family of skeletal mechanisms obtained varying the τ threshold. Then, if additional features are required, the classic or the TSR-version of the algorithm are employed on a training database of states representative of the sought-after behavior, for example a rich mixture auto-ignition for soot formation, with the specification of the desired target species. The resulting family of skeletal mechanisms is then merged to the primary mechanism, previously chosen, and the performance are checked a-posteriori, this time of course the additional features will also be kept under consideration. The final mechanism, typically, results from the union of two mechanisms generated with different targets and different τ thresholds. It is good practice, also, to have the secondary mechanism being self-contained, even though less accurate on the global observables, such as ignition delay time. This normally assures the preservation of the pathways that connect the core kinetics to the secondary observables.

4.3 A simplification test-case

The KAUST-Aramco PAH Mech 1.0, based on the comprehensively validated AramcoMech 1.3 C_0–C_2 chemistry developed by NUIG [34], accounts for reactions involving aromatics larger than benzene (C_6H_6 or A1) by including PAH growth pathways up to coronene, for the prediction of soot formation. The base mechanism contains accurate chemical kinetics for the combustion of saturated and unsaturated hydrocarbons, namely methane, ethane, ethylene, and acetylene, as well as oxygenated species, such as formaldehyde, methanol, acetaldehyde, and ethanol. The detailed KAUST-Aramco PAH Mech 1.0 contains 397 species and 2346 reactions. This mechanism has already been reduced to 99 species in [56] using directed relation graph with expert knowledge (DRG-X) [57], in which the DRG

method is extended allowing for expert-specified species-specific error tolerances, and DRG-aided sensitivity analysis (DRGASA) [58], which eliminates species that have minor effects on the major species and global parameters by eliminating one species at a time.

The improved CSP-based skeletal algorithms are tested on a simplification campaign involving homogeneous auto-ignition problems of ethylene (C_2H_4) - air mixtures. This campaign focuses on the replication of global observables, *i.e.* ignition delay times and equilibrium states, in a range of initial temperature (900 - 1500 K), pressure (0.1 - 10 atm) and equivalence ratio (0.5 -5). The aim of this campaign is to identify the best skeletal mechanism, whose trade-off between accuracy and degree of simplification is considered satisfactory over the whole range of operating conditions.

The CSP classic, the EPI-modified and the TSR-modified skeletal algorithm will be employed and compared. At this stage, PAH species are not targeted, for two main reasons: (i) the focus is on the core kinetics, (ii) the EPI-modified skeletal algorithm does not allow to do it, preventing comparisons between the two algorithms. PAH species will be added in a second stage, where also the variable tolerance approach will be exploited.

4.3.1 A single-operating-condition simplification for core kinetics

The first step of the simplification campaign usually consists of a single point analysis. The chosen operating condition for the constant pressure homogeneous reactor is: T = 900 K, $\phi = 1.0$ and p = 1 atm.

Classic CSP algorithm

The target species set for the classic CSP algorithm includes: temperature, C_2H_4, O_2,H_2O and CO_2, following the basic rule of thumb that suggest to include reactants and main products.

The detailed mechanism is thus employed to generate a time trajectory, which is employed as dataset and fed in the CSP skeletal algorithm, together with a set of increasing thresholds τ, each of which allows to obtain a simplified mechanism with a certain degree of simplification.

Figure 33 shows the outcomes of the three employed error measures, defined in section 4.1.3, that assess the ability of the skeletal mechanism to replicate, in the same operating condition adopted for the detailed mechanism, ignition delay time, target species evolution and target species equilibrium state.

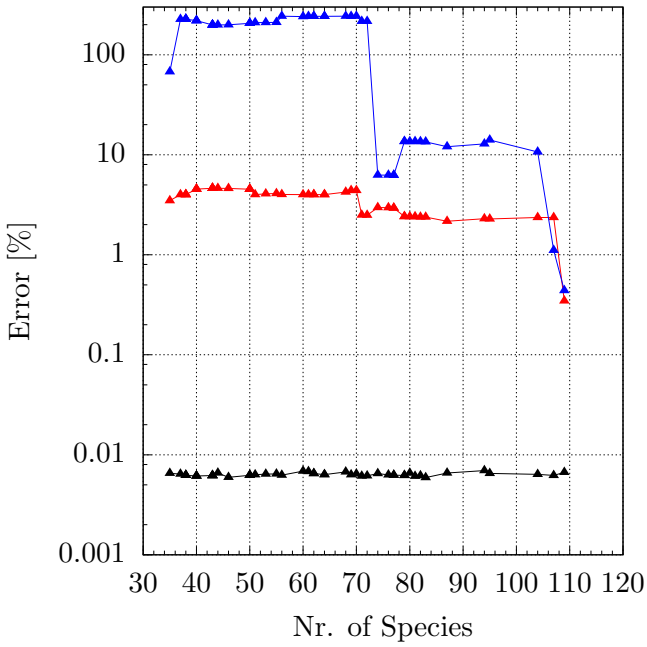

Figure 33: Errors in ignition delay time (blue symbols), target species evolution (red symbols) and target species equilibrium state (black symbols) versus number of retained species, with CSP skeletal algorithm

The error on target species equilibrium state (black symbols) is almost negligible and is not sensitive to the degree of simplification. This is presumably the consequence of: (i) the absence of complexity in the kinetics when the system approaches equilibrium, (ii) the ability of the algorithm to include all the necessary species/reactions when targeting the main products. Moreover, it appears that ∼30 species are enough to capture equilibrium composition, and adding species does not improve the accuracy.

The errors on target species evolution (red symbols), measured as per Eq.(4.1.11),

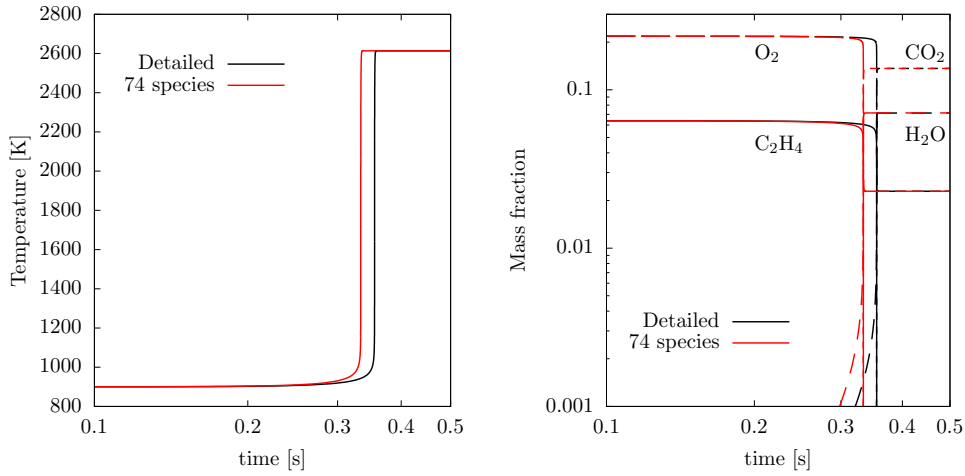

(a) Temperature

(b) Target species

Figure 34: Comparison between detailed and simplified (74 species) mechanism in a C_2H_4-air auto-ignition at stoichiometric conditions, 900 K, 1 atm

increase with the degree of simplification, but are well bounded below 5%, which is a remarkable performance figure. The same cannot be said of the errors on ignition delay time (blue symbols). They reach ∼10% around 105 species, then jump above 100% below 70 species. The reason for this poor performance is the absence of ignition-delay-related species in the target set, associated with high complexity in the chemical kinetics of the process. A tedious work that can be done to improve these error figures is to look for other species which appear to be important in the ignition process and target them. This approach, however, may end up nowhere, with a considerable waste of time.

In conclusion, the single-point simplification campaign with the classic CSP skeletal algorithm allowed to obtain a 74-species mechanism with acceptable accuracy performance in the three error figures simultaneously. Figure 34 shows a comparison between this skeletal mechanism and the 397-species detailed mechanism in terms of temperature and target species evolution.

EPI-modified algorithm

The same test-case is processed resorting to the entropy participation indices (EPIs) - modified algorithm. As already stated, this procedure does not allow to specify any target species, being entropy production the target of the algorithm. Figure 35 shows the errors in ignition delay time, target species evolution and target species equilibrium state of the obtained skeletal mechanisms. Clearly, being absent the target species set, the errors calculations have been done considering the same species of the previous test-case, namely C_2H_4, O_2,H_2O and CO_2, together with temperature.

Errors on equilibrium state are again very small and insensitive to the number of species. Errors on species evolution are comparable to the previous case, being lower in the 90-110-species region and slightly lower in the rest of the species range. The real breakthrough, though, is in the ignition delay time errors, which are more than one order of magnitude smaller than in the previous case. In particular, they are bounded below 10% throughout the whole species range. Hence, even mechanisms as small as 40 species have acceptable figures of merit in all the three error measures.

Figure 36 shows the comparison between the detailed mechanism and the 40-species mechanism here obtained.

TSR-modified algorithm

Finally, the same test-case is processed using this time the TSR-modified algorithm. The choice of the kernel set, which becomes dynamic in this version of the algorithm, is left to the algorithm itself, without adding any other user-defined species. Figure 37 shows the error figures computed with the so obtained skeletal mechanisms. At first sight, this plot appears slightly different from the corresponding ones of the previous cases: there are less points, *i.e.* less skeletal mechanisms, even though the same number of τ thresholds has been used. This means that the same mechanisms are chosen across intervals of τ, then a jump in the number of species/reactions occurs at certain values. Also, the errors behavior against the degree of simplification is much more bumpy and less monotone than observed in the previous cases, exception made for the errors in the equilibrium state, which remains constantly of the order of 0.01%.

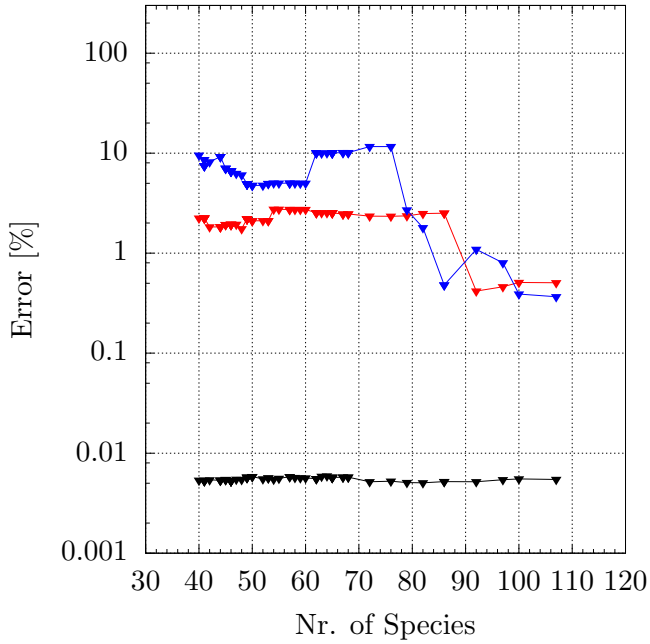

Figure 35: Errors in ignition delay time (blue symbols), target species evolution (red symbols) and target species equilibrium state (black symbols) versus number of retained species, with EPI-modified CSP skeletal algorithm

However, the plot suggests that the use of the TSR-modified algorithm in this application gives a dramatic improvement to the error figures: errors in ignition delay time remain bounded below 4% and there is even an outperformer, a small mechanism with 36 species, whose error in ignition delay is $\sim 0.1\%$. Nonetheless, also the errors on the reference species are improved, being below 1% until ~ 50 species, than slightly raising to 4%. Figure 38 shows the time evolution of the 36-species skeletal mechanism, which is almost superimposed to the detailed solution. The same degree of accuracy can be observed in Fig.39, where the trajectories against entropy of the main species are depicted.

More insights on the algorithm behavior may be provided by table 4.5, which shows the kernel set of species that is dynamically identified along the time trajectory. Even

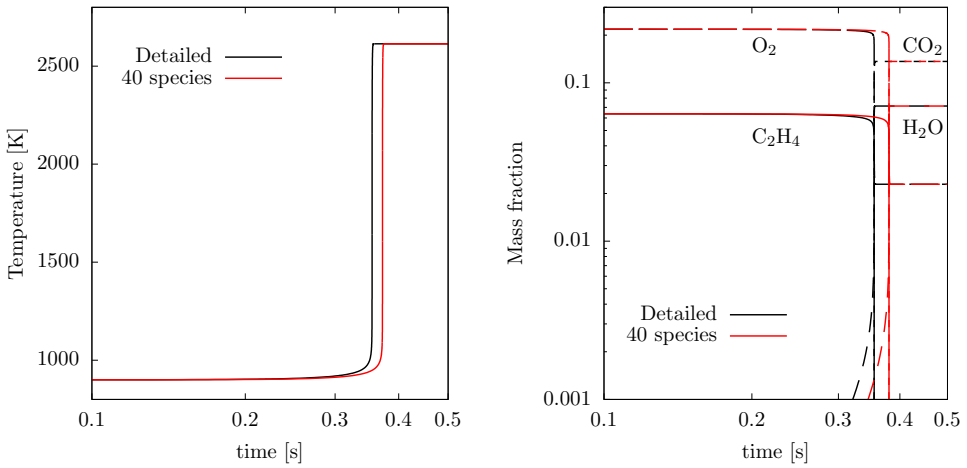

(a) Temperature

(b) Major species

Figure 36: Comparison between detailed and EPI-simplified (40 species) mechanism in a C_2H_4-air auto-ignition at stoichiometric conditions, 900 K, 1 atm

though the identification of the kernel set is local, *i.e.* it is done on each sampled point of the trajectory, which are more than 400 in this application, it was possible to distinguish 11 regions where the kernel set did not change appreciably or did not change at all. The species selected by TSR are indeed those typically involved in the ethylene oxidation[59]. In particular, in the first regions, it is worth to note the presence of the vinyl radical (C_2H_3) and the vinylidene (H_2CC) which are involved in the initiation reactions:

$$C_2H_4 + M \longleftrightarrow H_2 + H_2CC + M$$

$$C_2H_4 + O_2 \longleftrightarrow C_2H_3 + HO_2$$

Also, formaldehyde (CH_2O) and the formyl radical (HCO) are typically produced by the addition reactions:

$$C_2H_4 + O \longleftrightarrow CH_3 + HCO$$

$$C_2H_4 + O \longleftrightarrow CH_2O + CH_2$$

$$C_2H_3 + O_2 \longleftrightarrow CH_2O + HCO$$

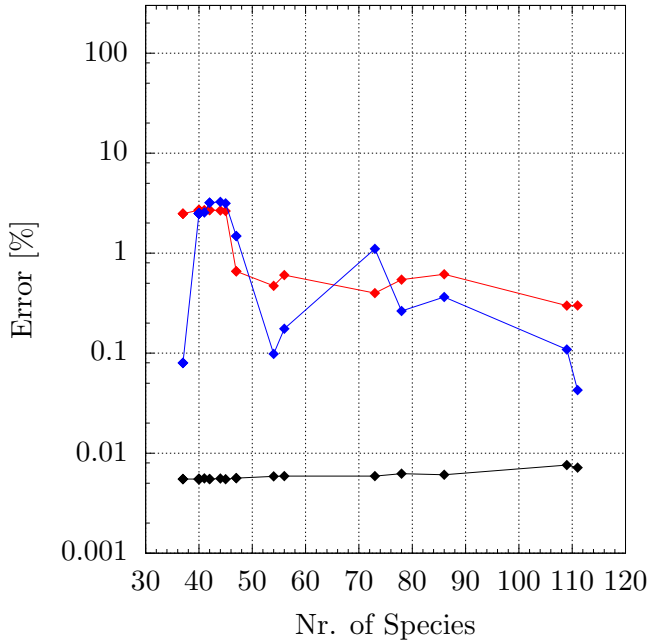

Figure 37: Errors in ignition delay time (blue symbols), target species evolution (red symbols) and target species equilibrium state (black symbols) versus number of retained species, with TSR-modified CSP skeletal algorithm

Further, the vinoxy radical (CH_2CHO) is one of the major intermediate during ethylene oxidation, produced by the reaction between vinyl and molecular oxygen:

$$C_2H_3 + O_2 \longleftrightarrow CH_2CHO + O$$

Indeed, TSR is able to automatically identify these species and use them as targets in the trajectory regions where it is reasonable to explore their kinetics, without any previous knowledge of the combustion process under study. Clearly, this feature becomes especially useful when dealing with new fuels, such as bio-fuels, synthetic fuels and surrogate fuels.

In summary, the comparison of the three versions of the CSP skeletal algorithms shows that, in this test-case, which consists in the simplification of a complex kinetic mechanism employed for ethylene oxidation, the TSR-modified version gives the best skeletal mech-

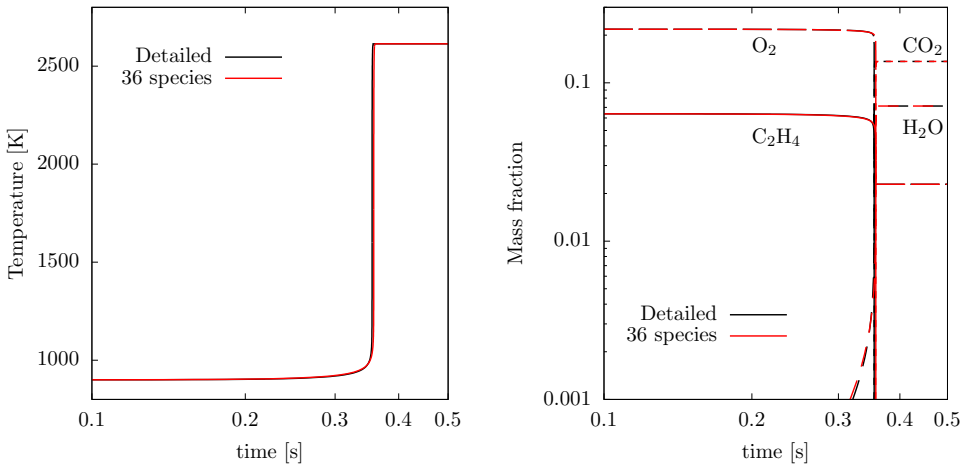

(a) Temperature

(b) Major species

Figure 38: Comparison between detailed and TSR-simplified (36 species) mechanism in a C_2H_4-air auto-ignition. Temperature and species time evolution, at stoichiometric conditions, 900 K, 1 atm

anisms in terms of error figures on both ignition delay time, main species evolution and equilibrium state. Figure 40 shows a direct comparison of the errors in ignition delay time already showed in Figs. 34, 36 and 38.

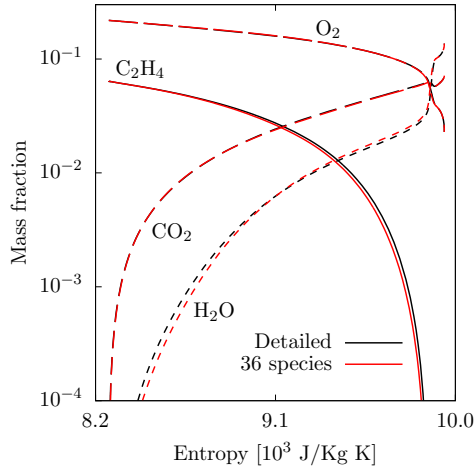

Figure 39: Comparison between detailed and TSR-simplified (36 species) mechanism in a C_2H_4-air auto-ignition. Species evolution against entropy, at stoichiometric conditions, 900 K, 1 atm

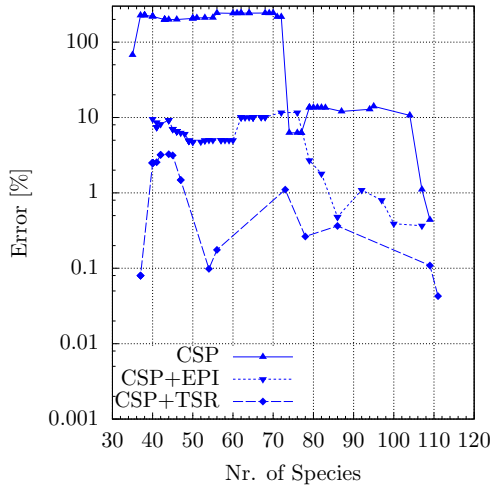

Figure 40: Errors in ignition delay time of the families of skeletal mechanisms obtained with classic (delta symbols with solid line), EPI-modified (gradient symbol with dotted line) and TSR-modified (diamond symbols with dashed line), CSP-algorithm

Table 4.5: TSR kernel species identified by regions

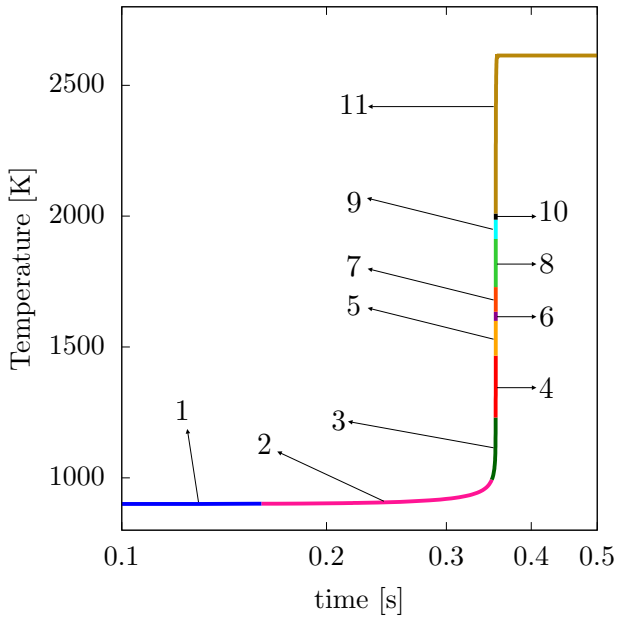

Region #	Temperature [K]	TSR kernel set
1	900 - 901	O, O_2, CH_2O, HCO, C_2H_3, H_2CC, CH_2CHO
2	901 - 985	O, O_2, OH, H_2O_2, CH_2O, HCO, C_2H_3, CH_2CHO
3	985 - 1210	O, O_2, OH, H_2O, H_2O_2, C_2H_4, C_2H_3, CH_2CHO
4	1210 - 1460	H, O, O_2, OH, H_2O, C_2H_4, C_2H_3, CH_2CHO
5	1460 - 1580	H, H_2, O, O_2, OH, CH_2O, HCO, C_2H_3, CH_2CHO
6	1580 - 1620	H, O, O_2, OH, CO, HCO, C_2H_3, CH_2CHO
7	1620 - 1680	H, H_2, O, O_2, OH, H_2O, CO, HCO
8	1680 - 1892	H, H_2, O, O_2, OH, H_2O, CH_4, CH_3, CH_2O, C_2H_4, C_2H_3
9	1892 - 1976	H, H_2, O, O_2, OH, H_2O, C_2H_2, HCCO
10	1976 - 2000	H, H_2, O, O_2, OH, H_2O, CO, CO_2
11	2000 - 2614	H, H_2, O, O_2, OH, H_2O, HO_2, CO, CO_2

4.3.2 A comprehensive skeletal mechanism with TSR

The focus of this section is to obtain a "comprehensive" skeletal mechanism which will be accurate in a range of initial temperatures (900 - 1500 K), pressure (0.1 - 10 atm) and equivalence ratio (0.5 -5). The performance validation, once more, is carried out on the basis of the simultaneous observation of the three error measures on ignition delay, equilibrium and species evolution. The employed algorithm is the TSR-modified version, which proved to generate the best skeletal mechanisms for this application test-case.
As a first step, the skeletal mechanisms obtained in the single-operating-condition case are validated over the whole range of temperature, pressure and equivalence ratio. The smallest mechanism providing satisfactory accuracy is the TSR-simplified 39-species mechanism, obtained with τ=0.5. It will be referred to as the "core-mechanism". Figure 41 shows a comparison of the ignition delay times predicted by the 39-species skeletal mechanism against the detailed mechanism. Surprisingly, a very good agreement can be observed throughout the whole operating range. This might be a combined consequence of (i) the remarkable job made by the TSR-modified algorithm in capturing the core kinetics of the ethylene oxidation, (ii) the rather low sensitivity of the oxidation kinetics to the operating conditions in the chosen intervals. This may indicate that the worst case scenario for the ignition kinetics in terms of complexity is indeed 900 K, which was employed for the training dataset generation, allowing in turn to correctly capture ignition delay times also in the high temperature cases.

On the other hand, the performance is not equally satisfactory for what concerns the errors on equilibrium temperature and composition of the rich mixture case ($\phi = 5$). Figure 42 shows the equilibrium temperatures obtained with the detailed and simplified mechanism, where, although the accuracy at ϕ equal to 0.5 and 1 is high, substantial discrepancies can be observed at $\phi = 5$. This result could be expected since the analyzed dataset refers to stoichiometric conditions: the whole rich chemistry is not involved in the training database and, as a consequence, is also not included in the skeletal mechanisms. Figure 43 shows a comparison of the time evolution of temperature and major species as predicted by the detailed mechanism and the 39-species skeletal mechanism for the {T=900K, p=1 atm, ϕ=5} auto-ignition case. There are large discrepancies in both the time behavior and the

equilibrium mass fractions. Indeed, other major species that become abundant in the rich cases, such as anthan, are not even present in the skeletal mechanisms, for the reason discussed here above.

4.3.3 Adding rich chemistry

For the purpose of improving the error figures at rich operating conditions, a new training database of states is generated with the detailed mechanism for a set of ϕ=5 auto-ignition problems at the different pressure values of 0.1 and 10 atm. The choice of two different pressure values for the rich dataset is motivated by an observed strong sensitivity of the important reactions upon pressure in the rich cases.

The final mechanisms will be the union of the 39-species "core" mechanism and the mechanisms resulting from this new campaign on a rich auto-ignition training database. The expectation is to generate mechanisms which are able to capture ignition delays, equilibrium composition and main species evolution in the whole operating conditions range. This comprehensive campaign allowed to obtain a family of skeletal mechanisms, referred to as "rich-submechanisms". The smaller mechanism which preserves the performance of the 39-species on ignition delays, and achieves sufficient accuracy in the equilibrium and species evolution figures in the rich cases, has 90 species and results from the union of a rich-submechanism obtained with τ=0.54 on the rich dataset and the 39-species core-mechanism. Essentially, the additional capability of replicating the rich kinetics in the dissipative region of the auto-ignition requires to double the number of retained species, given the complexity of the activated detailed kinetics in such cases. The detailed mechanism, in fact, is designed to describe soot precursors and PAHs growth, up to coronene. Indeed, in the analyzed rich cases, the species selected by TSR and included in the kernel set are those typical of the chemical pathways leading to PAHs formation, such as the H-abstraction reaction responsible for benzene (A1) formation:

$$\text{n-}C_4H_5 + C_2H_2 \longleftrightarrow A1 + H$$

or reactions involving species with odd-carbon number such as indene (C_9H_8), benzyl

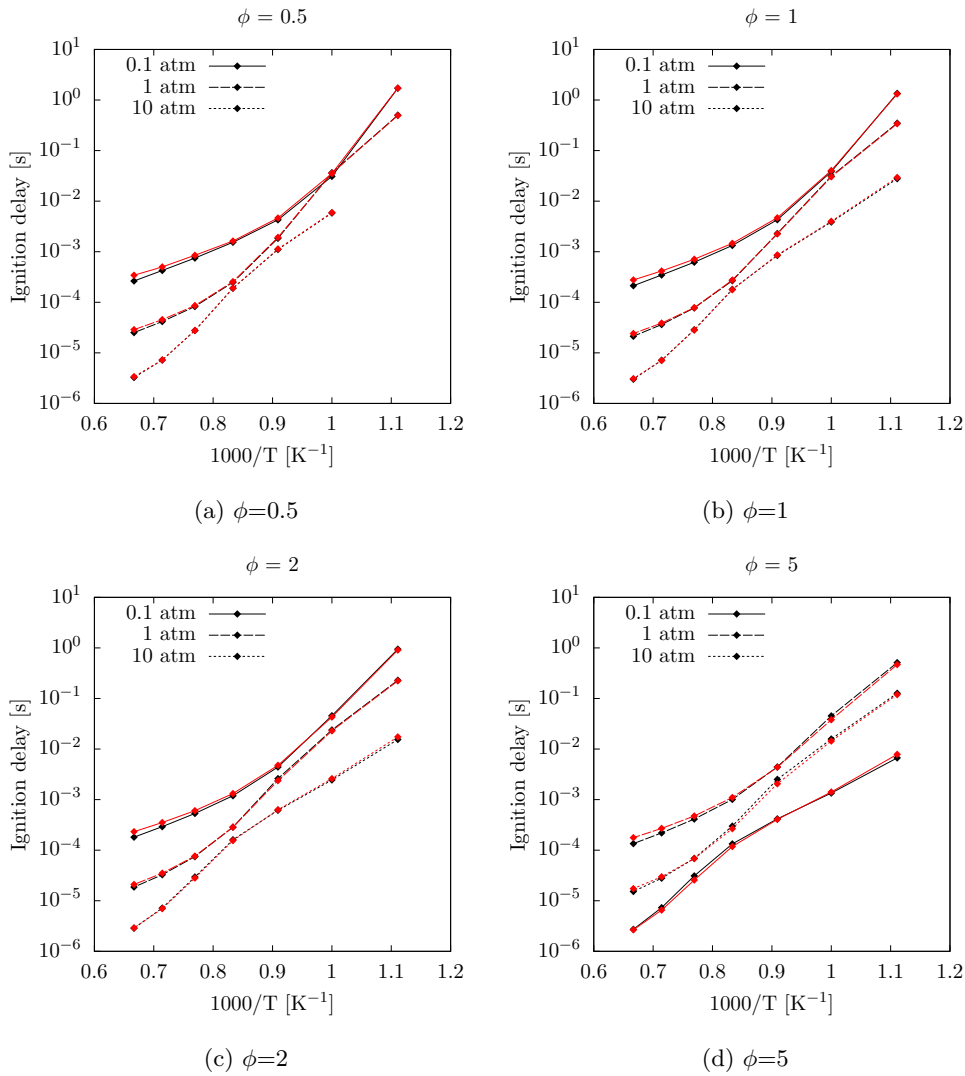

(a) ϕ=0.5 (b) ϕ=1

(c) ϕ=2 (d) ϕ=5

Figure 41: Comparison of ignition delay times in a range of temperature, pressure and equivalence ratio between detailed (black) and TSR-simplified (39 species, red) mechanism in a C_2H_4-air auto-ignition

($C_6H_5CH_2$) and C_5H_5:

$$C_6H_5CH_2 + C_2H_2 \longleftrightarrow C_9H_8 + H$$

$$C_6H_5CH_2 \longleftrightarrow c\text{-}C_5H_5 + C_2H_2$$

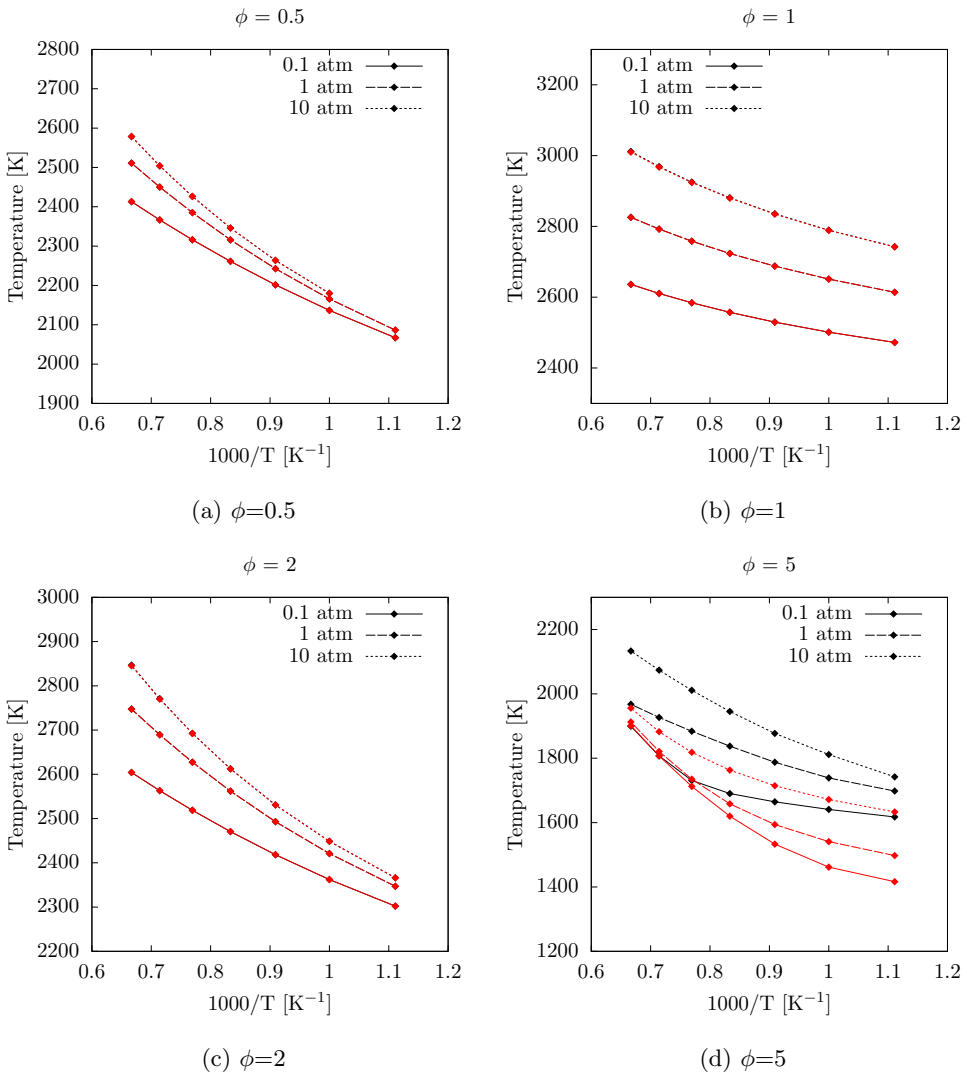

(a) ϕ=0.5 (b) ϕ=1

(c) ϕ=2 (d) ϕ=5

Figure 42: Comparison of equilibrium temperature in a range of temperature, pressure and equivalence ratio between detailed (black) and TSR-simplified (39 species, red) mechanism in a C_2H_4-air auto-ignition

Figures 44 and 45 show ignition delays and equilibrium temperature in the entire range of operating conditions. In particular, large improvements are visible in the equilibrium

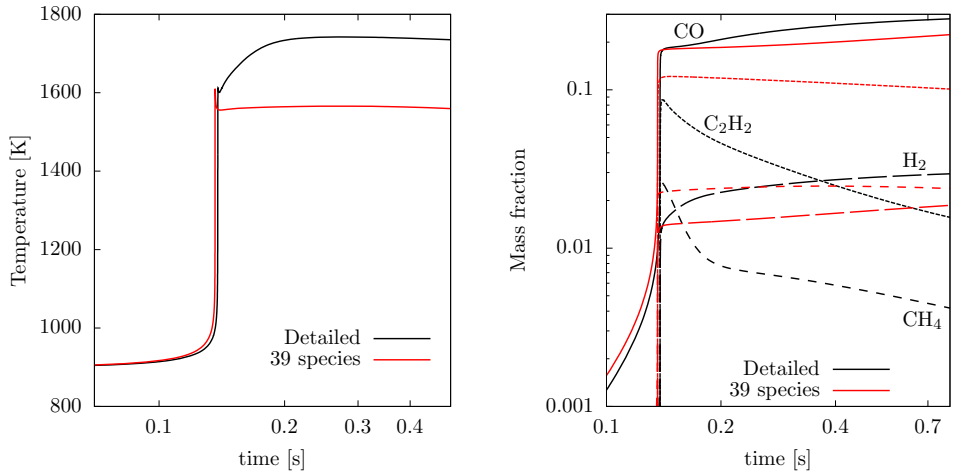

(a) Temperature

(b) Major species

Figure 43: Comparison between detailed and TSR-simplified (39 species) mechanism in a C_2H_4-air auto-ignition. Temperature and major species time evolution in the case of T=900K, p=1 atm, ϕ=5

temperature of the ϕ=5 cases. Figure 46 shows the time evolution of temperature and major species in the T=900K, p=1 atm, ϕ=5 case, which, compared to the 39-species mechanism depicted in Fig. 43, reveals the improvements brought by the 90-species mechanism.

4.3.4 An eye on large PAHs

As already stated at the beginning of § 4.3, the detailed KAUST-Aramco PAH Mech 1.0 accounts for reactions involving aromatics larger than benzene (C_6H_6 or A1) by including PAH growth pathways up to coronene, for the prediction of soot formation. Hence, it is surely worth to include as targets also species which play a role in soot formation, such as naphtalene (A2), pyrene (A4) and coronene (A7). These species are largely present in the ϕ=5 cases whose database of states has already been analyzed for the generation of the comprehensive skeletal mechanisms. In order to demand the inclusion of their relevant kinetics, the aforementioned species are systematically added to the TSR-selected target set, exploiting the advantage of the TSR-modified algorithm shown in table 4.4. The

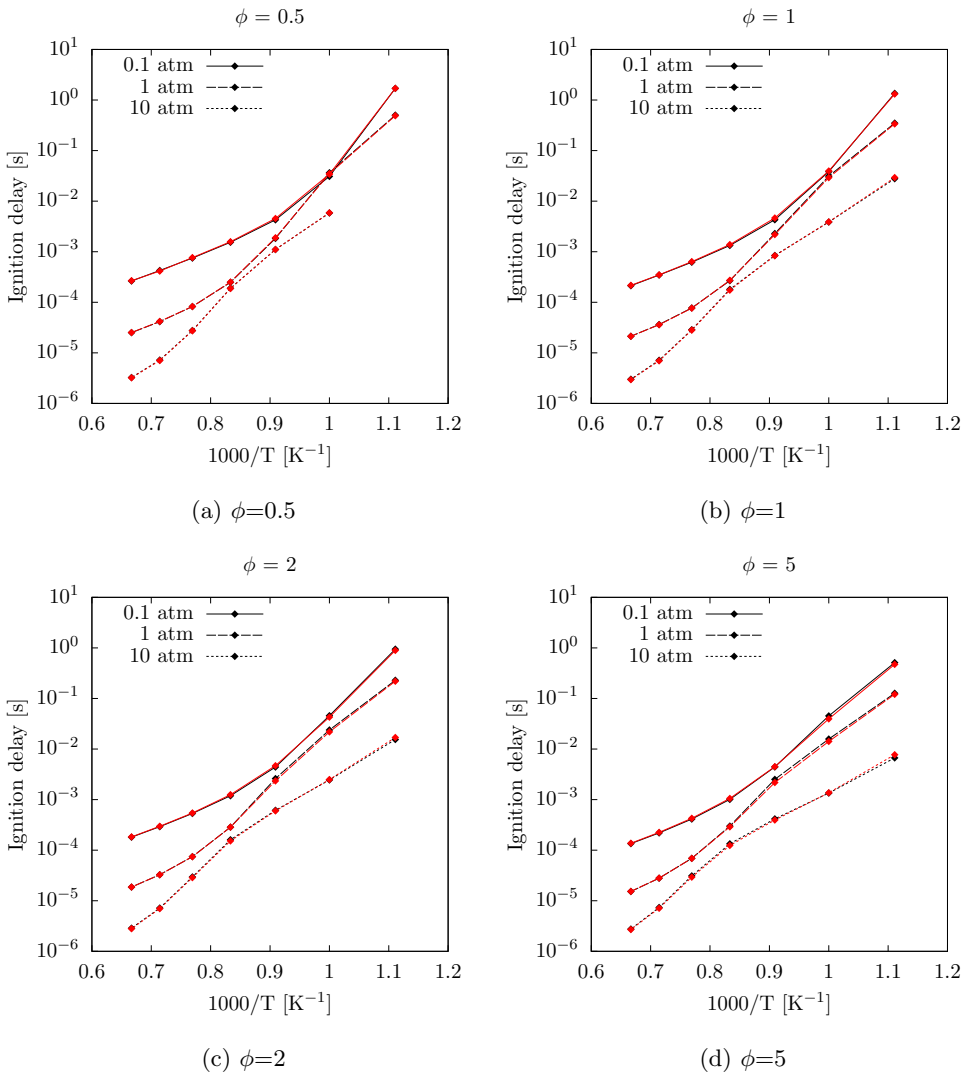

(a) ϕ=0.5 (b) ϕ=1

(c) ϕ=2 (d) ϕ=5

Figure 44: Comparison of ignition delay times in a range of temperature, pressure and equivalence ratio between detailed (black) and TSR-simplified (90 species, red) mechanism in a C_2H_4-air auto-ignition

resulting family of skeletal mechanisms, referred to as "PAH-submechanisms", obtained with a range of τ values, is then merged to the 90-species mechanism of section 4.3.3. The

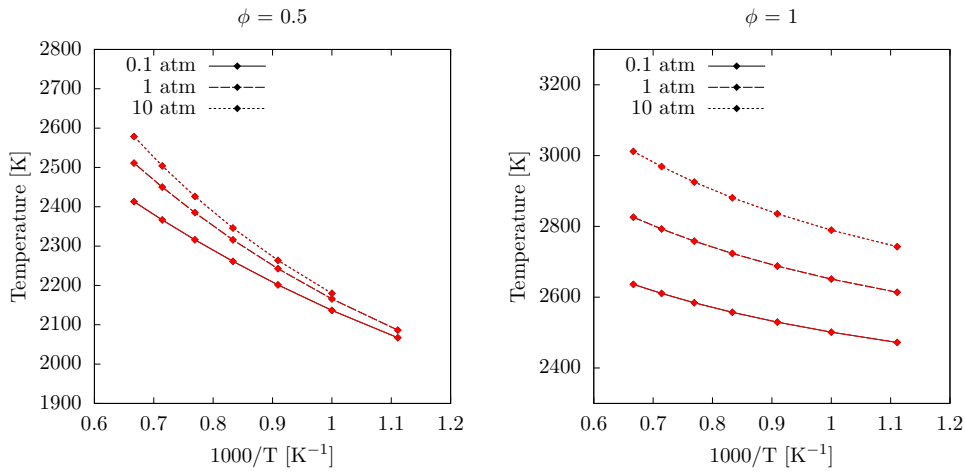

(a) ϕ=0.5

(b) ϕ=1

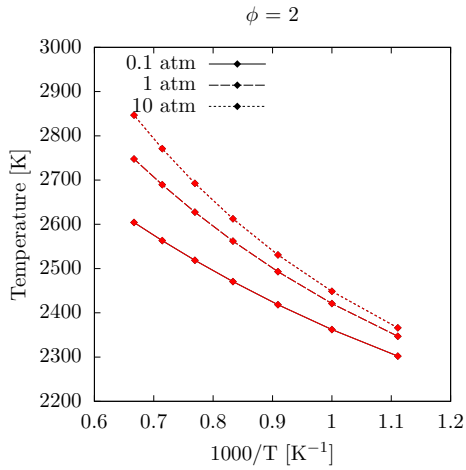

(c) ϕ=2

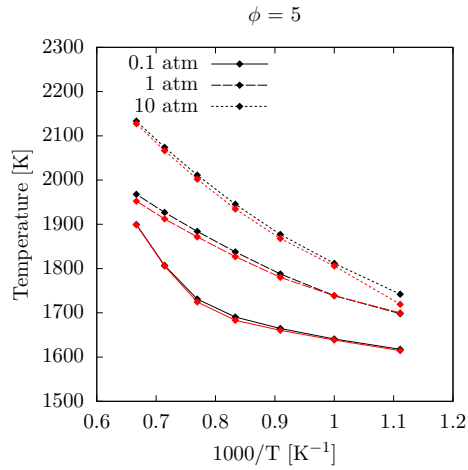

(d) ϕ=5

Figure 45: Comparison of equilibrium temperature in a range of temperature, pressure and equivalence ratio between detailed (black) and TSR-simplified (90 species, red) mechanism in a C_2H_4-air auto-ignition

best compromise between number of species and accuracy in the added target species is a 109-species mechanism, whose "PAH-submechanism" is obtained with τ=0.99. Ignition

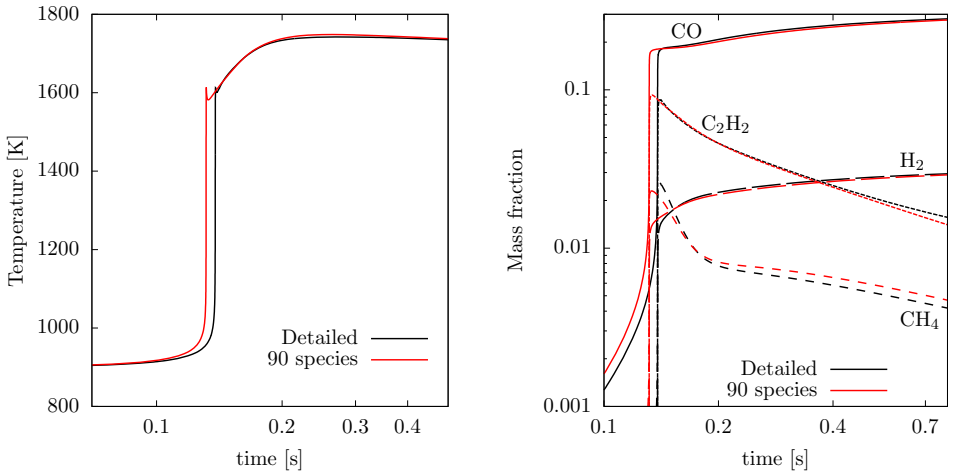

(a) Temperature

(b) Major species

Figure 46: Comparison between detailed and TSR-simplified (90 species) mechanism in a C_2H_4-air auto-ignition. Temperature and major species time evolution in the case of T=900K, p=1 atm, ϕ=5

delays and equilibrium temperature are essentially identical to those obtained with the 90-species mechanisms and are not shown. Figure 47, instead, shows the time evolution of A1, A2, A4 and A7, which exhibit an acceptable degree of fidelity to the detailed-mechanism-generated time evolutions.

In summary, when the replication of global ignition characteristics is the focus of a mechanism simplification strategy, the specification of a target species set becomes non-trivial, especially when dealing with complex detailed mechanisms. Two modification of the CSP simplification algorithm, presented in § 4.1.1, are proposed: the first relying on entropy participation indices, which allow to retain in the skeletal mechanism the reactions (and species) contributing to entropy production, the second relying on an automatic and dynamic target species set identification, which becomes possible thanks to the participation indices to the tangential stretching rate (TSR), which identify the reactions most contributing to the TSR.

A 90-species comprehensive skeletal mechanism for ethylene oxidation was obtained

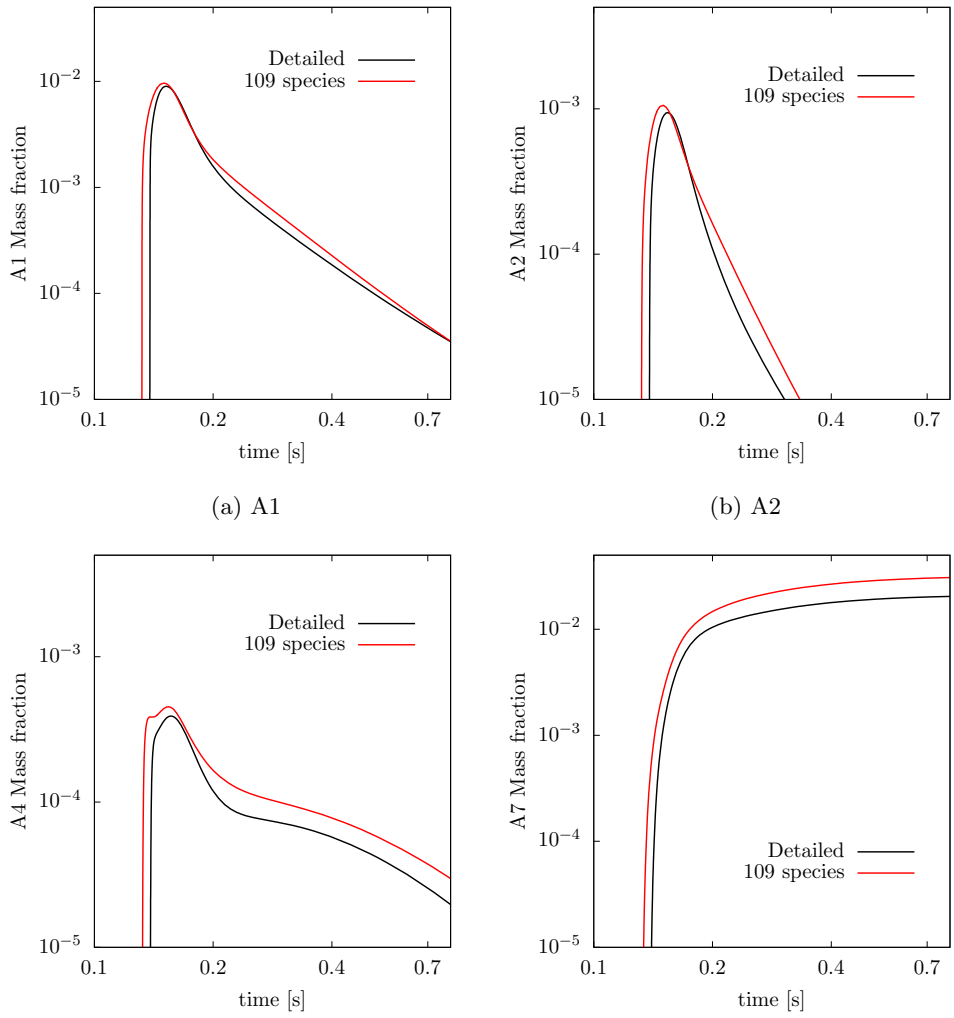

(a) A1 (b) A2

(c) A4 (d) A7

Figure 47: Comparison of PAH time evolution between detailed (black) and TSR-simplified (109 species, red) mechanism in a C_2H_4-air auto-ignition in the case of T=900K, p=1 atm, ϕ=5

exploiting the TSR-modified CSP skeletal algorithm and a variable tolerance approach, without the need of specifying any target species. This mechanism showed very good error

figures in both ignition delay times and equilibrium composition over a wide range of operating conditions. Then, taking advantage of the feature of the TSR-modified algorithm to add user-specified target species for PAH kinetics, a 109-species skeletal mechanism was obtained with fairly good ability of replicating the behavior of large PAHs, such as A2, A4 and coronen. This result becomes remarkable when compared to the 99-species skeletal mechanism obtained with expert-knowledge based and sensitivity-aided DRG methods in [57], since no knowledge and expert-information about important species were required.

4.4 Extension to steady-state reactive-diffusive problems

Consider a generic reactive flow system, whose dynamics is described by a set of PDEs of the form:

$$\frac{\partial \boldsymbol{y}}{\partial t} = \boldsymbol{L}_x(\boldsymbol{y}) + \boldsymbol{g}(\boldsymbol{y}), \qquad \text{BCs on } \boldsymbol{y}, \qquad \boldsymbol{y}(0) = \boldsymbol{y}_0. \tag{4.4.1}$$

where $\boldsymbol{y} \in \mathbb{R}^N$ and $\boldsymbol{g}(\boldsymbol{y})$ are defined as in Eq.(3.3.1), whereas $\boldsymbol{L}_x(\boldsymbol{y})$ represents a generic transport term such as convection or diffusion, or the sum of the two.

When the system reaches a steady-state condition, that is $\boldsymbol{L}_x(\boldsymbol{y}) = -\boldsymbol{g}(\boldsymbol{y})$, chemical kinetics and transport balance each other. The larger the transport term, the farther is the system from chemical equilibrium. The chemical processes of interest in a steady-state condition are those characterizing the chemical source term $\boldsymbol{g}(\boldsymbol{y})$ when balancing the transport term $\boldsymbol{L}_x(\boldsymbol{y})$. Therefore the aforementioned CSP-based simplification algorithm can be operated on the chemical source term associated with the steady-state solution. Hence, the definitions for the importance indices given in Eqs.(4.1.1) and (4.1.2) are employed. This local approach has been successfully employed for flame analysis in [29] and [60], and it is adopted hereby for skeletal mechanisms generation.

4.4.1 A simplification application: non-premixed combustion in hybrid rockets

Next, the above construction will be employed for the simplification of a 561-species, 2538-reactions, mechanism [61].

Selection of a suitable detailed mechanism

The detailed mechanism has been chosen in accordance with the physics of the application under study, that is the combustion process between butadiene and gaseous oxygen inside a hybrid rocket combustion chamber. The pressure range measured in both experiments and numerical campaign [62] spans the interval 3 to 36 bar. This prompts the need for a mechanism with a rather high pressure validation. Laskin *et al.* [63] proposed a mechanism

designed for butadiene oxidation, however validated at atmospheric pressure only. On the other hand, Curran *et al.* [61] proposed a n-heptane mechanism, containing C_4, C_5 and C_6 submechanisms, validated over a wider pressure range, that is $1 - 42$ atm. Although not specifically designed for butadiene oxidation, Curran *et al.* mechanism is conjectured to be more suitable for the present needs.

Simplification strategy

Since the combustion processes typical of hybrid rocket combustion chambers are mainly characterized by a diffusive nature, the prototypical model chosen for this application is the flamelet model described in appendix A. The choice of unity Lewis number is related to the fact that the skeletal mechanisms are expected to be used only in highly turbulent combustion simulations and therefore in conjunction with a turbulent combustion model. Indeed the Reynolds number of HTPB hybrid rockets GOx injector is typically $O(10^6)$ [62, 64], thus in such conditions turbulent stirring is expected to have a far greater role than molecular diffusion in determining the flame structure, overshadowing any differential diffusion effect. Therefore the conditional mean compositional structure of the present flames can be correctly represented by the $Le = 1$ solutions of the flamelet equations, as commonly encountered in canonical turbulent non-premixed flame [65, 66]. However, depending on the fuel composition and the burner configuration, differential diffusion can still play a significant role. In particular, this can be encountered in presence of very high scalar dissipation rates zones, which are usually located in the braid regions between large-scale Kelvin-Helmotz rollers [67, 68, 69, 70]. These high-strain layers in the braid regions are characterized by a quasi-laminar behavior so that the effect of turbulence is small compared to molecular diffusion and differential diffusion may play a significant role [71]. However these particular conditions are typical of the near field region of co-flowing jet flames[72], while in the present target configuration (a HTPB-based hybrid rocket) the flame emanates from a highly turbulent boundary layer with neither the formation of high scalar dissipation rates nor quasi-laminar regions. Taking into account differential diffusion effects in such situations can lead to a poor representation of the flame structure compared to a $Le = 1$ model, as demonstrated for highly turbulent jet flames [65, 66]. As a result, in the present

application, differential diffusion is neglected in the construction of the prototypical flame structures database for the chemical kinetic mechanism simplification.

In addition, due to the particular configuration of the target turbulent non-premixed flame, extremely high values of the scalar dissipation rate are not expected, and extinction events can be considered highly unlikely. Moreover, the target turbulent non-premixed flame is stably burning and anchored in the turbulent boundary layer by means of a large hot gases recirculation zone [64], which effectively acts as a pilot flame. For these reasons, only the stably burning branch of the classical S-shape curve has been considered in the generation of the representative flamelet dataset.

With the only exception of an initial transient behavior, these combustion chambers experience limited pressure changes, thus prompting the need for a simplified mechanism tailored over a single pressure value. It will be shown, however, that the simplified mechanisms are able to perform consistently also in the proximity of that pressure value.

It follows that each database should include the flamelet steady-state solutions obtained at different scalar dissipation rates and at a single pressure value.

Test case definition and numerical implementation

In this work, the datasets, consisting of steady-state solutions of laminar flamelets, are obtained at the pressure values of 3, 17 and 36 bar respectively, spanning the pressure range of the aforementioned experiments and numerical campaigns [62]. The choice of the pressure values is purely demonstrative, and any other pressure value may be used. At each pressure, different solutions are obtained by varying the scalar dissipation rate χ from the lowest value of 1 s^{-1} to the quenching value, covering the stable burning branch of the S-shaped curve. Thus, three campaigns of mechanism simplification are presented, one for each selected pressure value. Finally, a comprehensive campaign is presented where the databases obtained at different pressures and scalar dissipation rates are fed all at once into the algorithm, providing simplified mechanisms that are expected to be accurate in the whole pressure range.

The boundary conditions for all the flamelet problems are set as T_{OX} = 300 K, accord-

ing to the enforced oxidizer temperature in [62], and $T_{FU} = 700$ K, being representative of the temperature at which butadiene is produced at the pyrolyzing fuel surface. Each simplification campaign, carried out with the classic CSP algorithm described in § 4.1.1, allows to generate a set of simplified mechanisms of different size, following the specification of a number of increasing thresholds on the importance indices and the selection of a set of target species, namely: the fuel, C_4H_6, the oxidizer, O_2, and the products, CO_2, H_2O, CO, O, H_2, OH and C_2H_2. It is important to highlight that also temperature is part of the set of target variables. While the first 7 species are rather essential for gaining a good accuracy in the simplified mechanisms, OH and C_2H_2 have been specifically added being interesting in this particular scope. The OH radical is one of the most chemically aggressive species against a carbon-based nozzle material surface, therefore its accurate prediction is considered important to evaluate hybrid rockets throat erosion. Acetylene, C_2H_2, on the other hand, is an important Polycyclic Aromatic Hydrocarbons (PAH) precursor that can be correctly represented by steady state flamelet solutions because of its relatively fast chemistry [73]. Moreover, simplified and semi-empirical soot models at elevated pressures generally use acetylene-based chemistry for soot inception and growth [74]. Indeed, soot could strongly affect the thermal radiation processes within a hybrid rocket combustion chamber, which in turn contribute to the regression rate of the grain. The numerical solutions generation and the mechanism simplification are carried out by resorting to CSPTk [35], which integrates in time the flamelet model of Eq.(A.2.1), using CVODE [36] and the TChem package [37] for the thermo-kinetic database management.

Error definitions

The CSP-based simplification procedure does not allow to enforce an *a-priori* error requirement on the simplified mechanisms, due to the highly non linear character of the system of interest. For a given generated skeletal mechanism, an *a-posteriori* error estimation needs to be carried out to assess its quality in replicating the quantities of interest, in this case consisting of the steady-state solutions of the species of interest. The discrepancies between the steady-state solutions generated with the detailed and the simplified mechanisms, namely $Y_\alpha^d(z)$ and $Y_\alpha^\tau(z)$, $\alpha = 1, ..., N_s + 1$, the latter identified by the threshold

τ enforced on the importance indices, can be computed as an integral measure of their distance in the mixture fraction space. For the $\alpha-$th component of the state vector, it reads:

$$\hat{E}_\alpha^\tau = \frac{\int_0^1 |Y_\alpha^d(z) - Y_\alpha^\tau(z)| \quad dz}{\int_0^1 |Y_\alpha^d(z)| \quad dz}, \tag{4.4.2}$$

which has been normalized with the integral of the detailed solution.

The error of the simplified mechanism is defined as the average of the errors associated to the target species:

$$\hat{E}^\tau = \frac{\sum_{\alpha=1}^{N_{\text{tgt}}} E_\alpha^\tau}{N_{\text{tgt}}}, \tag{4.4.3}$$

where N_{tgt} is the number of target species considered. This error is expected to be much lower than the error averaged over all the species since, by construction, the skeletal mechanisms are tailored over the target species only.

Another useful error measure is used to quantify the discrepancy between detailed and simplified mechanisms' steady-state solutions at a given mixture fraction z^*. It is defined as:

$$E_\alpha^\tau = \hat{E}_\alpha^\tau \mid_{z=z^*} \tag{4.4.4}$$

As a general trend, higher accuracy on the whole mixture fraction space requires large mechanisms because of the need to capture different regions characterizing the diffusive flames, namely lean, stoichiometric and rich mixtures. However, the available computational resources force the accuracy requirements to be confined to a narrower range of mixture fractions, which are relevant to the problem of interest, such as the stoichiometric region. In those cases, it is preferable to adopt the error measure defined in Eq.(4.4.4) instead of Eq. (4.4.3).

Single-pressure skeletal mechanisms

The thresholds on importance indices have been chosen as to obtain sets of simplified mechanisms ranging from 17 to 39 species. Mechanisms that include a larger number of species may be used for tabulated chemistry approaches, such as flamelet libraries, while smaller mechanisms (20 species or less) are specifically suited to CFD with finite-

rate chemistry approaches. The performance of the simplified mechanisms is evaluated by employing them in analogous flamelet problems.

Figure 48 shows a comparison between the steady-state solutions computed with the detailed mechanism and 3 selected simplified mechanisms, obtained for the 3 bar case, and employed with scalar dissipation rate values of 10 and 10^4 s^{-1}. In particular, the temperature and a selection of target species mass fractions in the mixture fraction space, namely OH, CO and C_2H_2, are presented. Similarly, figures 49 and 50 show the same comparison for the 17 and 36 bar cases. Although a very good agreement can be already observed, even for the smallest mechanism, a rigorous quantitative measure of the discrepancies between the results obtained with detailed and simplified mechanisms is given by error measures such as those presented in § 4.4.1.

The error on temperature at stoichiometric mixture fraction and the number of retained species are the key figures of merit in deciding whether the performance of a given mechanism is suitable for a CFD simulation such as those presented in [62, 64, 75].

On the other hand, larger mechanisms such as those typically employed for the generation of flamelet libraries may be chosen looking at more comprehensive error figures such as the one in Eq.(4.4.3), which evaluates the steady-state solution accuracy over the whole mixture fraction range.

Figure 51 represents the performance of the simplified mechanisms for the 3 bar case. The simplified mechanisms were employed on flamelet problems at the pressure of 3 bar and with various scalar dissipation rate values, ranging from 1 to 10^5 s^{-1}, the latter being close to the quenching value. Figure 51a shows the integral errors as per Eq.(4.4.3). All the mechanisms have errors on the steady-state solutions of the target species bounded below 10% and, as a general trend, lower errors correspond to larger mechanisms. It can also be noted that the mechanisms perform better at intermediate scalar dissipation rate values. The more complex chemistry-diffusion interaction at scalar dissipation rates close to the quenching value, where unsteadiness becomes more and more dominant, requires the addition of more species/reactions to maintain a high accuracy level. Nonetheless, at low scalar dissipation rates the diffusion effects are weaker and the kinetics processes are dominant also in the rich side, triggering the activation of possibly very different chemical

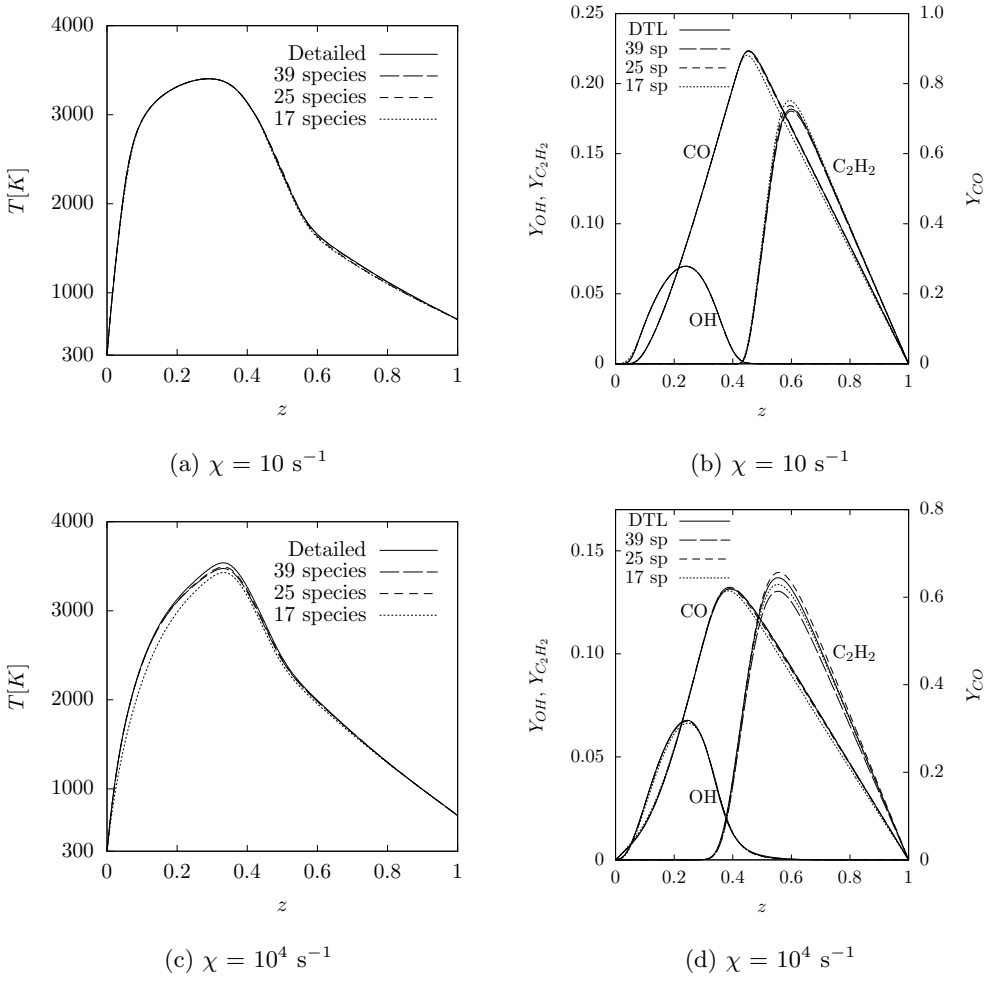

(a) $\chi = 10$ s^{-1}

(b) $\chi = 10$ s^{-1}

(c) $\chi = 10^4$ s^{-1}

(d) $\chi = 10^4$ s^{-1}

Figure 48: 3 bar case: Temperature and CO, OH, C_2H_2 mass fractions profiles with $\chi = 10$ s^{-1} and $\chi = 10^4$ s^{-1}. Detailed and 3 simplified mechanisms (17, 25 and 39 species)

pathways. It was observed that the inclusion of chemical pathways involving Crotyl (C_4H_7) and 1-Butene (C_4H_8) is crucial for the accurate replication of the steady-state solution in the rich side at low χ values, and only the two larger mechanisms (39 species and 37 species) include them. This discussion highlights two important consequences in the simplification campaign: first, given that the simplification algorithm is fed with all the solutions at once, with the aim of generating mechanisms that can be used throughout the whole χ

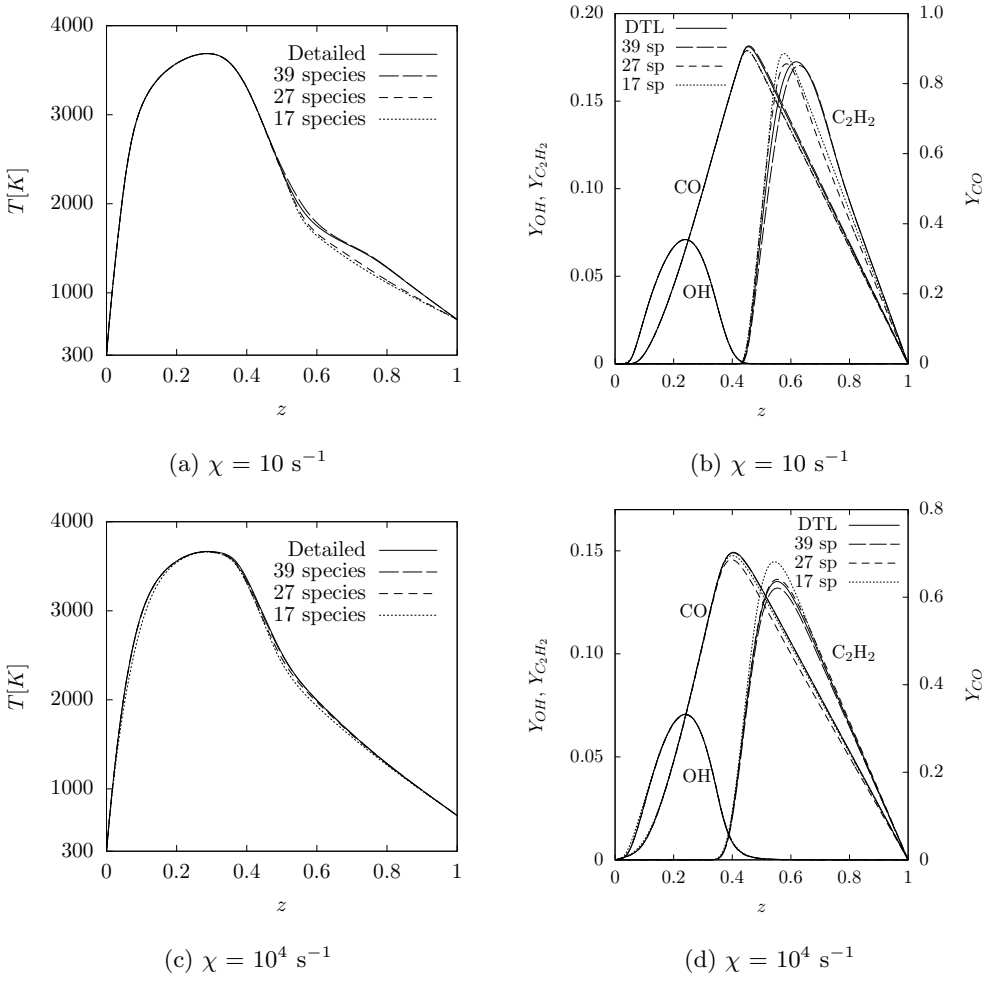

(a) $\chi = 10\ \mathrm{s}^{-1}$ (b) $\chi = 10\ \mathrm{s}^{-1}$

(c) $\chi = 10^4\ \mathrm{s}^{-1}$ (d) $\chi = 10^4\ \mathrm{s}^{-1}$

Figure 49: 17 bar case: Temperature and CO, OH, C_2H_2 mass fractions profiles with $\chi = 10\ \mathrm{s}^{-1}$ and $\chi = 10^4\ \mathrm{s}^{-1}$. Detailed and 3 simplified mechanisms (17, 27 and 39 species)

range, these reaction pathways, that are active in the low χ cases only, are considered less important than others, and are included only when low thresholds on the importance indices are chosen, thus generating a larger number of retained species. Second, their inclusion is not effective in lowering the error at higher scalar dissipation rates, as Figure 51a shows for the 37- and 39-species mechanisms. Figure 51b, instead, shows the errors on temperature at the stoichiometric mixture fraction only. As expected, the error increases with χ and

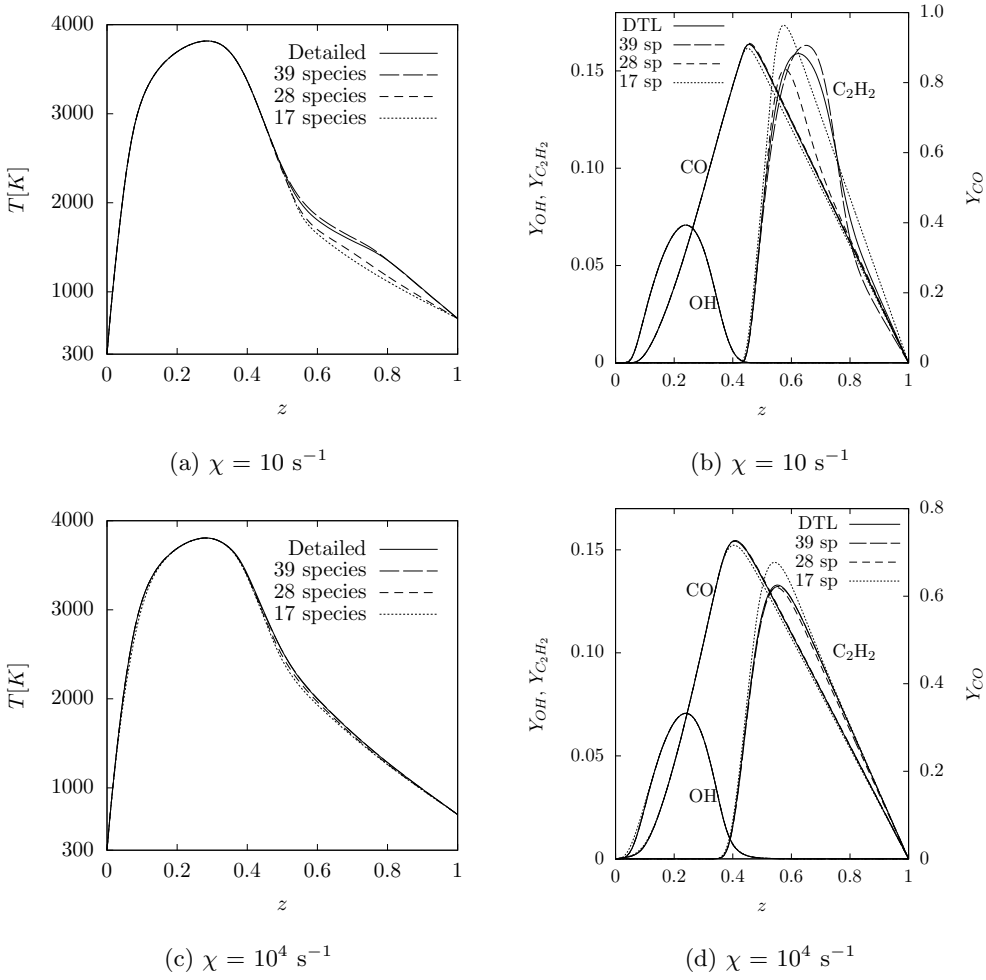

(a) $\chi = 10\ \mathrm{s}^{-1}$ (b) $\chi = 10\ \mathrm{s}^{-1}$

(c) $\chi = 10^4\ \mathrm{s}^{-1}$ (d) $\chi = 10^4\ \mathrm{s}^{-1}$

Figure 50: 36 bar case: Temperature and CO, OH, C_2H_2 mass fractions profiles with $\chi = 10\ \mathrm{s}^{-1}$ and $\chi = 10^4\ \mathrm{s}^{-1}$. Detailed and 3 simplified mechanisms (17, 28 and 39 species)

decreases with mechanism size, being always bounded below 10%. The inclusion/exclusion of the aforementioned pathway, that affects the rich side only, does not appear in this error measure.

Figures 52 and 53 show the same error trends with χ and mechanism size, with a pressure effect that extends the kinetics-dominant domain typical of the low scalar dissipation rates. Thus, the error minima can be seen shifted to the right in Figures 52a and 53a.

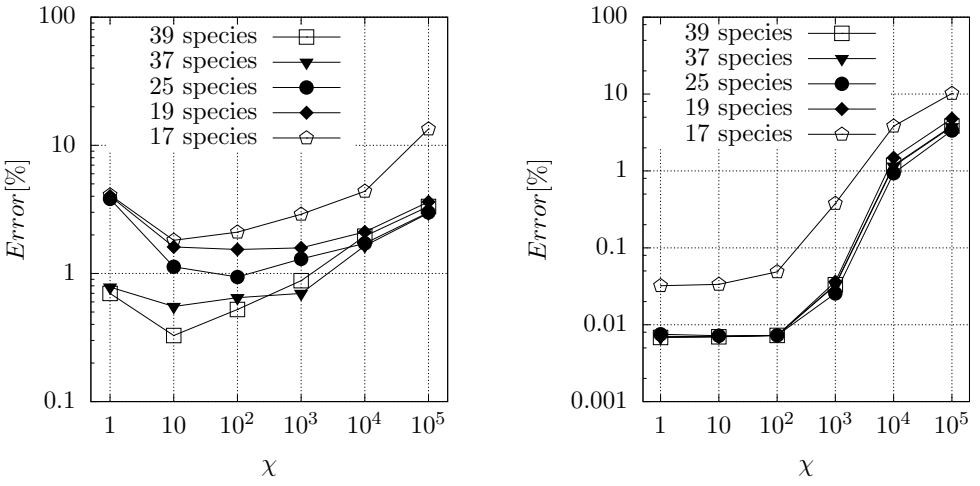

(a) $\hat{E}^{\tau}_{\alpha}$ (b) E^{τ}_{α}

Figure 51: 3 bar case: errors averaged over the target species on the whole mixture fraction range (a) and errors of temperature at stoichiometric mixture fraction (b)

The errors on temperature at stoichiometric mixture fraction (see Figures 52b and 53b), although maintaining the general trend of the 3 bar case, are sensibly lower, at least for χ sufficiently far from the quenching value.

A similar rich side, low-χ, behavior can be observed in Figs.50a and 50b, that depict temperature, CO, OH and C_2H_2 solutions in the 36 bar case, at $\chi = 10\ s^{-1}$. The 39-species mechanism is the only one capable of reproducing the features of the detailed solution in the rich side with a high degree of fidelity. The same behavior is visible at lower pressures, as in Figs.48a, 48b, 49a and 49b, although less evident because of the aforementioned effect of reduction of the low-χ-region where the inclusion of different pathways is important.

The reduced mechanisms, obtained at a single pressure value, are actually good performers also in a range of values around the selected pressure of generation. As an example, Figure 54 shows the errors obtained with the simplified mechanisms generated at 17 bar and employed at 14 and 20 bar, in the case of $\chi = 100\ s^{-1}$. The errors remain well bounded even changing the pressure by $\pm 20\%$, confirming their validity even in case of pressure variations. Generally speaking, the smallest mechanisms, which comprise 17 species, proved to

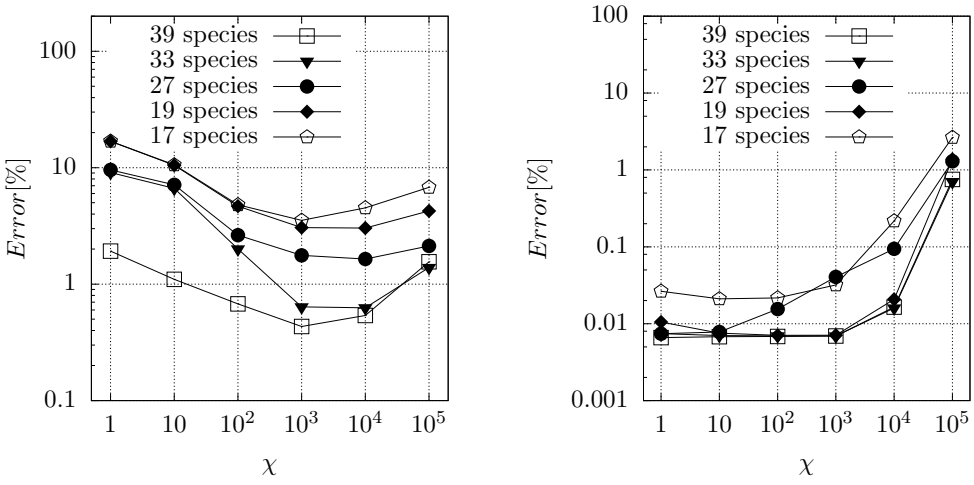

(a) $\hat{E}^{\tau}_{\alpha}$ (b) E^{τ}_{α}

Figure 52: 17 bar case: errors averaged over the target species on the whole mixture fraction range (a) and errors of temperature at stoichiometric mixture fraction (b)

have acceptable, *i.e.* around 10%, error figures over the whole mixture fraction range, and very good error figures at the stoichiometric mixture fraction, exhibiting errors on temperature as low as 1% for almost all the χ and pressure values. Larger, flamelet libraries oriented, mechanisms in the range of 30 to 40 species, were able to perform under 5% error throughout the whole z field.

Pressure-comprehensive skeletal mechanisms

Next, a simplification campaign is performed to generate skeletal mechanisms presumed to be valid through the whole 3-36 bar pressure range. This is achieved by feeding the simplification algorithm with the databases of states computed as flamelet steady-state solutions at the three representative pressure values of 3, 17 and 36 bar and in the aforementioned range of scalar dissipation rate values. The skeletal mechanisms are shown in Table 4.6, with different degrees of fidelity obtained by varying the τ threshold on the CSP importance indices. Insights on the effects of the threshold on the retained species can be drawn from Table 4.6. In particular, recalling that the kernel set of target species is retained by

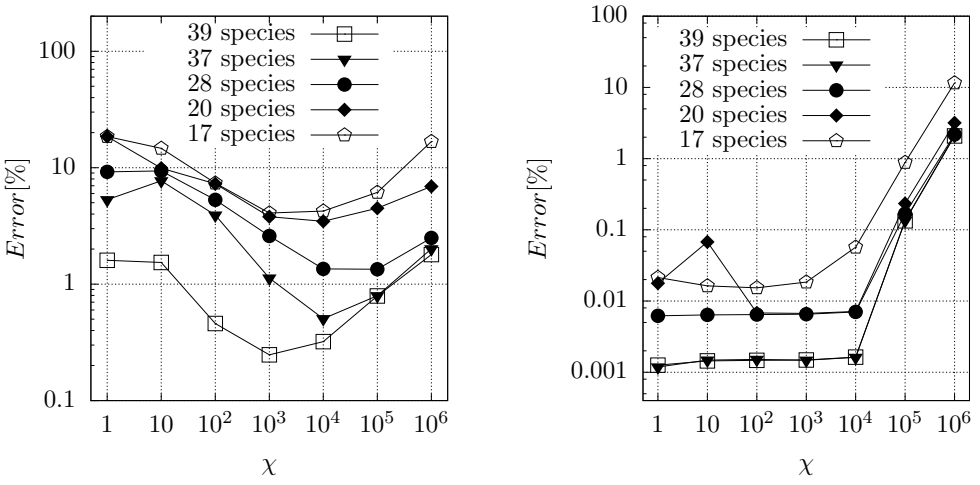

(a) $\hat{E}^{\tau}_{\alpha}$ (b) E^{τ}_{α}

Figure 53: 36 bar case: errors averaged over the target species on the whole mixture fraction range (a) and errors of temperature at stoichiometric mixture fraction (b)

construction, the core species are those retained up to the greatest level of simplification, this suggesting that the algorithm can be also employed as a diagnostics instrument.

The skeletal mechanisms are then re-employed at five pressure values to compute *a-posteriori* errors, namely the pressures of generation and two intermediate pressure values of 10 bar and 27 bar.

Figure 55 shows the error figures of three select mechanisms having 39, 30 and 20 species, respectively. First, it can be observed that, as expected, the larger the number of species, the lower the errors. Then, it is visible that, coherently with what has been previously discussed, the mechanisms perform better in a region of intermediate scalar dissipation rate values, while higher errors are present in very low and very high scalar dissipation rate regions, due to the lack of representation of the rich pathways and the proximity to the quenching region, respectively. Moreover, the pressure increase results in the shift of the error curves towards higher scalar dissipation rate values, as discussed before. Nonetheless, it can be concluded that each comprehensive mechanism has comparable error figures when employed at different pressure values, including the intermediate values of 10 and 27 bar

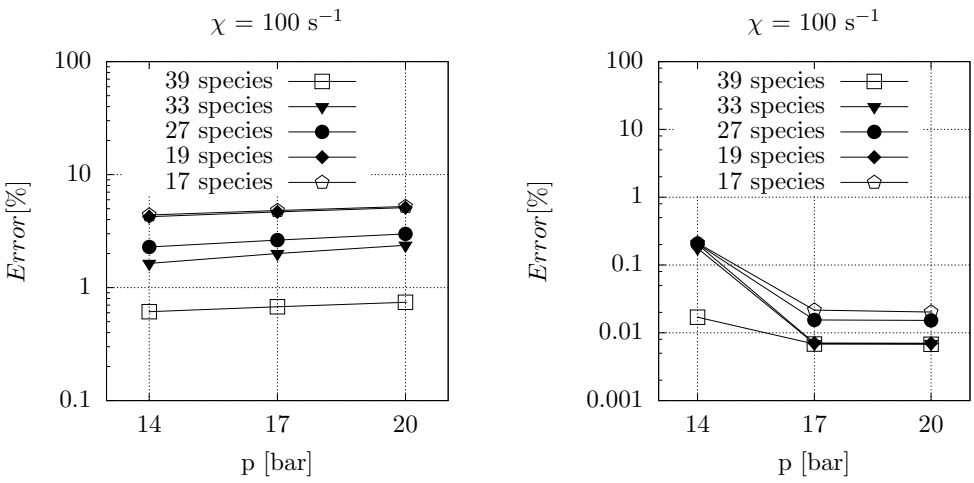

(a) $\hat{E}^{\tau}_{\alpha}$ (b) E^{τ}_{α}

Figure 54: 17 bar pressure range: errors averaged over the target species on the whole mixture fraction range (a) and errors of temperature at stoichiometric mixture fraction (b)

which have not been used for the database generation. In particular, the largest, 39-species, mechanism shows errors as per Eq.(4.4.3) that span between 0.3% and 6% regardless of the pressure of operation, while the smallest, 20-species, exhibits errors comprised between 1% and 11%.

Figure 56 shows the comparison of the upper stable branches of the S-shape curve obtained with the detailed mechanism and the three comprehensive skeletal mechanisms, at the 3 reference pressures. Good agreement is observed throughout the entire scalar dissipation range, with the only exception of the values very close to the extinction value of the detailed mechanism, which, however, are not expected in the application.
This kind of mechanisms can hence be considered suitable for applications characterized by large pressure changes.

Table 4.6: Retained species in the comprehensive simplified mechanisms. Target species are in bold.

Species name	39	33	27	19	17	*Species name*	39	33	27	19	17
H	x	x	x	x	x	HCCO	x	x	x	x	x
H2	x	x	x	x	x	CH2CO	x	x	x	x	x
OH	x	x	x	x	x	C3H4-A	x				
O	x	x	x	x	x	CH2CHO	x	x			
O2	x	x	x	x	x	C3H4-P	x	x	x		
H2O	x	x	x	x	x	C3H6	x	x	x		
HCO	x	x	x	x	x	**C4H6**	x	x	x	x	x
CO	x	x	x	x	x	C4H7	x	x			
CO2	x	x	x	x	x	C4H8-2	x				
CH3	x	x	x			C4H8-1	x				
CH4	x	x				C5H9	x	x			
H2O2	x					C2H3O1-2	x	x			
HO2	x	x	x			C2H3CO	x	x	x	x	
CH2O	x	x	x			C3H5-S	x	x	x		
C2H4	x	x	x	x		C3H5-A	x	x	x		
C2H5	x					C3H2	x	x	x	x	x
CH2	x	x	x	x	x	C3H3	x	x	x	x	x
C2H2	x	x	x	x	x	C7H13	x	x			
C2H3	x	x	x	x	x	C4H7CO1-4	x				
C2H	x	x	x								

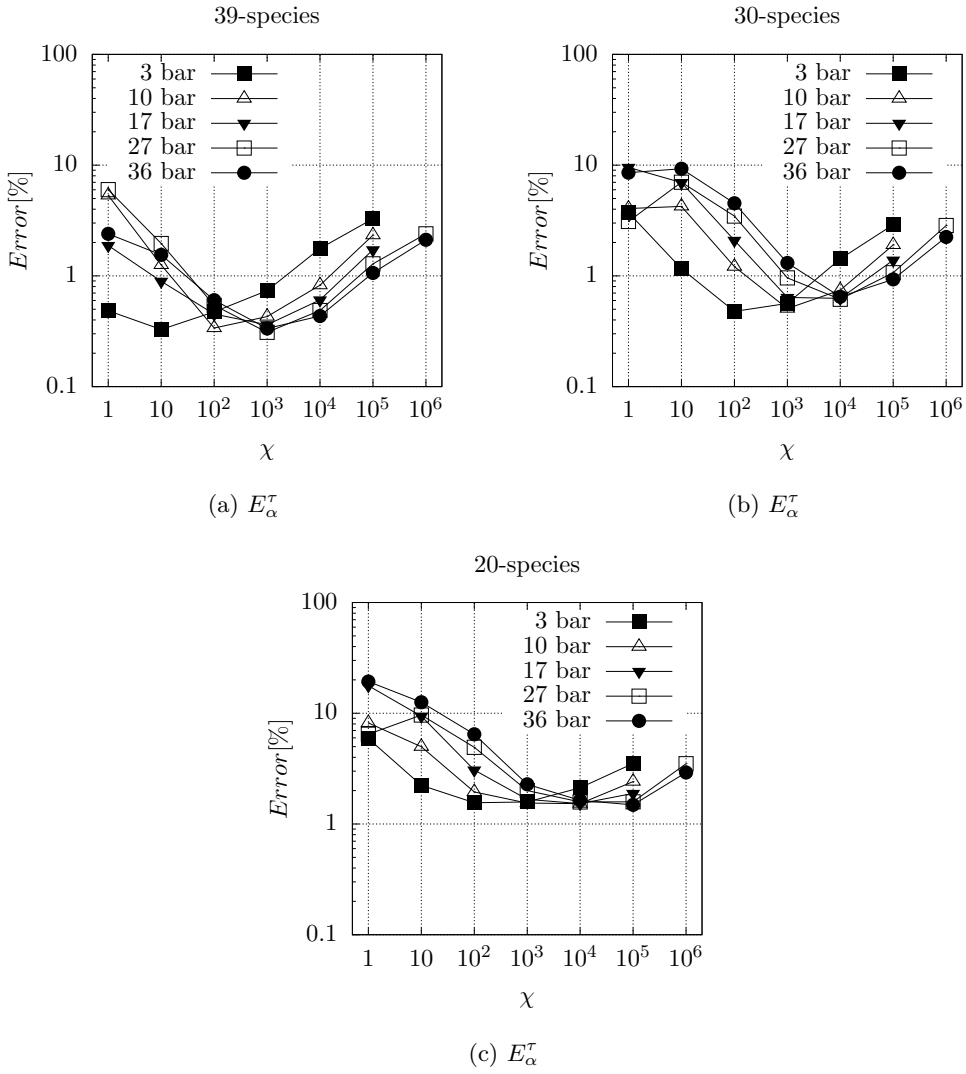

(a) E_α^τ

(b) E_α^τ

(c) E_α^τ

Figure 55: Errors averaged over the target species on the whole mixture fraction range for three comprehensive skeletal mechanisms: 39-species (a), 30-species (b) and 20-species (c)

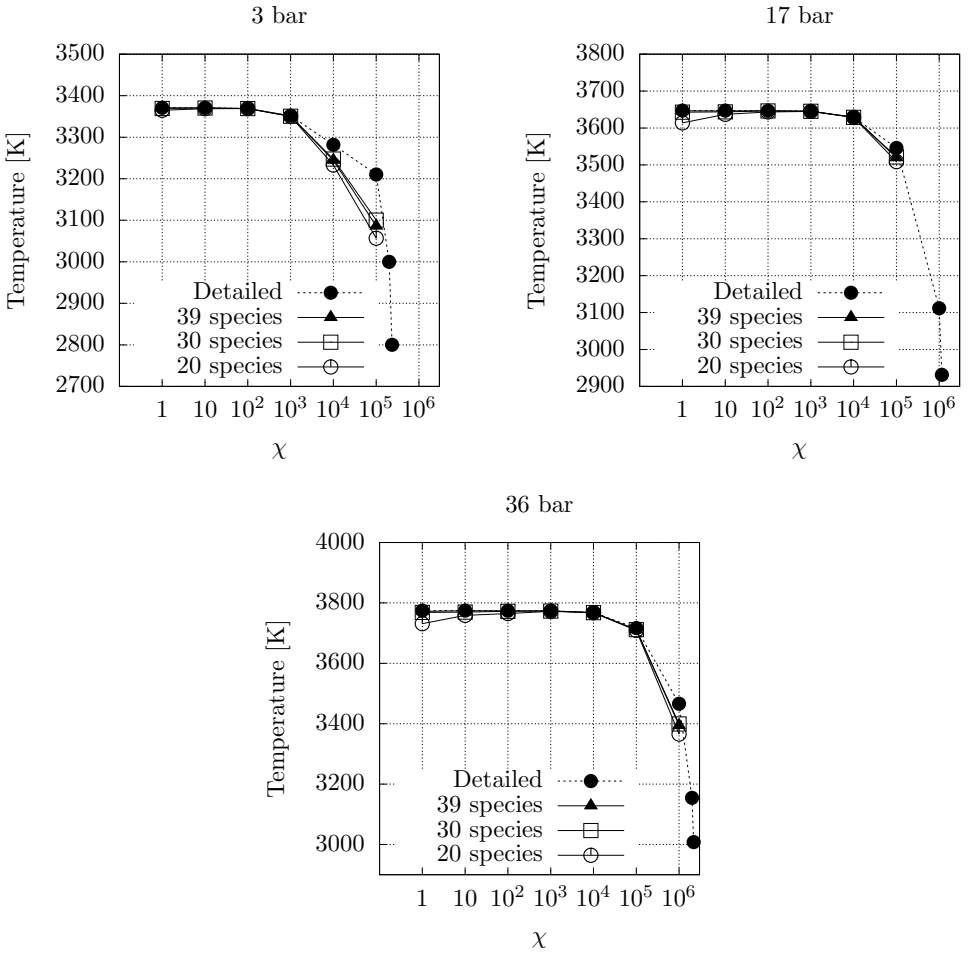

Figure 56: S-shape upper branches with comprehensive mechanisms for the three comprehensive skeletal mechanisms at the pressures of 3 bar, 17 bar and 36 bar.

Chapter 5

Skeletal mechanism generation with uncertainty

Chemical model reduction strategies generally start from a detailed chemical kinetic mechanism as the reference or baseline gold-standard. Given this standard, a specified range of operating conditions or set of state vectors, a select set of Quantities of Interest (QoIs), and a requisite error threshold, a model reduction strategy produces a simplified mechanism of associated size/complexity [51, 76].

This strategy, despite its effectiveness, nonetheless relies on the quality of the starting mechanism. Yet, there is typically significant uncertainty in both the structure of available detailed mechanisms for hydrocarbon fuels, and in their thermodynamic and chemical kinetic rate parameters. Therefore, in principle, the analysis/reduction processes that provide simplified mechanisms starting from the detailed mechanism, and the measures of quality of a simplified mechanism relative to the detailed mechanism, need to account for both model and parametric uncertainties in both mechanisms. This is a challenging, yet highly relevant topic. Overconfidence in the detailed mechanism can lead to a misplaced focus on tight error tolerances in the simplified model, relative to a faulty/uncertain baseline. Simplified model errors ought to be handled along with detailed model uncertainties in the same error budget. Any error norm between simplified and detailed models ought

to be weighted appropriately with attendant uncertainties. Moreover, the fact that both the detailed and simplified mechanisms are burdened with uncertainty suggests that any measures of distance between their predictions be done in a probabilistic context. This line of reasoning highlights the need for rethinking model analysis/reduction strategies for uncertain chemical kinetic models.

The above is a significant undertaking with a range of technical challenges. There has been some work addressing model reduction under uncertainty in the context of proper orthogonal decomposition (POD) [77], albeit for small degrees of uncertainty. The dynamical analysis of uncertain ordinary differential equation (ODE) systems has also received some attention [78, 79], in a full probabilistic setting. Further, from the process control perspective, there has also been work [80, 81] addressing dynamical systems reduction under parametric uncertainty, relying on balanced truncation [82, 83], singular value decomposition, and sensitivity analysis. Note that this work [80, 81] presumes parameter variations in intervals, with no probabilistic information. It is not clear, however, how well these methods, traditionally employed for process control in linear or mildly-nonlinear contexts, and, more specifically applied by [80, 81] for chemical process and isothermal biochemical systems modeling, extend to the strongly nonlinear thermally activated stiff kinetics of hydrocarbon fuels. It is fair to say that the challenge of dynamical analysis and uncertain chemical model simplification in hydrocarbon kinetics of relevance to combustion has yet to receive significant attention.

In the following, a general strategy for analysis and reduction of uncertain chemical kinetic models is laid out, and its utilization in the context of ignition of hydrocarbon fuel-air mixtures is described. The construction is fully probabilistic, allowing for an arbitrary uncertainty structure. It is based on the CSP analysis and reduction strategy, which has been thoroughly discussed in the previous chapters.

5.1 Simplification Strategy under Uncertainty

Consider a detailed chemical mechanism $\mathcal{M}^*(\lambda)$, defined by a set of species $\mathcal{S}^* = \{S_1, \ldots, S_N\}$ and elementary reactions $\mathcal{R}^* = \{R_1, \ldots, R_M\}$, where λ is the relevant vector of uncertain

parameters, *e.g.* the Arrhenius rate parameters of all reactions. Consider the auto-ignition process of a hydrocarbon fuel-air system in a constant pressure batch-reactor, for a range of initial temperature and stoichiometry, which is used to compute a set of ignition trajectories, providing a database of states $D = \{X^{(1)}, \cdots, X^{(K)}\}$, where $X \in \mathbb{R}^{N+1}$ is the state vector composed of temperature and the N mole fractions. Given that λ is uncertain, let D_λ denote the database computed for a given value of λ.

For any given D_λ, and considering a given set of QoIs - such as the set of target species - and a tolerance τ on Importance Indices, the CSP-based analysis and simplification strategy provides a simplified mechanism $\mathcal{M}_\tau(\lambda)$, being a subset of the starting mechanism with species $\mathcal{S}_\tau(\lambda)$ and reactions $\mathcal{R}_\tau(\lambda)$. In fact, given the starting model specification, the simplified model can be specified compactly in terms of a vector of M binary indicators $\alpha^\tau(\lambda) = (\alpha_1^\tau(\lambda), \ldots, \alpha_M^\tau(\lambda))^T$, where

$$\alpha_r^\tau(\lambda) = \begin{cases} 1 & \text{for reaction } R_r \in \mathcal{R}_\tau(\lambda) \\ 0 & \text{otherwise.} \end{cases}, \qquad r = 1, \ldots, M \tag{5.1.1}$$

In fact, $\alpha^\tau(\lambda)$ is a multi-index that specifies 2^M models. The process of database generation, analysis, and model simplification can be viewed as an input-output map:

$$f_\tau(\lambda) : \lambda \to \alpha^\tau(\lambda), \tag{5.1.2}$$

which provides a convenient abstraction for the use of uncertainty quantification (UQ) methods to account for uncertainty in λ in the process of simplified model selection.

Placing ourselves in a probabilistic UQ setting, uncertain quantities are represented as random variables. Accordingly, λ is defined as a real-valued random vector with a presumed joint Probability Density Function (PDF) $p(\lambda)$. The specification of this PDF is a major challenge in general, requiring recourse to available data on each parameter in the model, and allowing proper accounting for the correlation among different uncertain parameters. This challenge, as regards chemical mechanisms for combustion, is discussed later below in § 5.3.

Generating n random samples from $p(\lambda)$, $\{\lambda^{(1)}, \cdots, \lambda^{(n)}\}$, the input-output map of Eq.(5.1.2) provides corresponding samples $\{\alpha^{\tau j}\}_{j=1}^n$, where $\alpha^{\tau j} = \alpha^\tau(\lambda^{(j)})$, that allow to

estimate, $\forall \alpha = (\alpha_1, \cdots, \alpha_M)$, the joint probabilities,

$$P_\tau(\alpha) \approx \frac{1}{n} \sum_{j=1}^{n} \delta_{\alpha^{\tau j} \alpha} \tag{5.1.3}$$

where $\delta_{\alpha^{\tau j} \alpha}$ is the Kronecker delta,

$$\delta_{\alpha^{\tau j} \alpha} = \begin{cases} 1 & \text{if } \alpha = \alpha^{\tau j} \\ 0 & \text{otherwise.} \end{cases} \tag{5.1.4}$$

Thus, the contribution of each sample j to the sum for $P_\tau(\alpha)$ in Eq. (5.1.3) is 1 if $\alpha^{\tau j} = \alpha$, and 0 otherwise. Further, it holds:

$$\delta_{\alpha^{\tau j} \alpha} = \prod_{i=1}^{M} \delta_{\alpha_i^{\tau j} \alpha_i}. \tag{5.1.5}$$

The joint probabilities provide a wealth of information on the coupling among reactions. For example, marginalizing over $M-2$ reactions, provides the 2-way joint probabilities for any two given reactions (p, q),

$$P_\tau(\alpha_p, \alpha_q) \approx \frac{1}{n} \sum_{j=1}^{n} \delta_{\alpha_p^{\tau j} \alpha_p} \delta_{\alpha_q^{\tau j} \alpha_q}. \tag{5.1.6}$$

This provides information on the relevance of two reactions p and q being included/excluded jointly or separately in the model. Similarly, this analysis can be generalized to any subset of reactions forming a pathway of interest. Moreover, extending the scope to a full sub-mechanism, the joint picture provides a statement concerning the probability of any given mechanism that is a subset of the detailed model. Given a reasonable search strategy on α, one can thus select the model with the highest $P(\alpha)$ as the one most supported by the reduction strategy. Alternatively, if multiple models have comparable probability, a Bayesian model averaging [84, 85] strategy can be employed to provide a pooled/average prediction.

Given the complexity of the joint-picture, and the need for large numbers of samples to establish multivariate statistics, this study is confined to the marginal probabilities for individual reactions,

$$P_\tau(\alpha_i) \approx \frac{1}{n} \sum_{j=1}^{n} \delta_{\alpha_i^{\tau j} \alpha_i}, \qquad i = 1, \ldots, M. \tag{5.1.7}$$

With this, and since $\delta_{\alpha_i^{\tau j}1} \equiv \alpha_i^{\tau j}$, the marginal probability that a reaction is included in the simplified mechanism for a given τ, is given by

$$\mathcal{P}_i^\tau = P_\tau(\alpha_i = 1) \approx \frac{1}{n}\sum_{j=1}^{n} \alpha_i^{\tau j}. \tag{5.1.8}$$

In this way, a novel strategy is proposed for model reduction under uncertainty, whereby a reaction is included in the simplified mechanism for a given τ, when its marginal probability satisfies $\mathcal{P}_i^\tau > \theta$, where $0 < \theta < 1$ is a user-specified threshold.

It is worth to note, of course, that this marginalization is applied to samples, each of which is a mechanism selected based on CSP analysis and the associated simplification strategy for the chosen sample of the Arrehnius parameter vector of the detailed mechanism. Thus, if, say, partial equilibration or other dynamical arguments strongly require that a given pair/tuple of reactions be included together or not at all, then when one of these reactions is included with high/low marginal probability, the other(s) will be as well. As a result, these pairings/groupings will be implicitly respected in the marginally selected mechanism. Accordingly, the predominant impact of the limitation of the present scope to marginal statistics is that, for the present, explicit discovery/discussion of such groupings where they do exist is postponed to future work.

5.2 Error measures

In chapter 4 (see § 4.1.3), a number of error measures were introduced to assess the quality of a given simplified mechanism with respect to the detailed one. These errors involve ignition delay time in the $\{t, X_i(t)\}$ phase space, equilibrium temperature and composition, and trajectory discrepancies in a suitable phase space, where mixture entropy was chosen as progress variable instead of time.

In our probabilistic framework, we have uncertain predictions $X_i(\tilde{s}, \lambda)$ for each component of the state vector, based on any simplified model, and $X_i^d(\tilde{s}, \lambda)$ based on the detailed model. Probabilistic distributions of the distances, either in the $\{t, X_i(t)\}$ phase space, and/or in the $\{\psi(t), X_i(t)\}$ phase space, can be obtained by comparing the uncertain predictions on a sample-by-sample basis, giving way to the production of a number of prob-

abilistic results such as averages, standard deviations, or quantiles of the distance-based error.

Other compact probabilistic error measures in the $\{\psi, X_i\}$ plane may be obtained comparing directly the averages and standard deviations of the uncertain trajectories produced with the detailed mechanism and any given simplified mechanism, as follows. Introducing first the mean (μ) and standard deviation (σ) functions for the set of trajectories generated by the λ samples as:

$$\mu_i(\tilde{s}) = \mathrm{E}[X_i(\tilde{s},\lambda)], \qquad \mu_i^d(\tilde{s}) = \mathrm{E}[X_i^d(\tilde{s},\lambda)], \qquad i = 1, ..., N+1 \tag{5.2.1}$$

$$\sigma_i(\tilde{s}) = (\mathrm{V}[X_i(\tilde{s},\lambda)])^{\frac{1}{2}}, \qquad \sigma_i^d(\tilde{s}) = (\mathrm{V}[X_i^d(\tilde{s},\lambda)])^{\frac{1}{2}}, \quad i = 1, ..., N+1 \tag{5.2.2}$$

where $\mathrm{E}[\cdot]$ is the expectation, and $\mathrm{V}[\cdot]$ is the variance, both over λ, it is possible to define the weighted relative error norms, with $w_i(\tilde{s}) \equiv 1/\sigma_i^d(\tilde{s})$

$$E_{\mu_i}^p \equiv \chi_{p,w_i}(\mu_i, \mu_i^d) \approx \frac{\left(\sum_{k=1}^K w_i(\tilde{s}_k)|\mu_i(\tilde{s}_k) - \mu_i^d(\tilde{s}_k)|^p\right)^{\frac{1}{p}}}{\left(\sum_{k=1}^K w_i(\tilde{s}_k)|\mu_i^d(\tilde{s}_k)|^p\right)^{\frac{1}{p}}}. \tag{5.2.3}$$

where K is the number of discrete points. This measure quantifies the distance between the average transient evolution of the *i-th* species concentration computed with a detailed and a reduced model, giving a larger weight to the distance where the standard deviation of the detailed model is smaller. Similarly,

$$E_{\sigma_i}^p \equiv \chi_{p,w_i}(\sigma_i, \sigma_i^d) \tag{5.2.4}$$

where the comparison is between the standard deviations. Errors for each species/temperature can be averaged over all species/temperature, and/or over the target species, the latter being a useful measure to rank the quality of the simplified mechanisms, given that, by construction, the skeletal mechanisms are tailored for the target species. Thus, the compact error measures on averages and standard deviations are:

$$E_{\mu_{\mathrm{tgt}}}^p = \frac{\sum_{i=1}^{N_{\mathrm{tgt}}} E_{\mu_i}^p}{N_{\mathrm{tgt}}}, \tag{5.2.5}$$

and

$$E_{\sigma_{\mathrm{tgt}}}^p = \frac{\sum_{i=1}^{N_{\mathrm{tgt}}} E_{\sigma_i}^p}{N_{\mathrm{tgt}}} \tag{5.2.6}$$

where the sum is extended to the target species only.

5.3 Application to a n-butane mechanism

The utilization of the above construction for simplification is next described employing a 176-species, 1111-reaction, uncertain n-butane-air mechanism with published uncertainty for Arrhenius rate parameters [86], in constant pressure homogeneous ignition. First, the convergence of the results as a function of the number of random samples is explored, then errors in ignition delay time and uncertain trajectories with respect to the detailed mechanism are examined.

The specification of uncertain parameters in [86] is in the form of temperature dependent uncertainty factors $F_r(T)$ for the Arrehnius forward rate $k_r(T)$ of each reaction $r = 1, \ldots, M$. Uncertainty factors have been employed traditionally in the combustion literature [87] to specify the uncertainties on individual reaction pre-exponential constants A_r, where $F_r \equiv A_{r,\max}/A_{r,\text{nom}} \equiv A_{r,\text{nom}}/A_{r,\min}$, and the max and min values are some stated quantiles on a presumed log-normal distribution[1] for each reaction [88]. The temperature dependent $F_r(T)$ in [86] is defined similarly in terms of $k(T)$, employing 2σ quantiles. Given the paucity of data, a single functional form $F(T) = F_{300\text{K}} \exp|g \cdot (T^{-1} - 300^{-1})|$ is presumed [86], based on [89], specified with provided values for $F_{300\text{K}}$ and g for each reaction, where T is temperature in K. In principle, allowing for temperature-dependent uncertainty factors on $k(T)$ corresponds to presuming some uncertainty in the temperature exponent and/or the activation energy, aside from that in the pre-exponential. One can, indeed, use such a given $F(T)$ to constrain a presumed multivariate Gaussian on $(\ln A, E, n)$ for each reaction [90]. However, it may be argued that the correlation structure among the Arrhenius rate parameters should, in principle, be informed by available experimental data on each reaction and other experimental details, rather than a presumed functional form for $F(T)$. This concern, along with the desire to avoid tripling the dimensionality of the uncertain input space, lead to ignore the temperature dependence of the uncertainty factors in the present study. Certainly the importance of accounting for parametric correlations in chemical models is recognized, nonetheless they will be safely ignored in the present context, as further discussed in the following paragraph. Thus, a representative temper-

[1] A lognormal is presumed to ensure Arrhenius rate positivity by construction.

ature of 1500 K is picked, and the uncertainty factor is set as a constant $F \equiv F(1500\text{K})$ throughout the ignition process, based on the given $F(T)$ from [86], for each reaction. Accordingly, uncertainty is accounted for only in the pre-exponential rate constants A, and ignored in (E, n). Thus, to be precise, and in view of the earlier formulation above, the uncertain-parameter vector λ is defined as composed of the Arrhenius pre-exponential rate constants, $\lambda = (A_1, \cdots, A_M)$, where each A_r is presumed independent and lognormally distributed. The lognormal distributions are specified based on the given nominal A value and $F(1500\text{K})$ for each reaction.

Clearly, this construction, aside from ignoring the correlation among uncertain parameters (A, n, E) of each reaction, also ignores any correlation between rate parameters of different reactions. This is also the case in [86], and, in fact, in most *mechanism-scale* uncertainty analyses in the combustion literature. While examples of inferred joint densities on rates of multiple reactions [91, 92], mechanism-scale constrained parametric domains [93, 94, 95], and correlations among uncertain rates of numerous reactions [96], do exist, it is fair to say that published information on chemical kinetic mechanisms of combustion relevance never includes the specification of the joint PDF on *all* uncertain parameters in the model. Most typically, published mechanisms include only a specification of constant uncertainty factors for each reaction. Yet, correlations arise naturally from data fitting, and their importance in kinetic models is well acknowledged [97, 98, 99, 100]. When a rate constant is estimated from an experiment, where the fitting model relies on other uncertain reaction rate parameters, or, say, on uncertain thermodynamic properties, the fitting naturally induces a correlation among all these parameters. it is stress, nonetheless, that the choice in the present work, of accounting only for uncertainties in the pre-exponentials and ignoring uncertainties in (n, E) as well as correlations among rate parameters of different reactions, does not impact the generality of the strategy outlined in this study. Correlations can be easily included in future work. The present strategy for chemical model reduction under uncertainty can, indeed, employ any joint parametric PDFs where available.

5.3.1 Problem setup

The homogeneous, constant pressure, n-butane-air mixture adiabatic ignition problem is set up with a deterministic initial condition corresponding to a stoichiometric mixture at 1050 K and 1 atm. It is clear that a range of initial conditions would allow the exploration of the phase space more exhaustively, and the generation of more comprehensive simplified mechanisms, however, for now, this study is limited to one initial condition in order to emphasize the key aspects of the reduction strategy. For any given sample of λ, an ignition trajectory is computed by integrating the governing system of stiff ordinary differential equations using CVODE [36], employing TChem [37] for evaluation of chemical source terms and analytic Jacobians. Each integrated trajectory provides a database of states, based on which the CSP-based simplification method generates one simplified mechanism for each specified tolerance τ on Importance Indices. The $\boldsymbol{\tau}$ vector is defined as a uniformly-spaced list of 10 τ tolerances on Importance Indices between 0.02 and 0.27, which proved to generate a widespread family of simplified mechanisms in a preliminary deterministic analysis. The set of target species is defined as (C_4H_{10}, O_2, CO_2, H_2O, O, OH, CO). Given this setup, n random samples of λ are generated, then integration yields n ignition trajectories, producing the corresponding samples of integer vectors $\{\alpha^{\tau j}\}_{j=1}^{n}$, $\forall\tau$, used to estimate the marginal probabilities that each reaction is included in the simplified mechanisms. Finally, the proposed strategy is employed to generate simplified mechanisms for different thresholds θ on marginal probabilities. The effects of the thresholds θ are examined on the simplified mechanism and on the *a-posteriori* errors. Also, the utility of the probabilistic reduction strategy is illustrated, in particular, when employing the resulting simplified mechanisms in a deterministic prediction context, which is what a general user might be interested in.

5.3.2 Uncertain predictions of the detailed mechanism

Uncertainty in the Arrhenius parameters results in uncertain detailed autoignition trajectories as shown in Fig. 57 for select species/temperature. In these plots, the average trajectory of a species concentration/temperature is plotted against the progress variable

defined in section 5.2. Also plotted are two curves that lie ± 2 standard deviations away from the mean prediction. The choice of examining uncertain trajectories with respect to the progress variable allows to avoid artifacts associated with the fast growth of uncertainty due to small shifts of ignition time, during the ignition regime. The trajectories of temperature and O_2 (not shown) are the least affected by uncertainty among those included in the target set. Except for the fuel, which is depleted early, the largest predictive uncertainties on species concentrations occur in the proximity of $\tilde{s} = 0.9$, which represents the mixture evolution roughly halfway through the ignition.

Figure 58 shows the behavior of temperature in time for a number of samples, highlighting the variability in the ignition delay time. Note that there is no uncertainty in the equilibrium point. This is an expected result, given that equilibrium is determined by the equilibrium constants, which are sole functions of the thermodynamic properties of the mixture, that are not assumed as uncertain in this application. Thus, uncertainty appears only in the transient response. Also shown in Fig. 58 is the evolution of the progress variable $\tilde{s}$ in time for a number of samples. Its monotone and non-singular nature even when approaching equilibrium is highlighted in the box in the bottom right corner. Further, it is pointed out that, while these results, being at 1 atm, are not directly comparable to the 10 atm ignition delay results in [86], the analysis has also been run at 10 atm, arriving at a mean ignition delay time of 5.4 ms and a standard deviation of 1.1 ms, both of which are consistent with the findings in [86].

5.3.3 Monte Carlo convergence

The convergence of the Monte Carlo (MC) error is now examined to estimate the number of samples required to produce accurate enough $\{\alpha^\tau\}$ vectors. In general, for a given target accuracy, the number of required sample simulations scales with the number of important uncertain parameters, which is typically small, but is not known a-priori. The MC error in the estimation of the marginal probability of reaction r, $\mathcal{P}_r^\tau$, for any number of samples n, defined as $\varepsilon = \mathcal{P}_{r,n}^\tau - \mathcal{P}_r^\tau$ should decay as $n^{-1/2}$. The convergence rate of the error can be estimated by looking at the decay of the incremental error defined as $\epsilon_{r,n}^\tau = \mathcal{P}_{r,n}^\tau - \mathcal{P}_{r,2n}^\tau$, $r = 1, M$, for the geometric series $n = k, 2k, 4k, \dots$, given a starting sample size k. For

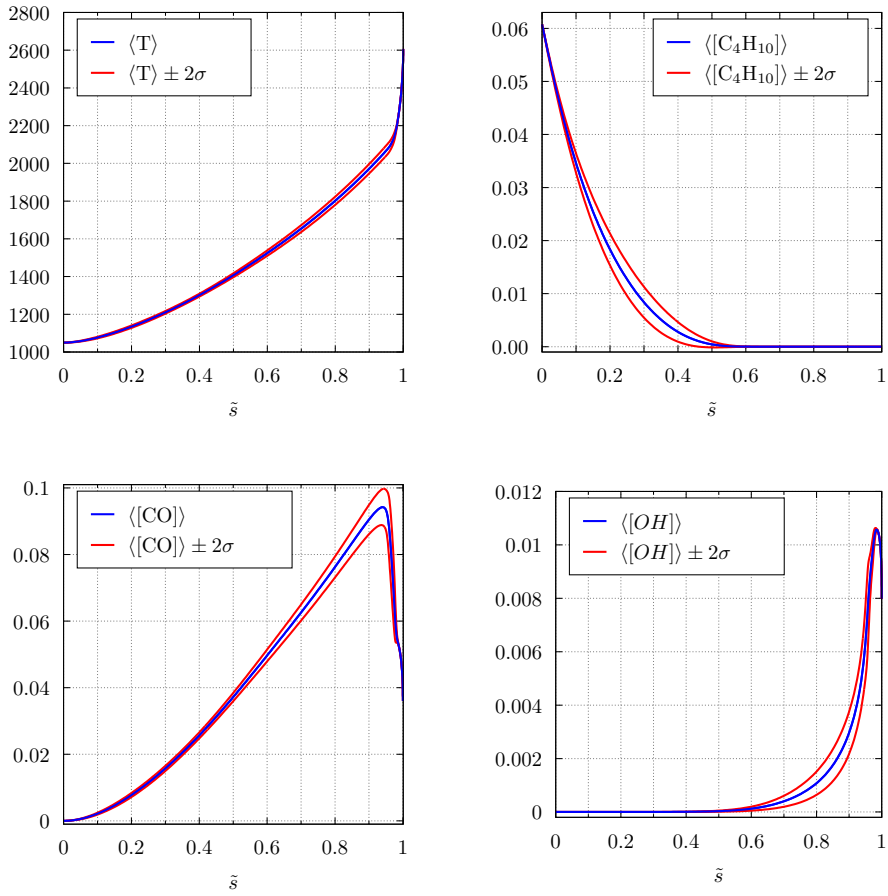

Figure 57: Average Temperature (expressed in Kelvin), C_4H_{10}, CO and OH trajectories, with 2 standard deviation bounds, plotted against the normalized mixture specific entropy $\tilde{s}$

each n, the error corresponding to equal-sized subsets of different combinations of $\{\alpha^{\tau j}\}$ realizations is computed. Figure 59 shows the scatter of the maximum MC error over the M reactions for increasing numbers of samples. The average MC error decays as $n^{-1/2}$ as expected based on the Central Limit Theorem. In what follows, $n = 10000$ samples will be employed, to keep the maximum error on statistics below 1%.

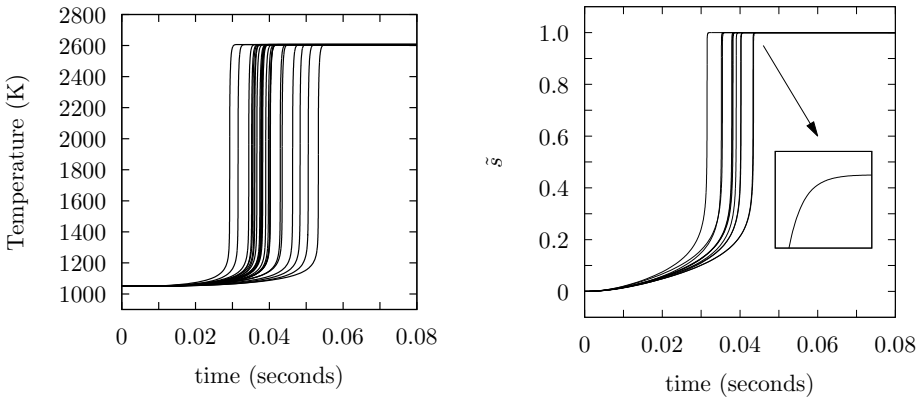

Figure 58: Temperature and normalized entropy ($\tilde{s}$) evolution in time for a number of samples, the box shows the normalized entropy evolution in time for $(1-\delta) < \tilde{s} < 1$, with $\delta \approx 10^{-3}$

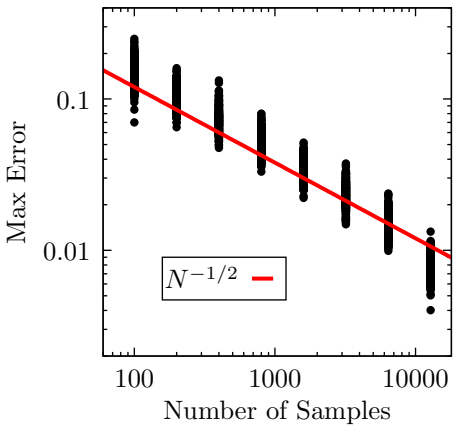

Figure 59: Self convergence of Max Error in P_α with increasing number of MC samples

5.3.4 Mechanism Simplification

Next the simplification of the uncertain n-butane-air mechanism is performed with the specified 10 τ tolerances on Importance Indices. Figure 60 shows the number of retained

species/reactions with increasing θ, for all the prescribed τ thresholds. As expected, the increase in τ acts towards a reduction in the number of species/reactions included in the simplified mechanisms. The role of θ is similar to that of τ in its consequence, namely the reduction of the retained reactions, although it operates on the probabilistic side of the analysis. In fact it deals with the probabilities of inclusion of each reaction in the reduced mechanism, given the specified parametric uncertainties in the detailed mechanism. For any fixed value of τ, and for any given reaction r, each random parameter vector sample $\lambda^{(j)}$, $j = 1, \ldots, n$, leads to a 1/0 choice on the inclusion/exclusion of this reaction, with the resulting marginal probability estimated as the sample average $\mathcal{P}_r^\tau \approx \mathcal{P}_{r,n}^\tau$. The final decision on inclusion/exclusion of reaction r then depends on θ, and specifically on whether $\mathcal{P}_r^\tau > \theta$. A low value of θ allows the inclusion of reactions that are marked

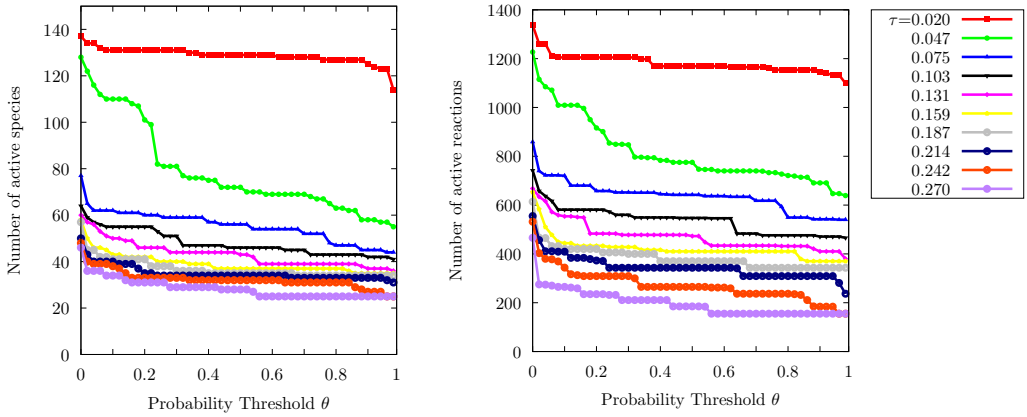

Figure 60: Number of retained/active species and reactions with increasing τ and θ

as important/included in only a minority of the samples, and thus have a relatively low inclusion probability $\mathcal{P}_r^\tau > \theta$, while for high values of θ only highly probable reactions are included. Obviously, $\theta = 1$ means that a reaction is included only if it is found to be included for *every* randomly sampled $\lambda^{(j)}$. Thus, this limit of θ would be most exclusive, resulting in the smallest set of included reactions for the given τ. On the other hand, a $\theta = 0$ allows for the inclusion of the majority of reactions, namely, any reaction that is selected for at least one sample of $\lambda^{(j)}$ is included. It is also observed that the quantitative

effect of τ in decreasing the number of retained species/reactions in this application is generally much stronger than that of θ. The maximum change in the number of retained species that has been obtained varying θ through its whole excursion range, that is from 0 to 1, is approximately 60 and happens for the case of $\tau = 0.047$ (depicted in green in Fig 60). However, in all the other τ-cases considered, the effect of θ is of the order of 20 species or less. Figure 61 shows the histogram of the probability of inclusion $\mathcal{P}_r^\tau$ for a representative choice of values for τ. As Fig.60 suggests, with the non-smooth behavior of the number of active species/reactions with increasing θ, where sudden jumps are observed together with long plateaus, $\mathcal{P}_r^\tau$ has the tendency to assume only certain values. There are wide intervals of values of $\mathcal{P}_r^\tau$ that are never taken by any reaction. For example, in the case of $\tau = 0.020$, no reactions have a probability of inclusion which falls between 0.1 and 0.3, and 0.4 and 0.6. Moreover, many reactions have a probability of inclusion which is equal, or very close to, 1. These groups of reactions are those whose relative importance is not sensitive to the uncertainty in the Arrhenius parameters and, for the given τ, will be labeled as active/included for any choice of θ. The only one case in which this behavior is less evident is again $\tau = 0.047$, where the group of reactions with $\mathcal{P}_r^\tau \approx 1$ is smaller and the histograms are more uniformly distributed. These results help to give more insight into the system's behavior when it is subject to perturbations in its parameters. For almost all the τ thresholds employed, there is a bulk of reactions that is always included in spite of the trajectories variability.

5.3.5 Error Analysis

For the *a posteriori* error analysis, 8 sets of simplified mechanisms are compared, built using 8 probabilistic thresholds θ, namely (0.1, 0.3, 0.4, 0.5, 0.7, 0.8, 0.9, 0.99), each set including 10 mechanisms with different levels of fidelity according to the τ tolerances. The probabilistic thresholds have been chosen in order to explore the most interesting $\mathcal{P}_r^\tau$ ranges based on the results showed in Fig.61.

Each simplified mechanism is identified by the pair (τ,θ) that has been used to generate it, as explained in section 5.1. Several QoIs can be drawn *a posteriori* to evaluate their degree of accuracy with respect to the detailed mechanism, as described in section 5.2.

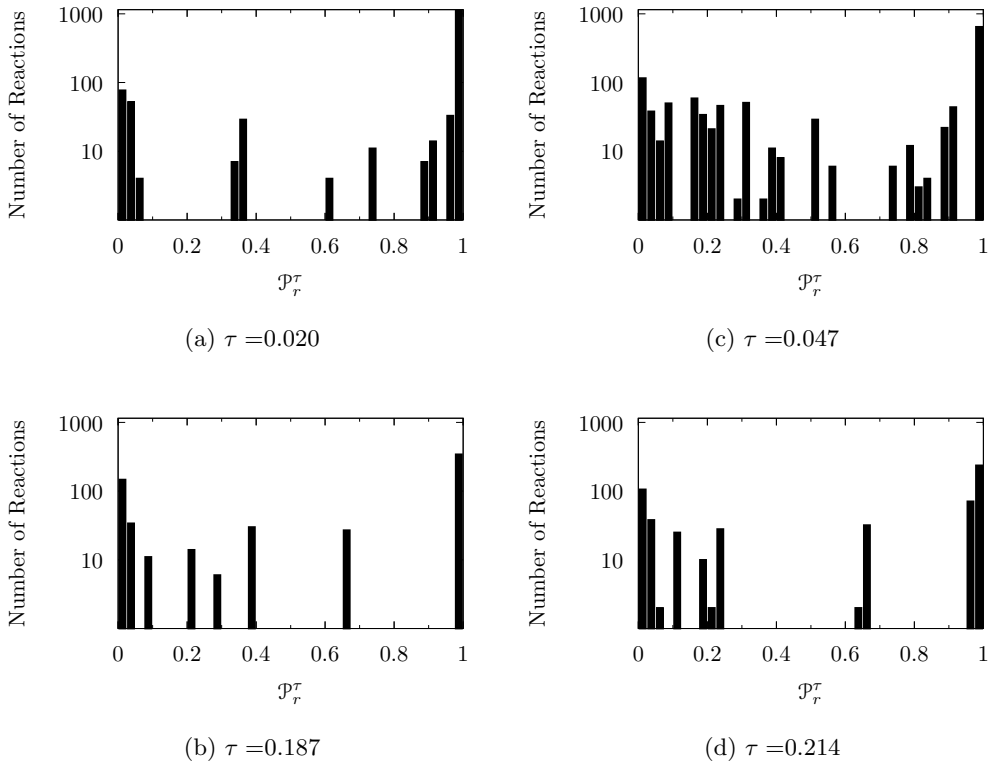

(a) τ =0.020

(c) τ =0.047

(b) τ =0.187

(d) τ =0.214

Figure 61: Histograms of the probability of inclusion $\mathcal{P}_r^\tau$ for a representative choice of values for τ.

Consider first the ignition delay time. Previous experience with deterministic chemical model analysis/reduction with CSP [54] demonstrated a general lack of monotonicity of the ignition delay time, and its error with respect to that based on the detailed mechanism, when reducing the number of species/reactions by varying the CSP threshold τ. This is found here as well. Figure 62 shows the predicted ignition delay times with their error bars, compared to the uncertain prediction based on the detailed mechanism. All the 10 sets shown, each comprising 8 mechanisms corresponding to the same τ threshold, are plotted against the number of retained species. The θ threshold increases from right to left in each set. A logarithmic scale is used in the x-axis for the sake of clarity, since the majority of the

resulting mechanisms are in the region of 30 to 60 species. As a general result, the ignition delay time remains acceptable, in both average and standard deviation, until around 60 species, then it becomes irregular, being above or below the detailed prediction, without exhibiting a monotonic tendency towards promoting or postponing the onset of ignition by eliminating species/reactions.

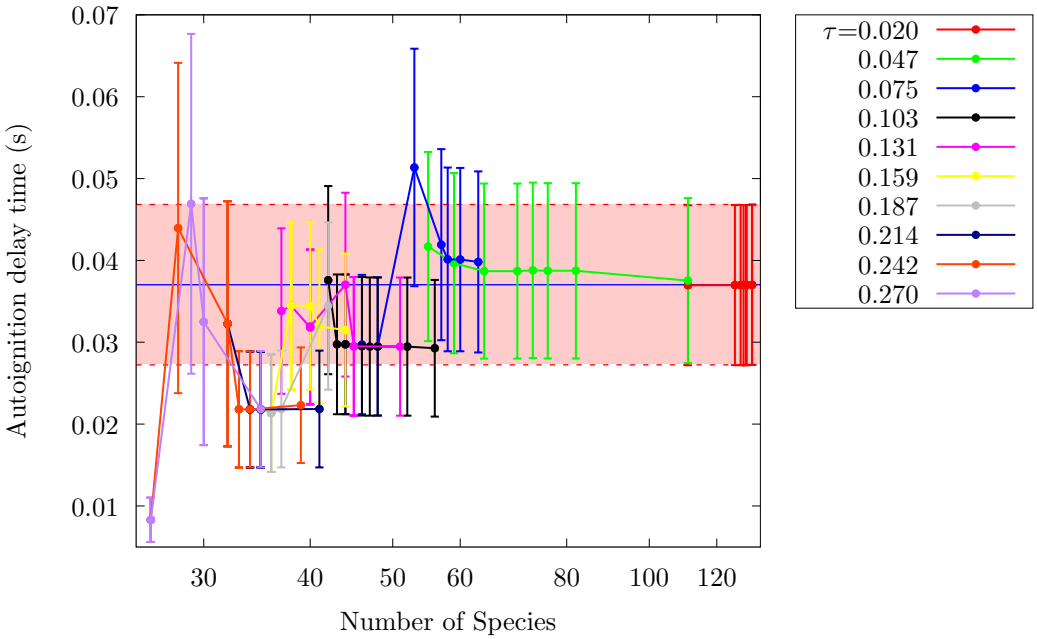

Figure 62: Ignition delay times with their error bars at 2 standard deviations, for different τ and θ thresholds, compared with the detailed mechanism-based prediction in blue with error bounds at 2 standard deviations in red. θ thresholds are parametrizing each τ-set, increasing from right to left.

A global monotonic trend is instead observed in the 95% quantiles of the distributions of the relative error between the detailed and the simplified predictions of the ignition delay time, as shown in Fig.63. The distributions are built by evaluating the relative error of each simplified mechanism-based random ignition with respect to the corresponding detailed mechanism-based ignition. As already pointed out, errors are relatively small

for mechanisms involving more than 60-species. Further, despite islands of local non-monotonicity, it can be generally said that increasing τ and/or θ leads to higher errors in ignition delay times.

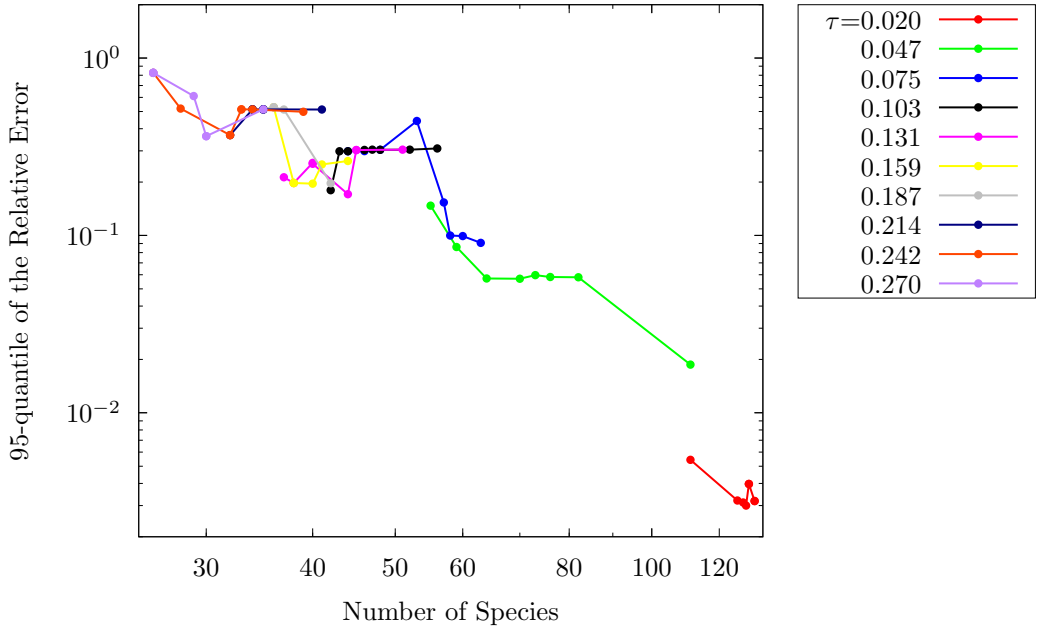

Figure 63: 95% quantiles of the distributions of the relative errors in ignition delay time against the number of retained species. θ thresholds parametrize each τ-set, increasing from right to left.

Consider next *a posteriori* errors measured by trajectory error norms. Figures 64 and 65 show the probabilistic error norms obtained as per Eqs.(5.2.5) and (5.2.6), that are averaged over the target species only. In particular, the un-weighted L_2 error in averages and standard deviations is presented, plotted against the number of species for each τ-set, parametrized with θ. In both plots, reasonably clear global trends may be seen towards higher error with increased (τ, θ). Nonetheless, local non-monotonicity is also observable in these results. Removing one reaction at a time from a chemical model, even as guided by the dynamical analysis information from CSP, does not monotonically cause increase

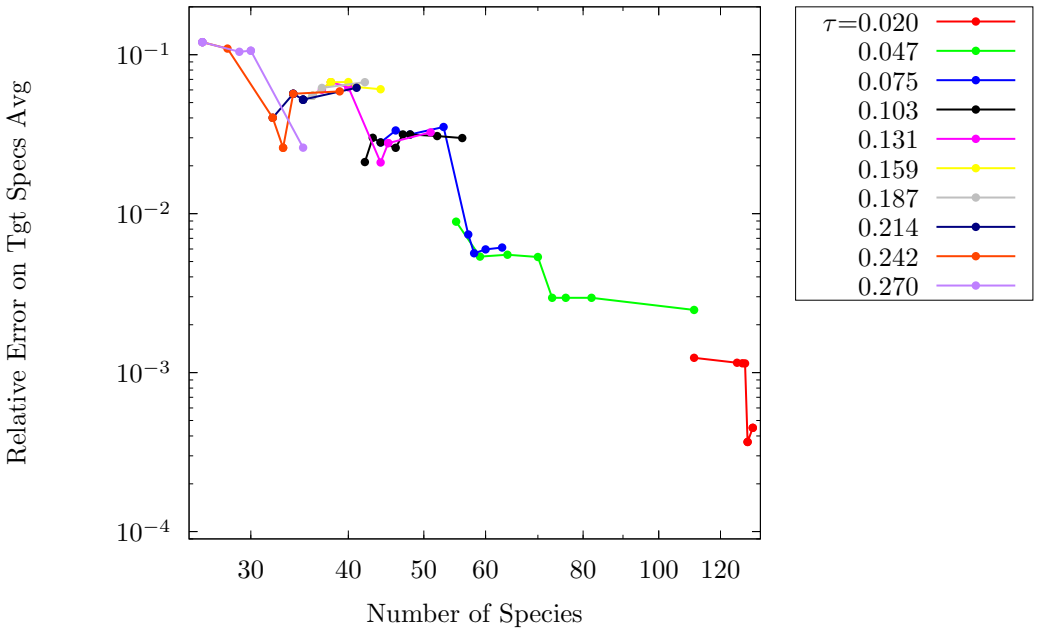

Figure 64: Average over the target species of the L_2 un-weighted relative errors of the mean transient evolution against the number of retained species. θ thresholds parametrize each τ-set, increasing from right to left.

in error. This is because of the complex network structure underlying the model. In particular, it may be imagined that removing a whole reaction sub-network can potentially provide a more physically-valid reaction mechanism than simply removing part of it.

Beside this, Figs. 64 and 65 indicate that average probabilistic errors for target species, including both means and standard deviations, are acceptable over a wide range of importance index tolerances and probabilistic thresholds. The (relative) errors in the means span roughly 0.05% to 10%, depending on (τ, θ), while those in the standard deviations are larger, spanning 0.5% to 200%. Evidently, less severe simplification can be tolerated for similar accuracy in standard deviations versus the means. Thus, larger mechanisms are necessary for capturing both predictive means and uncertainties to the same degree of accuracy. Again, mechanisms down to 60 species show acceptable error figures in both averages

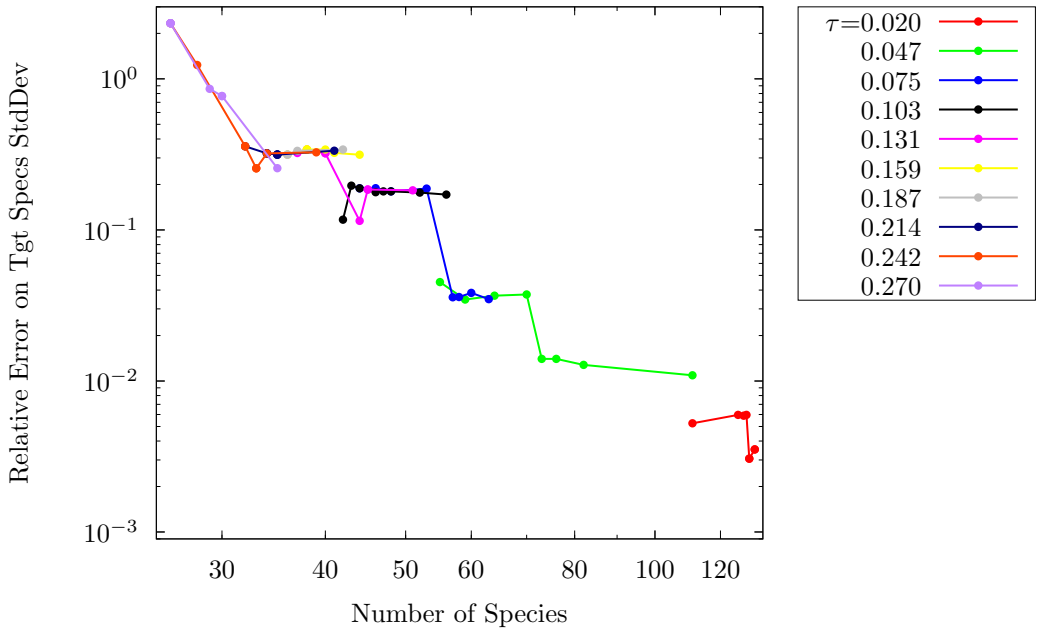

Figure 65: Average over the target species of the L_2 un-weighted relative errors of the standard deviation of the transient evolution against the number of retained species. θ thresholds parametrize each τ-set, increasing from right to left.

and standard deviation accuracy with respect to the uncertain detailed mechanism.

Also, the behavior of other norms was examined, including both weighted and unweighted L_2, L_1, and L_∞ norms. Among all these, the unweighted L_2 errors exhibited the clearest global trends in (τ,θ), hence their inclusion here. The other plots do not go against the illustrated global trends, they simply exhibit more local non-monotonicity. In particular, there is the suspect that weighted error norms exhibit higher local non-monotonicity because of the role of the weight, namely the standard deviation along the orbital predictions based on the detailed mechanism, which adds an extra level of complexity given its additional dependence on the database of solutions and sampling noise.

5.4 A motivation question

The following question is next considered: what is the advantage that a general user, who might not be necessarily interested in uncertain predictions but rather in deterministic predictions from robust reduced mechanisms, can derive from the use of a simplified mechanism generated through the proposed probabilistic approach. A general user would choose the suitable simplified mechanism for his/her applications by trading off accuracy for improvements in computational costs, *i.e.* a lower number of retained species/reactions. It is presumed that he/she are further interested in ensuring some degree of robustness in the simplified model, in that its deterministic prediction is within requisite thresholds with sufficiently high probability, given the existing uncertainties in the detailed mechanism. However, again, he/she would employ this simplified mechanism in a deterministic context, that is by setting the uncertain parameters to the nominal values. It will be illustrated below that the uncertainty-based construction of the simplified mechanisms ensure that, even when the mechanism is employed with nominal parameters, it has a lower probability of violating its presumed error thresholds, in comparison to the alternative option of deterministic reduction ignoring uncertainty.

In a general setting, let $y = f(\lambda)$ be the detailed forward model, where λ is a vector of random variables having a joint distribution p_λ, whose nominal values are λ_0. Two possible approaches are recognized to obtain a simplified forward model. The first one is the deterministic approach for which the simplified model is a function of the nominal value of the uncertain parameter:

$$\tilde{y} = g(\lambda_0) \tag{5.4.1}$$

The simplified model $g(\lambda_0)$ is chosen *a-posteriori*, based on an error requirement of the kind:

$$E_1 = \|g(\lambda_0) - f(\lambda_0)\| < \epsilon \tag{5.4.2}$$

where ϵ is a user-defined error threshold.

The issue with this approach is that it might lead to underestimating the error with respect to reality, if λ is in fact uncertain, and it happens that the true value of λ is quite

different from λ_0. In fact, if the "true" value of λ is $\lambda^\star$, and defining:

$$E_2 = \|g(\lambda_0) - f(\lambda^\star)\| \tag{5.4.3}$$

there is the possibility that $E_2 > \epsilon > E_1$, which means that the simplified model $g(\lambda_0)$ can be farther from reality than the user intended by the ϵ-certification, with some probability.

Clearly, the value $\lambda^\star$ is not known. However, given the uncertain λ, modeled as a random variable, it holds that $E_2(\lambda) = \|g(\lambda_0) - f(\lambda)\|$ is a random variable, and the deterministically reduced model $g(\lambda_0)$ has a certain probability of missing the threshold of error (ϵ) that the user tried to enforce. In other words, predictions with $g(\lambda_0)$ produce an actual error $E_2(\lambda)$ relative to the detailed model where the probability $P[E_2(\lambda) > \epsilon] > 0$.

In contrast, the approach presented in this paper considers λ as a random variable up-front and generates probabilistic simplified models of the kind:

$$\hat{y} = h(\lambda) \qquad\qquad \lambda \sim p_\lambda \tag{5.4.4}$$

The simplified model is chosen *a-posteriori*, based on probabilistic error constraints such as those defined in section 5.2, that treat the models in a probabilistic framework, *i.e.* by comparing averages and standard deviations, or by building probabilistic distributions of the predictions. However, a general user would presumably employ this model for deterministic predictions. In this case:

$$\hat{y}_0 = h(\lambda_0) \tag{5.4.5}$$

and the error between this model and reality is:

$$E_3^* = \|h(\lambda_0) - f(\lambda^\star)\| \tag{5.4.6}$$

Again, given that the true $\lambda^\star$ is unknown, it is possible to employ only

$$E_3(\lambda) = \|h(\lambda_0) - f(\lambda)\|, \tag{5.4.7}$$

which is a random variable. It will be shown in the following that

$$P[E_2(\lambda) > \epsilon] \;>\; P[E_3(\lambda) > \epsilon]. \tag{5.4.8}$$

This means that the mechanisms generated with our probabilistic approach have a lower chance of missing the user-enforced threshold ϵ when compared against an uncertain detailed mechanism, even if employed with nominal uncertain parameters, with respect to the mechanisms generated ignoring the uncertainty.

Figure 66a shows the PDF of $E_3(\lambda)$ for one of the obtained simplified mechanisms, together with its error certification ϵ, already presented in Fig.64. $E_3(\lambda)$ is calculated in the $\{\psi, X_i\}$ phase space and is averaged over the target species only. The probability of missing the error certification is as low as 8%. On the contrary, the PDF in Fig.66b is the PDF of $E_2(\lambda)$ for a simplified mechanism generated with a classical, non-probabilistic, method, that has a similar error certification ϵ, enforced on classical, deterministic, error figures. The probability of missing the error-certification is as high as 75%. This result, indicating the improved robustness in the deterministic predictions from the mechanisms developed with the present strategy, appears systematically for all the obtained simplified mechanisms.

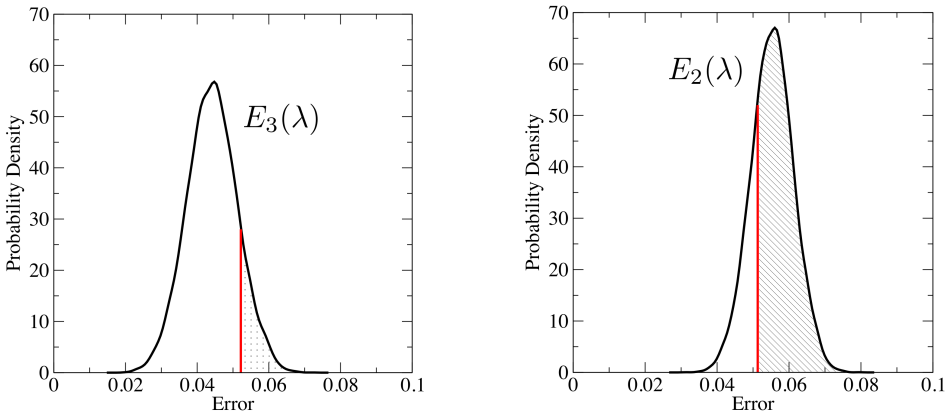

(a) $E_3(\lambda)$ (b) $E_2(\lambda)$

Figure 66: PDF of $E_3(\lambda)$ for one of the probabilistically generated simplified mechanisms, and PDF of $E_2(\lambda)$ for a non-probabilistically generated simplified mechanism, with their error certification in the $\{\psi, X_i\}$ space (ϵ, both in red). The highlighted areas are $P[E_3(\lambda) > \epsilon]$ and $P[E_2(\lambda) > \epsilon]$

5.5 Conclusions and future work

A general strategy for analysis and reduction of uncertain chemical kinetics models was proposed, adopting an existing reduction method, based on computational singular perturbation (CSP) analysis, as a deterministic tool through which the uncertainty in the Arrhenius pre-exponential rate constants of the reference model is propagated to obtain the marginal probability of inclusion in the reduced model of each reaction. The simplified mechanisms are built by including those reactions whose marginal probability is higher than a given threshold. Probabilistic error measures were defined to assess the performance of such simplified mechanisms taking uncertainty into account. The utilization of this strategy was demonstrated presenting an application where the uncertain kinetic model for the oxidation of n-butane was simplified based on different thresholds on marginal probabilities and several levels of accuracy determined by a number of tolerances on the reactions Importance Indices. The probabilistic error figures for the obtained simplified mechanisms were shown, highlighting the global trends of errors when varying probabilistic thresholds and tolerances on Importance Indices, and discussed some local non-monotonic behaviors of the errors that come from the complex way in which a given reaction mechanism/network performs when removing reactions/species. Also, the utility of the probabilistic reduction strategy was illustrated for the general user who may be simply interested in *robust* deterministic predictions, showing that tight error tolerances enforced on simplified models obtained with deterministic approaches have a high probability of being missed because of the uncertainty in the detailed model.

Ongoing work will further explore the various numerical and statistical aspects of the construction, focusing on its capabilities for examining the joint probability of sets of reaction. Additional detailed comparisons between deterministic and probabilistic analysis strategies will also be explored, outlining further the utility of the present construction for identifying robust simplified models that are certifiably accurate over stated ranges of uncertainty.

Chapter 6

Conclusions and future works

With the aim of improving the understanding of combustion phenomena, in the era of complex numerical experiments, the computational singular perturbation (CSP) method was invoked as the cornerstone of a general framework for the analysis of chemical kinetics systems. The essence of the CSP method was shown to lie in the ability to project the chemical source term on a special basis, where each mode evolves independently according to its own time scale, and to decompose the tangent space into fast and slow subspaces. This new representation in terms of modes allows to exploit a large number of features of the dynamical system that otherwise would have been hidden by the system's coupling. Among them, the identification of the exhausted time scales lays the foundations for deriving reduced models, since the system approaches a low dimensional manifold where it evolves according to the slow scales, and for characterizing the species involved as slow or radicals. The CSP framework was then extended to non-homogeneous problems, where kinetics is challenged by transport. The proposed approach considers transport as a process that affects the amplitudes of the kinetic modes, but not the structure of the modes themselves.

Once the CSP framework was set up, a number of CSP-based tools were introduced to get *a-posteriori* information and physical insights on combustion problems involving

complex kinetic schemes and/or interaction between chemistry and transport. The CSP participation indices were introduced to quantify the contribution of a chemical reaction to a mode, rediscovering the link between the CSP modal representation and the system's physical meaning. The indices were employed in a simple application to detect the reactions contributing to unusually fast modes, which appeared in the context of homogeneous auto-ignitions where very large mechanisms were employed to describe chemistry. Such mechanisms, needed to model today's complex fuels, are developed with automated procedures and designed to match certain thermo-physical properties of fuel blends. They typically include thousands of species, and are inclined to develop unphysically small timescales. The CSP framework proved to be a valuable choice for addressing such kind of problems.

Another participation index was then defined, combining the CSP concepts with the definition of entropy and its time variation, allowing to expand the CSP framework. The entropy participation index quantifies the contribution of a reaction to the entropy production, in either the fast or slow subspace, and is perfectly suitable for identifying the dominating chemical processes in the system's dynamics. Also, the exhausted timescales criterion was reformulated in terms of entropy production, exploiting the idea that there is no entropy produced by the fast subspace.

In the context of CSP-based tools for system's diagnostics, the real breakthrough was represented by the tangential stretching rate (TSR). The TSR is the most energy containing chemical time scale, being a weighted average of the system's eigenvalues, where the weights depend on the amplitudes of the modes and their degree of colinearity with the vector field. Based on the sign and value of the TSR, one may employ it to characterize the system's dynamics in terms of: (i) explosive/dissipative nature, (ii) truly active chemical time scale, (iii) chemical reactions participating to the most energy containing modes. Moreover, the TSR extension to non-homogeneous systems was presented, introducing additional features that allow to determine whether the dynamics is kinetic- or transport-controlled, *i.e.* distinguish between auto-ignition and deflagration.

Three TSR applications were shown. First, a homogeneous hydrogen/air auto-ignition, where TSR was employed to identify the dominant chemical processes, distinguishing between below- and above-crossover behavior, which are two different ignition paths whose

activation depends on the initial temperature/pressure of the mixture. A simple criterion involving TSR participation indices was also shown to fairly identify the crossover initial temperature. Second, the analysis of a 1-D unsteady non-premixed flame was performed. The comparison between TSR and extended TSR allowed to get deep physical insights on the flame behavior and to define the flame topology according to the dynamic's nature. In particular, the flame front region was identified and its auto-igniting/deflagrating character was ascertained, as long as its dominant chemical and physical processes. Lastly, the DNS of a turbulent 3-D premixed flame was analyzed, highlighting the most natural way to employ the TSR, *i.e.* to get fundamental understanding of large and complex fields.

Next, the second main feature available in the CSP framework was exploited: the mechanism simplification. A well established algorithm was recalled, which relies on the CSP importance indices, employed to quantify the contribution of a reaction to the production/consumption of a species, and which selects the reactions mostly involved - more than a tolerance - in the dynamics of a set of species of interest. The pivotal tasks of a simplification campaign were described, highlighting the importance of correctly choosing a representative dataset to be fed to the algorithm.

Three improvements to the algorithm were then presented, involving entropy participation indices, TSR, and a variable tolerance approach. The advantages and disadvantages of the three were revealed in a practical application, where a skeletal mechanism valid for ethylene-air mixtures was obtained from the detailed KAUST-Aramco PAH mechanism. In particular, the combination of TSR and variable tolerance approach was shown to get the best results in terms of number of retained species and ability of replicating the behavior of the species of interest, which included the PAHs.

The simplification strategy was then extended to steady-state reactive-diffusive problems and an application to HTPB hybrid rocket combustion was performed. The campaign allowed to obtain families of skeletal mechanisms, ranging from 17 to 40 species, that accurately replicated the butadiene-oxygen combustion in a flamelet model, representative of the hybrid rocket combustion processes.

Lastly, the model reduction strategy was discussed again taking the uncertainty in the model parameters under consideration. Overconfidence in the model parameters, in fact, can lead to a misplaced focus on tight error tolerances in the simplified model, when the baseline, *i.e.* the detailed model, is faulty because affected by uncertainty. Typical uncertain parameters are the Arrhenius rate coefficients. A novel CSP simplification strategy under uncertainty was presented, and adequate error measures were introduced to compare simplified and detailed models in a probabilistic setting. The simplified mechanisms are built by retaining those reactions whose marginal probability is higher than a given threshold. An application to a uncertain n-butane kinetic model was performed, demonstrating the utilization of the strategy and its utility for a general user who may be simply interested in robust deterministic predictions.

Despite the efforts made in building a versatile framework for model reduction and system's diagnostics, much remains to be done and a number of questions still remain open. In example, further developments will be required to extend the CSP diagnostics to filtered datasets, such as those obtained with LES simulations. The correct way to employ CSP would be to analyze the sub-grid scale value of the reactive scalars. The way to access the sub-grid scale values varies with the turbulence-chemistry model employed and the effect of this reconstruction requires deeper inspection. Also, the validity of the CSP diagnostics is still to be fully understood in the case of steady-state problems, where either the chemical source term in the homogeneous case, or the sum of chemical source term and transport term(s) in non-homogeneous cases, is zero. In the latter case, as it has been shown in the steady-state reactive-diffusive system simplification, the chemical source term, which is non-zero because it balances transport, is the only entity that can be investigated.

The model reduction side of the CSP framework is more consolidated, as long as uncertainty is not taken into account. The presence of uncertainty opened a wide spectrum

of questions, a very small number of which has been tackled in this work. Very few words were spent from the chemical kinetics point of view on the impact of uncertainty on groups of reactions, that are or are not included together. This consideration extends the strategy from using marginal probabilities to two-way probabilities of inclusion, and even to joint probabilities of an entire sub-mechanism.

Most of the perspectives outlined above are part of ongoing work and will hopefully contribute to the consolidation of this small brick in the combustion knowledge wall.

Appendix A

Model problems

A.1 Homogeneous reactor model

The set of ODEs describing the time evolution of a mixture of ideal gases contained in a batch reactor (at constant pressure) is

$$\begin{aligned} \frac{\mathrm{d}Y_j}{\mathrm{d}t} &= \frac{1}{\rho} W_j \, \dot{\omega}_j \left(T, p, Y_i\right), \qquad i, j = 1, \ldots, N, \\ \frac{\mathrm{d}T}{\mathrm{d}t} &= -\frac{1}{\rho \, C_p} \sum_{j=1}^{N} h_j(T) \, W_j \, \dot{\omega}_j \left(T, p, Y_i\right), \end{aligned} \tag{A.1.1}$$

where T and Y_j are the temperature and composition (expressed in terms of mass fractions) of the mixture, t is time, ρ is the mixture density, C_p is the mixture mean heat capacity at constant pressure per unit mass, N is the number of species, h_j is the species enthalpy per unit mass, W_j is the species molecular weight, and $\dot{\omega}_j$ is the molar rate of formation/destruction of the j-th species. The set of ODEs is closed by the thermal equation of state for a mixture of ideal gases

$$p = \rho \, R \, T, \tag{A.1.2}$$

where p is the pressure in the reactor vessel, $R = \sum_{j=1}^{N} R_j Y_j$ is the mixture's gas constant, and the mixture specific heat which can be expressed as

$$C_p\left(T, Y_j\right) = \sum_{j=1}^{N} C_{p,j}(T)\, Y_j, \tag{A.1.3}$$

where $C_{p,j}(T)$ is the heat capacity at constant pressure per unit mass of the j-th species.

The customary relations between mass fractions Y_j, molar fractions X_j, and molar concentrations c_j read:

$$c_j = \rho\, \frac{X_j}{\overline{W}} = \rho\, \frac{Y_j}{W_j}, \tag{A.1.4}$$

where $\overline{W} = \sum_{j=1}^{N} W_j\, X_j$ is the mean molecular weight of the mixture. The molar rate of formation/destruction of the j-th species due to the K reactions reads:

$$\frac{dc_j}{dt} = \dot{\omega}_j\left(T, p, Y_j\right) = \sum_{k=1}^{K} \Delta\nu_{j,k}\, r^k\left(T, p, Y_i\right), \tag{A.1.5}$$

where $\Delta\nu_{j,k} = \Delta\boldsymbol{\nu}_k = \boldsymbol{\nu}_k^{''} - \boldsymbol{\nu}_k^{'}$ is the net stoichiometric coefficient, and $\boldsymbol{\nu}_k^{'} = \nu_{j,k}^{'}$ and $\boldsymbol{\nu}_k^{''} = \nu_{j,k}^{''}$ are the forward and reverse stoichiometric coefficients of the j-th species in the k-th reaction. The net rate of the k-th reaction reads:

$$\begin{aligned} r^k\left(T, p, Y_j\right) = \; & r_f^k - r_b^k = K_f^k \prod_{j=1}^{N} c_j^{\boldsymbol{\nu}_k^{'}} - K_b^k \prod_{j=1}^{N} c_j^{\boldsymbol{\nu}_k^{''}} = \\ & K_f^k \prod_{j=1}^{N} \left(\rho\, \frac{Y_j}{W_j}\right)^{\boldsymbol{\nu}_k^{'}} - K_b^k \prod_{j=1}^{N} \left(\rho\, \frac{Y_j}{W_j}\right)^{\boldsymbol{\nu}_k^{''}} = \\ & K_f^k \prod_{j=1}^{N} \left(\frac{p}{RT}\, \frac{Y_j}{W_j}\right)^{\boldsymbol{\nu}_k^{'}} - K_b^k \prod_{j=1}^{N} \left(\frac{p}{RT}\, \frac{Y_j}{W_j}\right)^{\boldsymbol{\nu}_k^{''}}, \end{aligned} \tag{A.1.6}$$

where r_f^k and r_b^k are the forward and backward reaction rates, and K_f^k and K_b^k are the forward and backward reaction constants, which depend exponentially on temperature according to the standard Arrhenius form.

Often, a N-long column vector $\boldsymbol{S}_k$ of the net stoichiometric coefficients is defined as:

$$\boldsymbol{S}_k := \Delta\nu_{j,k} \tag{A.1.7}$$

so that the molar rate of formation/destruction can be expressed as:

$$\frac{dc_j}{dt} = \dot{\omega}_j(T, p, Y_j) = \sum_{k=1}^{N_r} \boldsymbol{S}_k r^k. \tag{A.1.8}$$

If we define the state of the system as the algebraic vector with the corresponding vector field as

$$\boldsymbol{x} = \{Y_j, T\} \quad \text{and} \quad \boldsymbol{g}\,(Y_j, T) = \left\{ \frac{W_j\,\dot{\omega}_j\,(T, p, Y_i)}{\rho}, -\frac{1}{\rho\,C_p}\sum_{j=1}^{N} h_j\,W_j\,\dot{\omega}_j\,(T, p, Y_i) \right\}, \quad \text{(A.1.9)}$$

where the pressure p is a prescribed constant value, we can recast Eq. (A.1.1) as a dynamical system whose time evolution from time $t = 0$ to $t = t_{max}$ is obtained by solving the following initial value problem

$$\frac{\mathrm{d}\boldsymbol{x}}{\mathrm{dt}} = \boldsymbol{g}(\boldsymbol{x}), \qquad \boldsymbol{x}(0) = \boldsymbol{x}_0, \qquad \text{with}$$

$$\boldsymbol{x} \in \mathbb{R}^{N+1},\ \mathrm{t} \in (0, t_{max}) \subset \mathbb{R},\ \text{and}\ \boldsymbol{g} : C \subset \mathbb{R}^{N+1} \to \mathbb{R}^{N+1}. \quad \text{(A.1.10)}$$

where C is a compact set.

A.2 Laminar flamelet model

By defining the mixture fraction according to Bilger [101], the flamelet equations describe the balance of reactive and diffusive processes in a non-premixed system. Using unity Lewis number assumption [50], the species and temperature source terms read:

$$\dot{\omega}_\alpha = -\frac{1}{2}\rho\chi\frac{\partial^2 Y_\alpha}{\partial z^2}, \qquad \dot{\omega}_T = -\frac{1}{2}\rho\chi\Big[\frac{\partial^2 h}{\partial z^2} + \sum_{\alpha=1}^{N} h_\alpha \frac{\partial^2 Y_\alpha}{\partial z^2}\Big], \quad \text{(A.2.1)}$$

where ρ is the mixture density, χ is the scalar dissipation rate, Y_α are the species mass fractions, h and h_α are the mixture and $\alpha-$th species sensible enthalpies respectively.

The comparison of Eq.(A.2.1) with Eq.(4.4.1) allows to establish that the state vector $\boldsymbol{y}$ is equal to $\boldsymbol{y} := (T, \mathbf{Y}_\alpha)$, so that its dimension is $N + 1$. Moreover, the space operator $\boldsymbol{L}_x(\boldsymbol{y})$ can be defined as:

$$\boldsymbol{L}_\xi(T, Y_\alpha) := \left(\frac{1}{2}\chi\left(\frac{\partial^2 T}{\partial \xi^2} + \frac{1}{c_p}\frac{\partial c_p}{\partial \xi}\frac{\partial T}{\partial \xi}\right), \frac{1}{2}\chi\frac{\partial^2 Y_\alpha}{\partial \xi^2}\right), \quad \text{(A.2.2)}$$

and finally the source term $\boldsymbol{g}(\boldsymbol{y})$ can be defined as:

$$\boldsymbol{g}(T, Y_\alpha) := \left(\frac{\dot{\omega}_T}{c_p\rho}, \frac{\dot{\omega}_\alpha}{\rho}\right). \quad \text{(A.2.3)}$$

The flamelet equations are derived assuming the pressure p being constant in the mixture fraction space. The diffusive term represents, in the mixture fraction space, the effect of the fluid dynamic mixing and strain onto the chemical processes. The intensity of this effect is regulated by the scalar dissipation rate $\chi = \left(\frac{\partial z}{\partial x_i}\right)^2$. The response of the flamelet solution to changes in χ is well-known and consists in the departure from chemical equilibrium [50]. Indeed maximum temperature decreases with increasing χ and for large enough values of χ, quenching occurs. This behavior is classically represented by the S-shape diagram, which summarizes all the possible steady state solutions of the flamelet equations [50] [102].

Bibliography

[1] L.A.Segel, M.Slemrod, The quasi steady state assumption: a case study in perturbation., SIAM Rev. 31 (1989) 446–447.

[2] A.N.Yannacopoulos, A.S.Tomlin, J.Brindley, J.H.Merkin, M.J.Pilling., The error of the quasi steady state approximation in spatially distributed systems., Chem. Phys. Lett. 248 (1996) 63–70.

[3] M.D.Smooke, Reduced kinetic mechanisms and asymptotic approximations for methane-air flames., Vol. 348, 1991.

[4] U.Maas, S.B.Pope, Implementation of simplified chemical kinetics based on intrinsic low-dimensional manifolds, in: Twenty-Fourth Symposium (International) on Combustion, The Combustion Institute, 1992, pp. 103–112.

[5] U.Maas, S.B.Pope, Simplifying chemical kinetics: Intrinsic low dimensional manifolds in composition space, Combustion and Flame 88 (1992) 239–264.

[6] M.R.Roussel, S.J.Fraser, Invariant manifold methods for metabolic model reduction., Chaos 11 (1) (2001) 196.

[7] M.R.Roussel, S.J.Fraser, Geometry of the steady-state approximation. perturbation and accelerated convergence method., J. Chem. Phys. 93 (1990) 1072.

[8] M.R.Roussel, S.J.Fraser, On the geometry of transient relaxation., J. Chem. Phys. 94 (1991) 7106.

[9] S.J.Fraser, The steady state and equilibrium approximations: a geometrical picture., J. Chem. Phys. 88 (8) (1988) 4732–4738.

[10] S. H. Lam, D. A. Goussis, Understanding complex chemical kinetics with computational singular perturbation, Proc. Comb. Inst. 22 (1988) 931–941.

[11] S. H. Lam, D. A. Goussis, Conventional Asymptotics and Computational Singular Perturbation for Simplified Kinetics Modelling, in: M. Smooke (Ed.), Reduced Kinetic Mechanisms and Asymptotic Approximations for Methane-Air Flames, no. 384 in Springer Lecture Notes, Springer Verlag, 1991, Ch. 10, pp. 227–242.

[12] S. H. Lam, D. A. Goussis, A study of homogeneous methanol oxidation kinetic using csp, Proc. Comb. Inst. 24 (1992) 113–120.

[13] S. H. Lam, Using CSP to Understand Complex Chemical Kinetics, Combustion Science and Technology 89 (1993) 375–404.

[14] J.Warnatz, U.Maas, R.W.Dibble, Combustion: Physical and Chemical Fundamentals, Modeling and Simulation, Experiments, Pollutant Formation, Springer-Verlag, Berlin, 1996.

[15] J.H.Seinfeld, S. Pandis, "Atmospheric Chemistry and Physics: From Air Pollution to Climate change", Wiley, New York, 1998.

[16] J.Monod, J.Wyman, J.P.Changeux, On the nature of allosteric transitions: A plausible model, J. Mol. Biol 12.

[17] F. Creta, Computational methods in chemical kinetics reduction and analysis for combustion modeling and applications to hydrocarbon systems, Ph.D. thesis, Sapienza Università di Roma (2005).

[18] T.F.Lu, C.K.Law, A directed relation graph method for mechanism reduction., Proceedings of the Combustion Institute 30 (2005) 1333–1341.

[19] A. B. Bendtsen, P. Glarborg, K. Dam-Johansen, Visualization methods in analysis of detailed chemical kinetics modelling, Computers and Chemistry 25 (2001) 161–170.

[20] W. Sun, Z. Chen, X. Gou, Y. Ju, A path flux analysis method for the reduction of detailed chemical kinetic mechanisms, Combustion and Flame 157 (2010) 1298–1307.

[21] D. A. Goussis, Quasi steady state and partial equilibrium approximations: their relation and their validity, Combustion Theory and Modelling 16 (5) (2012) 869–926.

[22] A. Adrover, F. Creta, M. Giona, M. Valorani, V. Vitacolonna, Natural tangent dynamics with recurrent biorthonormalizations: A geometric computational approach to dynamical systems exhibiting slow manifolds and periodic/chaotic limit sets, Physica D 213 (2006) 121–146.

[23] M. Valorani, F. Creta, D. A. Goussis, J. C. Lee, H. N. Najm, An Automatic Procedure for the Simplification of Chemical Kinetics Mechanisms based on CSP, in: K. Bathe (Ed.), Computational Fluid and Solid Mechanics 2005, Elsevier Science, 2005, pp. 900–904.

[24] M. Valorani, H. N. Najm, D. A. Goussis, CSP analysis of a transient flame-vortex interaction: Time scales and manifolds, Combustion and Flame 134 (1-2) (2003) 35–53. doi:10.1016/S0010-2180(03)00067-1.

[25] D. A. Goussis, M. Valorani, F. Creta, H. N. Najm, Reactive and reactive-diffusive time scales in stiff reaction-diffusion systems, Progress in Computational Fluid Dynamics, An International Journal 5 (6) (2005) 316.

[26] M. Valorani, H. Najm, D. Goussis, CSP Analysis of a Transient Flame-Vortex Interaction: Time Scales and Manifolds, Combustion and Flame 134 (1-2) (2003) 35–53.

[27] A. Adrover, F. Creta, M. Giona, M. Valorani, Stretching-based diagnostics and reduction of chemical kinetic models with diffusion, Journal of Computational Physics 226 (2) (2007) 1442–1471.

[28] M. Valorani, S. Paolucci, E. Martelli, T. Grenga, P. P. Ciottoli, Dynamical system analysis of ignition phenomena using the Tangential Stretching Rate concept, Combustion and Flame 162 (8) (2015) 2963–2990.

[29] M. Valorani, P. P. Ciottoli, R. Malpica Galassi, Tangential stretching rate (TSR) analysis of non premixed reactive flows, Proceedings of the Combustion Institute 36 (1) (2017) 1357–1367.

[30] J. Prager, H. Najm, M. Valorani, D. Goussis, Structure of n-Heptane/Air Triple Flames in Partially-Premixed Mixing Layers, Combustion and Flame 158 (2011) 2128–2144.

[31] S. Gupta, H. G. Im, M. Valorani, Analysis of n-heptane auto-ignition characteristics using computational singular perturbation, Proceedings of the Combustion Institute 34 (1) (2013) 1125–1133.

[32] A. Tomlin, T. Turànyi, Analysis of kinetic reaction mechanisms, Springer, 2014.

[33] G. Blanquart, P. Pepiot-Desjardins, H. Pitsch, Chemical mechanism for high temperature combustion of engine relevant fuels with emphasis on soot precursors, Combustion and Flame 156 (3) (2009) 588–607.

[34] W. Metcalfe, S. M. Burke, S. S. Ahmed, H. J. Curran, A hierarchical and comparative kinetic modeling study of c1-c2 hydrocarbon and oxygenated fuels, International Journal of Chemical Kinetics 45 (2013) 638–675.

[35] CSPTk - a software toolkit for the csp and tsr analysis of kinetic models and the simplification and reduction of chemical kinetics mechanisms.

[36] S. D. Cohen, A. C. Hindmarsh, CVODE, a Stiff/Nonstiff ODE Solver in C, Comput. Phys. 10 (2) (1996) 138–143.

[37] C. Safta, H. N. Najm, O. M. Knio, TChem - a software toolkit for the analysis of complex kinetic models, Sandia Report SAND2011-3282, http://www.sandia.gov/tchem.

[38] M. Valorani, S. Paolucci, P. P. Ciottoli, R. Malpica Galassi, Entropy production and timescales, Combustion Theory and Modelling 21 (1) (2017) 137–157.

[39] T. Lu, C. Yoo, J. Chen, C. Law, Three-dimensional direct numerical simulation of a turbulent lifted hydrogen jet flame in heated coflow: A chemical explosive mode analysis, Journal of Fluid Mechanics 652 (2010) 45–64.

[40] M. Valorani, S. Paolucci, The G-Scheme: A framework for multi-scale adaptive model reduction, Journal of Computational Physics 228 (13) (2009) 4665–4701.

[41] J. Li, Z. Zhao, A. Kazakov, M. Chaos, F. L. Dryer, J. J. J. Scire, A comprehensive kinetic mechanism for co, ch2o, ch3oh combustion, International Journal of Chemical Kinetics 39 (2007) 109–136.

[42] P. Boivin, C. Jimenez, A. L. Sànchez, F. A. Williams, An explicit reduced mechanism for H_2–air combustion, Proceedings of the Combustion Institute 33 (1) (2011) 517–523.

[43] P. Boivin, A. L. Sànchez, F. A. Williams, Explicit analytic prediction for hydrogen–oxygen ignition times at temperatures below crossover, Combustion and Flame 159 (2) (2012) 748–752.

[44] C. Trevino, Ignition phenomena in H_2-O_2 mixtures, Progress in Astronautics and Aeronautics, AIAA 131 (1991) 19–43.

[45] P. Boivin, A. L. Sànchez, F. A. Williams, Analytical prediction of syngas induction times, Combustion and Flame 176 (2017) 489–499.

[46] P. Pal, A. B. Mansfield, M. S. Wooldridge, H. G. Im, Characteristics of Syngas Auto-ignition at High Pressure and Low Temperature Conditions with Thermal Inhomogeneities, Combustion Theory and Modelling 66 (5) (2015) 1–4.

[47] H. G. Im, P. G. Arias, S. Chaudhuri, H. A. Uranakara, Direct numerical simulations of statistically stationary turbulent premixed flames, Combustion Science and Technology 188 (8) (2016) 1182–1198.

[48] P. Arias, H. Uranakar, S. Chaudhuri, H. Im, Direct numerical simulations of flow-chemistry interactions in statistically turbulent premixed flames, in: APS Meeting Abstracts, 2015.

[49] M. P. Burke, M. Chaos, Y. Ju, F. L. Dryer, S. J. Klippenstein, Comprehensive h2/o2 kinetic model for high-pressure combustion, International Journal of Chemical Kinetics 44 (7) (2012) 444–474.

[50] N. Peters, Turbulent Combustion, Cambridge University Press, UK, Cambridge, UK, 2000.

[51] M. Valorani, F. Creta, D. A. Goussis, J. C. Lee, H. N. Najm, Chemical Kinetics Simplification via CSP, Combustion and Flame 146 (2006) 29–51.

[52] M. Valorani, F. Creta, F. Donato, H. N. Najm, D. A. Goussis, Skeletal mechanism generation and analysis for¡ i¿ n¡/i¿-heptane with csp, Proceedings of the Combustion Institute 31 (1) (2007) 483–490.

[53] J. Prager, H. N. Najm, M. Valorani, D. A. Goussis, Skeletal mechanism generation with csp and validation for premixed¡ i¿ n¡/i¿-heptane flames, Proceedings of the Combustion Institute 32 (1) (2009) 509–517.

[54] M. Valorani, F. Creta, F. Donato, H. N. Najm, D. A. Goussis, A csp-based skeletal mechanism generation procedure: Auto-ignition and premixed laminar flames in *n*-heptane/air mixtures, in: ECCOMAS CFD 2006, Delft, Holland, 2006.

[55] M. Kooshkbaghi, C. E. Frouzakis, K. Boulouchos, I. V. Karlin, Entropy production analysis for mechanism reduction, Combustion and Flame 161 (6) (2014) 1507 – 1515.

[56] P. Selvaraj, P. G. Arias, B. J. Lee, H. G. Im, Y. Wang, Y. Gao, S. Park, S. M. Sarathy, T. Lu, S. H. Chung, A computational study of ethylene–air sooting flames: Effects of large polycyclic aromatic hydrocarbons, Combustion and Flame 163 (2015) 427–436.

[57] T. Lu, M. Plomer, Z. Luo, S. Sarathy, W. Pitz, S. Som, D. E. Longman, Directed Relation Graph with Expert Knowledge for Skeletal Mechanism Reduction, 7th US National Combustion Meeting.

[58] X.L.Zheng, T.F.Lu, C.K.Law, Experimental counterflow ignition temperatures and reaction mechanisms of 1,3-butadiene, Proceedings of the Combustion Institute 31 (2007) 367–375.

[59] C. Westbrook, F. Dryer, Chemical Kinetic Modeling of Hydrocarbon Combustion, Progress in Energy and Combustion Science 10 (1984) 1–57.

[60] P. Pal, M. Valorani, P. G. Arias, H. G. Im, M. S. Wooldridge, P. P. Ciottoli, R. Malpica Galassi, Computational characterization of ignition regimes in a syngas/air mixture with temperature fluctuations, Proceedings of the Combustion Institute 36 (3) (2017) 3705–3716.

[61] H. Curran, P. Gaffuri, W. Pitz, C. Westbrook, A Comprehensive Modeling Study of n-Heptane Oxidation 114 (1–2) (1998) 149–177.

[62] D. Bianchi, B. Betti, F. Nasuti, C. Carmicino, Simulation of gaseous oxygen/hydroxyl-terminated polybutadiene hybrid rocket flowfields and comparison with experiments, Journal of Propulsion and Power 31 (3) (2015) 919–929.

[63] A. Laskin, H. Wang, C. K. Law, Detailed kinetic modeling of 1, 3-butadiene oxidation at high temperatures, International Journal of Chemical Kinetics 32 (10) (2000) 589–614.

[64] D. Bianchi, F. Nasuti, C. Carmicino, Hybrid rockets with axial injector: Port diameter effect on fuel regression rate, Journal of Propulsion and Power (2016) 1–13.

[65] R. Barlow, G. Fiechtner, C. Carter, J.-Y. Chen, Experiments on the scalar structure of turbulent co/h 2/n 2 jet flames, Combustion and Flame 120 (4) (2000) 549–569.

[66] R. Barlow, J. Frank, A. Karpetis, J.-Y. Chen, Piloted methane/air jet flames: Transport effects and aspects of scalar structure, Combustion and Flame 143 (4) (2005) 433–449.

[67] M. M. Rogers, R. D. Moser, Direct simulation of a self-similar turbulent mixing layer, Physics of Fluids 6 (2) (1994) 903–923.

[68] A. Attili, F. Bisetti, Statistics and scaling of turbulence in a spatially developing mixing layer at reλ= 250, Physics of Fluids 24 (3) (2012) 035109.

[69] A. Attili, F. Bisetti, Fluctuations of a passive scalar in a turbulent mixing layer, Physical Review E 88 (3) (2013) 033013.

[70] R. B. Loucks, J. M. Wallace, Velocity and velocity gradient based properties of a turbulent plane mixing layer, Journal of Fluid Mechanics 699 (2012) 280–319.

[71] A. Attili, F. Bisetti, M. E. Mueller, H. Pitsch, Effects of non-unity lewis number of gas-phase species in turbulent nonpremixed sooting flames, Combustion and Flame 166 (2016) 192–202.

[72] H. Pitsch, Unsteady flamelet modeling of differential diffusion in turbulent jet diffusion flames, Combustion and Flame 123 (3) (2000) 358–374.

[73] Y. Xuan, G. Blanquart, A flamelet-based a priori analysis on the chemistry tabulation of polycyclic aromatic hydrocarbons in non-premixed flames, Combustion and Flame 161 (6) (2014) 1516 – 1525.

[74] A. E. Karataş, Ö. L. Gülder, Soot formation in high pressure laminar diffusion flames, Progr. in Ener. and Combust. Sci. 38 (6) (2012) 818–845.

[75] G. Leccese, D. Bianchi, F. Nasuti, Simulations of hybrid rocket flowfields including modeling of fuel pyrolysis and thermal radiation, SP2016-3125176, 5th Space Propulsion Conference, Rome, May 2016.

[76] M. Valorani, F. Creta, F. Donato, H. N. Najm, D. A. Goussis, Skeletal Mechanism Generation and Analysis for n-heptane with CSP, Proc. Comb. Inst. 31 (2007) 483–490.

[77] C. Homescu, L. R. Petzold, R. Serban, Error estimation for reduced-order models of dynamical systems, SIAM Review 49 (2) (2007) 277–299.

[78] B. Sonday, R. Berry, H. Najm, B. Debusschere, Eigenvalues of the Jacobian of a Galerkin-Projected Uncertain ODE System, SIAM J. Sci. Comp. 33 (2011) 1212–1233.

[79] M. Salloum, A. Alexanderian, O. Le Maître, H. Najm, O. Knio, Simplified CSP Analysis of a Stiff Stochastic ODE System, Computer Methods in Applied Mechanics and Engineering 217-220 (2012) 121–138.

[80] C. Sun, J. Hahn, Model reduction in the presence of uncertainty model parameters, J. Process Control 16 (2006) 645–649, short communication.

[81] C. Sun, J. Hahn, Parameter reduction for stable dynamical systems based on Hankel singular values and sensitivity analysis, Chemical Engineering Science 61 (2006) 5393–5403.

[82] A. Antoulas, Approximation of Large-Scale Dynamical Systems, SIAM Publications, Philadelphia, PA, 2005.

[83] P. Benner, V. Mehrmann, D. Sorensen, Dimension Reduction of Large-Scale Systems, in: Lecture Notes in Computational Science and Engineering, Vol. 45, Springer-Verlag, Berlin/Heidelberg, Germany, 2005.

[84] M. Clyde, Bayesian model averaging and model search strategies (with discussion), in: J. Bernardo, J. Berger, A. Dawid, A. Smith (Eds.), Bayesian Statistics 6, Oxford University Press, 1999, pp. 157–185.

[85] J. A. Hoeting, D. Madigan, A. E. Raftery, C. T. Volinsky, Bayesian model averaging: a tutorial, Statistical Science 14 (4) (1999) 382–417.

[86] É. Hébrard, A. S. Tomlin, R. Bounaceur, F. Battin-Leclerc, Determining predictive uncertainties and global sensitivities for large parameter systems: A case study for n-butane oxidation, Proceedings of the Combustion Institute 35 (1) (2015) 607–616.

[87] J. Warnatz, Resolution of gas phase and surface combustion chemistry into elementary reactions, in: Twenty-Fourth Symposium (International) on Combustion, Vol. 24, The Combustion Institute, 1992, pp. 553–579.

[88] B. Phenix, J. Dinaro, M. Tatang, J. Tester, J. Howard, G. McRae, Incorporation of Parametric Uncertainty into Complex Kinetic Mechanisms: Application to Hydrogen Oxidation in Supercritical Water, Comb. and Flame 112 (1998) 132–146.

[89] S. P. Sander, J. Abbatt, J. R. Barker, J. B. Burkholder, R. R. Friedl, D. M. Golden, R. E. Huie, C. E. Kolb, M. J. Kurylo, G. K. Moortgat, V. L. Orkin, P. H. Wine, Chemical kinetics and photochemical data for use in atmospheric studies, evaluation no. 17, Tech. Rep. JPL Publication 10-6, Jet Propulsion Laboratory, Pasadena, CA, http://jpldataeval.jpl.nasa.gov (2011).

[90] T. Turányi, T. Nagy, I. Zsély, M. Cserháti, T. Varga, B. Szabó, I. Sedyó, P. Kiss, A. Zempléni, H. Curran, Determination of rate parameters based on both direct and indirect measurements, Int. J. Chem. Kinetics 44 (2012) 284–302.

[91] D. Miller, M. Frenklach, Sensitivity Analysis and Parameter Estimation in Dynamic Modeling of Chemical Kinetics, Int. J. Chem. Kinetics 15 (1983) 677–696.

[92] K. Braman, T. A. Oliver, V. Raman, Bayesian analysis of syngas chemistry models, Combustion Theory and Modelling 17 (5) (2013) 858–887.

[93] M. Frenklach, H. Wang, M. J. Rabinowitz, Optimization and analysis of large chemical kinetic mechanisms using the solution mapping method – combustion of methane, Progress in Energy and Combustion Science 18 (1) (1992) 47–73.

[94] M. Frenklach, A. Packard, P. Seiler, R. Feeley, Collaborative Data Processing in Developing Predictive Models of Complex Reaction Systems, Int. J. Chem. Kinetics 36 (2004) 57–66.

[95] M. Frenklach, Transforming data into knowledge – Process Informatics for combustion chemistry, Proc. Comb. Inst. 31 (1) (2007) 125–140.

[96] D. A. Sheen, H. Wang, Combustion kinetic modeling using multispecies time histories in shock-tube oxidation of heptane, Combustion and Flame 158 (4) (2011) 645–656.

[97] J. Prager, H. Najm, K. Sargsyan, C. Safta, W. Pitz, Uncertainty Quantification of Reaction Mechanisms Accounting for Correlations Introduced by Rate Rules and Fitted Arrhenius Parameters, Combustion and Flame 160 (2013) 1583–1593.

[98] A. S. Tomlin, E. Agbro, V. Nevrlỳ, J. Dlabka, M. Vašinek, Evaluation of combustion mechanisms using global uncertainty and sensitivity analyses: A case study for low-temperature dimethyl ether oxidation, International Journal of Chemical Kinetics 46 (11) (2014) 662–682.

[99] H. Wang, D. A. Sheen, Combustion kinetic model uncertainty quantification, propagation and minimization, Progress in Energy and Combustion Science 47 (2015) 1–31.

[100] M. Khalil, K. Chowdhary, C. Safta, K. Sargsyan, H. Najm, Inference of reaction rate parameters based on summary statistics from experiments, Proc. Comb. Inst.In press. doi:10.1016/j.proci.2016.08.058.

[101] R. Bilger, Conditional moment closure for turbulent reacting flow, Phys. Fluids 5 (1993) 436–444.

[102] T. Poinsot, D. Veynante, Theoretical and numerical combustion, RT Edwards Inc., Philadelphia, PA, 2005.

List of publications

Some of the ideas and figures presented in the thesis may have previously appeared in the following publications:

Journal Papers

- P.P.Ciottoli, R.Malpica Galassi, P.E.Lapenna, G.Leccese, D.Bianchi, F.Nasuti, F.Creta, M.Valorani "CSP-based chemical kinetics mechanisms simplification strategy for non-premixed combustion: An application to hybrid rocket propulsion". Combustion and Flame 186 (2017) 83-–93

- R.Malpica Galassi, M.Valorani, H.N.Najm, C.Safta, M.Khalil, P.P.Ciottoli "Chemical Model Reduction under Uncertainty". Combustion and Flame 179 (2017) 242-–252

- M.Valorani, S.Paolucci, P.P.Ciottoli, R.Malpica Galassi, "Entropy Production and Timescales." Combustion Theory and Modelling, 21 (1) (2017) 137–157

- M.Valorani, P.P.Ciottoli, R.Malpica Galassi, "Tangential Stretching Rate (TSR) Analysis of Non Premixed Reactive Flows." Proceedings of the combustion institute, 36 (1) (2016) 1357–1367.

- P.Pal, M.Valorani, P.G.Arias, H.G.Im, M.S.Wooldridge, P.P.Ciottoli, R.Malpica Galassi, "Computational characterization of ignition regimes in a syngas/air mixture with

temperature fluctuations." Proceedings of the combustion institute, 36 (3) (2016) 3705-–3716.

Conference Papers

- E.Tingas, R.Malpica Galassi, P.P.Ciottoli, N.Mukhadiyev, H.Im, M.Valorani, "Dynamical system analysis of a turbulent premixed planar hydrogen flame in the corrugated flamelets combustion regime" 10th Mediterranean Combustion Symposium, 2017

- M.Valorani, P.P.Ciottoli, R.Malpica Galassi, S.Paolucci, T.Grenga, E.Martelli, "Enhancements of the G-Scheme framework" 10th Mediterranean Combustion Symposium, 2017

- R.Malpica Galassi, P.P.Ciottoli, M.Valorani, "A CSP-based automatic procedure to identify reactions leading to hyper-fast timescales in reacting systems" Meeting of the Italian Section of the Combustion Institute, 2017

- M.Valorani, P.P.Ciottoli, R.Malpica Galassi, S.Paolucci, T.Grenga, E.Martelli "Enhancements of the G-Scheme Framework" International Workshop on Model Reduction in Reacting Flows 2017

- R.Malpica Galassi, M.Valorani, H.N.Najm, C.Safta, M.Khalil, P.P.Ciottoli "A novel strategy for analysis and reduction of uncertain chemical kinetic models" International Workshop on Model Reduction in Reacting Flows 2017

- P.P.Ciottoli, R.Malpica Galassi, P.E.Lapenna, G.Leccese, D.Bianchi, F.Nasuti, F.Creta, M.Valorani "Skeletal chemical kinetic mechanism for HTPB-based hybrid rockets." 8th European Combustion Meeting, 2017.

- P.P.Ciottoli, B.J.Lee, P.E.Lapenna, R.Malpica Galassi, M.Valorani, H.G.Im, "Large eddy simulation on the effects of pressure on syngas/air turbulent nonpremixed flames." 8th European Combustion Meeting, 2017.

- R.Malpica Galassi, P.E.Lapenna, P.P.Ciottoli, G.Leccese, D.Bianchi, F.Nasuti, F.Creta, M.Valorani "Simplified chemical kinetic mechanisms for hybrid rocket propulsion." Meeting of the Italian Section of the Combustion Institute, 2016.